ANNUAL REPORT

Center for Experimental Nuclear Physics and Astrophysics
University of Washington
April, 2010

Sponsored in part by the United States Department of Energy
under Grant #DE-FG02-97ER41020.

Cover photos, counter-clockwise from the top: (1.) The cryogenic torsion balance (see Sec. 2.7) with Frank Fleischer on the left and Massimo Bassan on the right. Photo provided by Frank Fleischer. (2.) The KATRIN pinch and detector magnets and the KATRIN vacuum system (see Sec. 1.8). Kevin Wierman is standing to the left and Laura Bodine is on the right. Photo by Greg Harper. (3.) Ted Cook taking digital microscopic images of the wedge pendulum apparatus (see Sec. 2.3). Photo by Greg Harper. (4.) David Zumwalt attaching the viewport to the ^{6}He target apparatus (see Sec. 2.12). Photo by Greg Harper.

INTRODUCTION

The Center for Experimental Nuclear Physics and Astrophysics, CENPA, was established in 1998 at the University of Washington as the institutional home for a broad program of research in nuclear physics, astrophysics, and related fields. Research activities are conducted locally and at remote sites. CENPA has been a major participant in the Sudbury Neutrino Observatory (SNO) and is presently contributing substantially to the KATRIN tritium beta decay experiment, the MAJORANA ^{76}Ge double beta decay experiment, and the SNO+ ^{150}Nd double beta decay experiment in Canada. The current program includes "in-house" research on nuclear astrophysics and fundamental interactions using the local tandem Van de Graaff, as well as local and remote non-accelerator research on fundamental interactions and user-mode research on relativistic heavy ions at the Relativistic Heavy Ion Collider at Brookhaven.

Much of note has taken place in the 2009-10 period. Our second CENPA Fellow, Sanshiro Enomoto, joined us in October 2009, and is immersed in our SNO+ and KATRIN projects. Professor John Cramer retired in January 2010, and a symposium in honor of his 75th birthday was held in September, a celebration of a truly remarkable career. Two valued members of our professional staff departed. David Peterson has joined our staff replacing electronics technician Allan Myers, who has moved to PNNL in Richland, and Gary Holman steps into the big shoes of computer systems manager Dick Seymour, who retired in March 2010. On the retirement of David Boulware in July 2009, Blayne Heckel has taken over as Department Chair. Somehow in the middle of all that he and his group managed to achieve the world's most sensitive search for an atomic electric dipole moment, in ^{199}Hg.

On the departure of Professor John Wilkerson for the University of North Carolina in January 2009, the Department of Physics and College of Arts and Sciences committed to try to recruit a senior physicist of comparable caliber and leadership to replace him. It is with delight and excitement that we can report success. Professors David Hertzog and Peter Kammel from the University of Illinois at Urbana-Champaign will be joining our faculty before the fall quarter of 2010. Professor Nancy Hertzog, David's wife, will take over the Directorship of the UW's Robinson Center, which specializes in gifted and early education. The success of our search was made possible by the exceptional efforts of Search Committee Chair and INT Director David Kaplan, Robinson Center Director *pro tem* John Sahr, Divisional Dean Werner Stuetzle, Dean Ana Mari Cauce, Provost Phyllis Wise, and countless others. We take this opportunity to extend our gratitude to them.

The DOE Office of Nuclear Physics, which provides operating support through programs in Low Energy Nuclear Physics and Heavy Ion Physics, has renewed our support for FY10, which began December 1, 2009, and is the second of the current 3-year cycle. In the following paragraphs we record some of the highlights of our past year in research.

A new upper limit, seven times more sensitive than the previous limit, on the electric dipole moment of ^{199}Hg has been achieved. A comprehensive review article on this work has been written.

The static electric field in the ^{199}Hg electric dipole moment experiment admixes M1 and E2 transitions with the primary E1 transition used to probe the Hg atoms. The small frequency shift from this admixture, linear in the applied electric field, has been measured for the first time.

Commissioning of the KATRIN detector system continues with the commissioning of the various sub-systems. A major event was the delivery and commissioning of the long delayed detector and pinch magnets. These were successfully run at their full design field of 6T. The vacuum system, including calibration hardware, has been commissioned and integrated with the slow controls system. With the delivery by our colleagues at Karlsruhe Institute of Technology (KIT) of the complete analog readout electronics, commissioning of the electronics system and characterization of the detectors are almost complete. This work was carried out using the latest Mark-IV version of the DAQ hardware supplied by KIT and running under the ORCA software. Final commissioning of the entire detector system is about to begin with shipping to KIT sheduled for Fall 2010.

A near-time analysis tool for the KATRIN experiment has been developed. The tool will be used for comissioning works and also will be a part of the detector monitoring system when stable data taking begins. Although it was primarily designed for the Focal Plane Detector (FPD), it has a general framework, and integration to the KATRIN onsite tools for use in general KATRIN components is being done.

Results from a new low-energy-threshold analysis of data from both the first phase (pure D_2O and second phase (with dissolved salt) of the Sudbury Neutrino Observatory (SNO) were submitted for publication. Improved statistics and much reduced systematic uncertainties lead to improved precision in the determination of the mixing angle θ_{12}, as well as providing an upper limit on the value of θ_{13}.

A feasibility study of a future large scintillation detector was started. Using comprehensive Monte Carlo (MC) simulation tools originally developed for KamLAND and later considerably improved for SNO+, we have performed detailed studies of physics processes and optics. Based on the simulation results, we constructed prototype analysis tools and used them to evaluate the detector design.

For the Majorana Demonstrator Project, a prototype data-acquisition system was successfully fielded at Soudan with a point-contact geometry Ge detector. This apparatus has been used to set limits on light WIMP dark matter particles. The results published in Phys. Rev. Lett. were covered in Nature News:
http://www.nature.com/news/2010/100226/full/news.2010.97.html.

A novel, custom built parylene and copper ribbon cable was designed and prototyped with promising results. It is low in radioactivity and may solve the cable problem for Majorana. A new design of low-noise pre-amplifier has been prototyped, also with promising results.

The decommissioned radiocarbon laboratory of Prof. Minze Stuiver contains some 50 tonnes of high-quality lead bricks, samples of which have now been radioassayed and show extremely low levels of ^{210}Pb. These bricks will be retrieved and put to new use in the Majorana shield.

The preparation of thin, ion-implanted targets of ^{20}Ne, ^{24}Mg, ^{28}Si, ^{32}S, and ^{36}Ar at CENPA was completed. These targets were used in a CENPA-led experiment at the Technical University of Munich to measure the masses of ^{20}Na, ^{24}Al, ^{28}P, and ^{32}Cl, and excitation energies in ^{32}Cl and ^{36}K, to high precision. The results will contribute to tests of the electroweak standard model and studies of explosive hydrogen burning on accreting compact stars in binary systems.

Data were acquired at the IGISOL facility of the University of Jyväskylä to measure the electron-capture branch in the decay of ^{116}In. The detectors and associated electronics were initially assembled and tested at CENPA and then shipped to Finland for the experiment. The result will provide a constraint for calculations of the matrix element for the potential neutrinoless double beta decay of ^{116}Cd.

The data taking on the measurements of (p, γ) resonances on ^{22}Na in the 190 to 650 keV proton energy range is now complete. The absolute strengths for resonances at proton energies of 214, 284, 456, and 607 keV have been determined and were found to be substantially larger than those previously reported. Upper limits for strengths of the proposed resonances at 198, 209, and 232 keV have also been determined and the resonance at 214 keV was found to be the dominant contributor to the destruction of ^{22}Na in novae.

Using a recently designed molten lithium target chamber and a beam line at CENPA modified to accommodate it, experiments have shown that the production of ^{6}He is strong enough to justify setting up a laser trapping system. CENPA will do this in collaboration with the group at Argonne National Laboratory to determine the electron-antineutrino correlation in a search for tensor contributions to the weak interaction.

Two CENPA graduate students, Noah Oblath and Michelle Leber, obtained their Ph.D. degrees during the period of this report. Noah is a postdoc at MIT, Michelle a postdoc at UC Santa Barbara.

As always, we encourage outside applications for the use of our facilities. As a convenient reference for potential users, the table on the following page lists the capabilities of our accelerator. For further information, please contact Greg Harper, Associate Director, CENPA, Box 354290, University of Washington, Seattle, WA 98195; (206) 543-4080, or gharper@u.washington.edu. Further information is also available on our web page: http://www.npl.washington.edu.

We close this introduction with a reminder that the articles in this report describe work in progress and are not to be regarded as publications or to be quoted without permission of the authors. In each article the names of the investigators are listed alphabetically, with the primary author underlined, to whom inquiries should be addressed.

Hamish Robertson, Director

Greg Harper, Associate Director and Editor

Victoria Clarkson, Assistant Editor

TANDEM VAN DE GRAAFF ACCELERATOR

A High Voltage Engineering Corporation Model FN purchased in 1966 with NSF funds, operation funded primarily by the U.S. Department of Energy. See W. G. Weitkamp and F. H. Schmidt, "The University of Washington Three Stage Van de Graaff Accelerator," *Nucl. Instrum. Methods* **122**, 65 (1974). Recently adapted to an (optional) terminal ion source and a non-inclined tube #3, which enables the accelerator to produce high intensity beams of helium and hydrogen isotopes at energies from 100 keV to 7.5 MeV.

Some Available Energy Analyzed Beams

Ion	Max. Current (particle μA)	Max. Energy (MeV)	Ion Source
^{1}H or ^{2}H	50	18	DEIS or 860
^{3}He or ^{4}He	2	27	Double Charge-Exchange Source
^{3}He or ^{4}He	30	7.5	Tandem Terminal Source
^{6}Li or ^{7}Li	1	36	860
^{11}B	5	54	860
^{12}C or ^{13}C	10	63	860
*^{14}N	1	63	DEIS or 860
^{16}O or ^{18}O	10	72	DEIS or 860
F	10	72	DEIS or 860
* Ca	0.5	99	860
Ni	0.2	99	860
I	0.001	108	860

*Negative ion is the hydride, dihydride, or trihydride.

Several additional ion species are available including the following: Mg, Al, Si, P, S, Cl, Fe, Cu, Ge, Se, Br and Ag. Less common isotopes are generated from enriched material. We recently have been producing the positive ion beams of the noble gases He, Ne, Ar, and Kr at ion source energies from 10 keV to 100 keV for implantation, especially the rare isotopes ^{36}Ar and ^{21}Ne. We have also produced a separated beam of 15-MeV ^{8}B at 6 particles/second.

Contents

INTRODUCTION **i**

1 Neutrino Research **1**

SNO **1**

1.1 Overview of the SNO experiment and CENPA's contribution 1

SNO+ **2**

1.2 Overview of the SNO+ experiment and CENPA's contribution 2

1.3 Status of the SNO+ data acquisition software 3

1.4 Status of the SNO+ slow control system 4

1.5 SNO+ Monte Carlo verification studies 5

KATRIN **7**

1.6 Overview of KATRIN 7

1.6.1 Status of KATRIN hardware 7

1.6.2 Status of the CENPA contribution to KATRIN 9

1.7 Commissioning of the KATRIN focal-plane detector and electronics 12

1.8 Status of the superconducting magnets for KATRIN 14

1.9 Status of absolute calibration of KATRIN focal plane detector 15

Majorana **16**

1.10 Majorana Demonstrator activities 16

1.11 Surface-alpha measurements on HPGe detectors 17

1.12 A prototype DAQ system for the Majorana Demonstrator 18

1.13 Searches for direct detection of dark matter with a Majorana prototype . . 19

1.14 Data management and workflow management for the Majorana Demonstrator 20

1.15 Preparation and shipping of Pb bricks for the MAJORANA shield 21

1.16 Simulated response of a MAJORANA detector string to ^{68}Ge 22

1.17 Thermal and vacuum measurements from a prototype MAJORANA cryostat and string 23

1.18 Design and fabrication of ultra-low background parylene-copper ribbon cable for MAJORANA 24

Project 8 **26**

1.19 Status of the Project 8 neutrino mass measurement prototype 26

Large Detector **28**

1.20 Investigations into the feasibility of a very large liquid scintillator detector for next generation long baseline neutrino experiments 28

1.21 Reconstructing the light production distribution in a liquid scintillator detector 30

HALO **32**

1.22 The HALO supernova detector 32

2 Fundamental Symmetries and Weak Interactions **34**

Torsion Balance Experiments **34**

2.1 Current status on improved equivalence principle limits for gravitational self-energy 34

2.2 Parallel plate test of Newton's gravitational inverse square law 35

2.3 Wedge pendulum progress report: data and analysis 36

2.4 Progress on a torsion balance test of new spin coupled forces 37

2.5 Designing an equivalence-principle pendulum containing a hydrogen-rich test body 38

2.6 Looking for signatures of space-time granularity with a spin-polarized torsion pendulum 39

2.7 A cryogenic torsion balance for tests of the equivalence principle 40

2.8 Observation of Lévy walks in torsion balance squeeze film damping 41

2.9 Development of a high-precision interferometric quasi-autocollimator 42

2.10 UV charge management for gravitational wave observatories 43

Weak Interactions **45**

2.11 Laser trap developments for ^{6}He 45

2.12 Production of ^{6}He at CENPA 47

2.13 Permanent electric dipole moment of atomic mercury 48

2.14 Progress in determining the beta asymmetry from neutron decay 49

2.15 Progress in analysis of emiT data 49

2.16 Parity non-conserving neutron spin rotation experiment 50

2.17 M1 width of the 2_1^+ state in ^{22}Na and searches for tensor contributions to beta decays. 52

3 Axion Searches **53**

3.1 ADMX axion search 53

3.2 Acceleration predictions for moving the ADMX cryostat through a mock move experiment 58

3.3 Continued studies of systematic errors in the “axion” torsion-balance experiment 59

4 Nuclear Astrophysics **60**

4.1 Measurements of ^{33}S$(p, \gamma)^{34}$Cl at nova temperatures 60

4.2 Determining the reaction rate for ^{22}Na(p, γ): final results 62

4.3 Correlations between solar activity and nuclear decay rates? 63

5 Nuclear Structure **65**

5.1 Electron capture on ^{116}In and 2β decay 65

5.2 Precise measurements of ^{20}Na, ^{24}Al, ^{28}P, ^{32}Cl, and ^{36}K 66

5.3 Mass of ^{31}S with the Canadian Penning Trap 68

6 Relativistic Heavy Ions **70**

6.1 Summary of event structure research 70

6.2 Tracking issues affecting two particle angular correlations in STAR 71

6.3 Fitting charge-independent joint angular autocorrelations 72

6.4 Progress on understanding the Cu-Cu data 73

6.5 Two-particle correlations with marginal y_t cuts for 62 and 200 GeV Au-Au collisions 74

6.6 Quadrupole component marginal p_t dependence 75

6.7 Quadrupole spectrum and universality 76

6.8 Gaussian jet peak marginal p_t dependence 77

6.9 Parametrization of quadrupole centrality and p_t/y_t dependence 78

6.10 Mean jet correlations in a finite angular acceptance 79

6.11 Jet properties inferred from jet angular correlations 80

6.12 Minijet contribution to Au-Au particle production 81

6.13 Extracting single-particle fragment spectra from jet correlations 82

6.13.1 pQCD jet fragment distributions 82

6.13.2 Factorization of pair distribution 82

6.13.3 Connecting jet correlations to spectrum hard components and pQCD 83

6.14 Marginal distributions of jet angular correlations on y_t 84

6.15 Marginal jet correlations versus spectrum hard components and pQCD 85

6.16 Status of the DWEF model for the analysis of pion interferometry 86

7 Computing, and Electronics **87**

7.1 Laboratory computer systems 87

7.2 Athena: a high end computing deployment for scientific computing 88

7.3 Preamplifier with forward biased reset for MAJORANA 89

7.4 Electronic equipment 91

8 Accelerator and ion sources **92**

8.1 Van de Graaff accelerator and ion source operations and development 92

9 Other Research **93**

9.1 Progress on a test of quantum nonlocal communication 93

9.2 A "half-slit" interferometer based on the Mach-Zehnder design 95

9.3 Stochastics of dosimetry of C-ions 98

10 CENPA Personnel **100**

10.1 Faculty 100

10.2 CENPA External Advisory Committee 100

10.3 Postdoctoral Research Associates 101

10.4 Predoctoral Research Associates 101

10.5 NSF Research Experience for Undergraduates participants 101

10.6 University of Washington undergraduates taking research credit 102

10.7 Professional staff 102

10.8 Technical staff 103

10.9 Administrative staff 103

10.10 Part time staff and student helpers 103

11 Publications **104**

11.1 Published papers 104

11.2 Papers submitted or to be published 2010 108

11.3 Invited talks, abstracts and other conference presentations 110

11.4 Ph.D. degrees granted 113

1 Neutrino Research

SNO

1.1 Overview of the SNO experiment and CENPA's contribution

N. S. Oblath*, R. G. H. Robertson, N. R. Tolich, B. A. VanDevender,
H. S. Wan Chan Tseung, plus the SNO Collaboration.

The primary scientific goal of the Sudbury Neutrino Observatory (SNO) experiment was to measure the flux of the different neutrino flavors coming from the Sun in order to understand the solar neutrino anomaly. There were three distinct phases of the experiment, each of which measured the total fluxes for all three light neutrino flavors in a different way. For the first and second phases, respectively, neutrons produced by neutrino neutral current interactions in the D_2O were observed by the the gammas emitted from the subsequent neutron capture on ^2H and ^{35}Cl. For the third phase, proportional counters filled with ^3He were deployed within the D_2O, to detect the neutrons. Since data taking ended in November, 2006, all efforts have focussed on analysis of the recorded data.

In the past year the SNO collaboration published a reanalysis of the data collected in the first two phases of SNO[1] and a search for high frequency oscillation in the solar neutrino data[2]. The reanalysis of the first two phases improved precision by a factor of almost two over the previous SNO results. Work has also been done to combine the improved result from the first two phases with an improved analysis of data collected in the third phase. This will be the most accurate result possible with the SNO data and likely the most accurate solar neutrino measurement for the foreseeable future. The main effort to reduce both the statistical and systematic errors in the third phase involves the development of pulse shape analysis to distinguish the signals from neutrons and alphas in the proportional counters. Oblath has developed a technique comparing actual pulse shapes with pulse shapes obtained from simulations of both neutrons and alphas in the proportional counters. Tolich has developed a pulse shape analysis that relies on variations in the width and skewness for neutron and alpha pulses. These two independent techniques combined with a third technique can eliminate more than 98 % of alpha backgrounds while preserving approximately 75 % of neutrons. Oblath's technique builds on previous efforts[3] to develop the simulations by Oblath, Wan Chan Tseung, and Robertson, for which they are working on a publication.

In the past year Robertson and VanDevender together with a small group of other collaborators have nearly completed a publication of their work[4] to identify two "hotspots" of backgrounds on the proportional counters. It is expected that all work on SNO will be finished by summer of 2010, completing what has been a main area of research at CENPA for more than a decade and that has led to some very exciting results confirming that the solar neutrino anomaly was caused by neutrino oscillations.

---

*Presently at M.I.T.

[1] B. Aharmim, *et al.* Phys. Rev. C *in press* (2010)

[2] B. Aharmim, *et al.* ApJ **710** 540 (2010)

[3] CENPA Annual Report, University of Washington (2008) p. 5.

[4] CENPA Annual Report, University of Washington (2008) p. 7.

SNO+

1.2 Overview of the SNO+ experiment and CENPA's contribution

S. Enomoto, J. Kaspar, J. K. Nance, D. Scislowski, N. R. Tolich, and
H. S. Wan Chan Tseung

The primary scientific goal of the SNO+ experiment is to observe lepton number violation by observing neutrinoless-double-beta-decay in ^{150}Nd. There are, however, a number of other scientific goals such as using neutrinos to measure the heat production in the earth and the sun, and to measure neutrino oscillation parameters using neutrinos from nearby nuclear reactors and the sun.

The SNO+ project builds on the infrastructure of the Sudbury Neutrino Observatory (SNO) project, which ended data taking in November, 2006. The main change to the SNO detector is to replace the heavy water contained within the inner acrylic vessel with liquid scintillator loaded with ^{150}Nd. In the last year the funding for the major aspects of this work has been approved by Canadian funding agencies. The main engineering task is to fasten the acrylic vessel to the floor since the liquid scintillator is less dense than the surrounding water resulting in a large buoyant force. This work is proceeding well, although there was a delay in the start of this work. It is now expected that we will start collecting data in early 2012.

The liquid scintillator will result in significantly more light than observed in SNO, therefore there is also a need to update the electronics and data acquisition software (DAQ) to handle the higher data rate. The University of Pennsylvania will update the electronics that read out each crate of front-end electronics. CENPA has accepted responsibility for updating the DAQ to a faster computer platform and more modern software to handle the two orders of magnitude increase in the data rate. This work is described in section 1.3. CENPA has also accepted responsibility for updating the slow control system used in SNO, which is responsible for reading out detector related variables at a frequency of approximately 1 Hz. With many of the variables readout for SNO moving to a centralized location for the newly created SNOLAB, it was decided that SNO+ should invest in a new system with easier access to the data. This work is described in section 1.4.

CENPA has also been active in verification of the SNO+ Monte Carlo (MC). The MC will be necessary for understanding systematic errors after data is collected. However, before data collection the MC is being used to develop reconstruction tools and to guide design decisions. Before any of this, it is necessary to verify that the MC reproduces expected results. CENPA has been doing much of this vital work, which is described in section 1.5.

1.3 Status of the SNO+ data acquisition software

M. A. Howe*, J. Kaspar, N. R. Tolich, and J. F. Wilkerson*

The scintillator filling the SNO+ detector will provide 25 times more photoelectrons per electron than the Cherenkov process in SNO, which will improve the energy resolution and allow the energy threshold to be decreased. The new DAQ software to handle the increased data rate is based on ORCA, a general purpose, highly modular, object-oriented, acquisition and control system that is easy to use, develop, and maintain. The DAQ pulls data from the VME trigger crate. There will be 19 data crates operating in an independent, asynchronous way pushing data into the DAQ system.

A test stand located in Sudbury has been used for our DAQ development. It allows us to run both the former SNO DAQ and the present ORCA system in parallel to cross-check the outputs. The agreement between the systems was excellent and allowed us to commission the trigger system. In 2009 we successfully tested the communication between the DAQ and the underground electronics.

New controllers for the data crates will arrive in Summer, 2010. DAQ is ready to commission them. The development is focusing on the user interface (see Fig. 1.3-1) and various calibration tasks. We currently are working on an event builder interface that will preserve backwards compatibility. The final parts to be implemented include a safe HV controller and an interface to the slow control system that will provide feedback information into the DAQ. We are also participating in efforts to incorporate the DAQ simulation in the MC package.

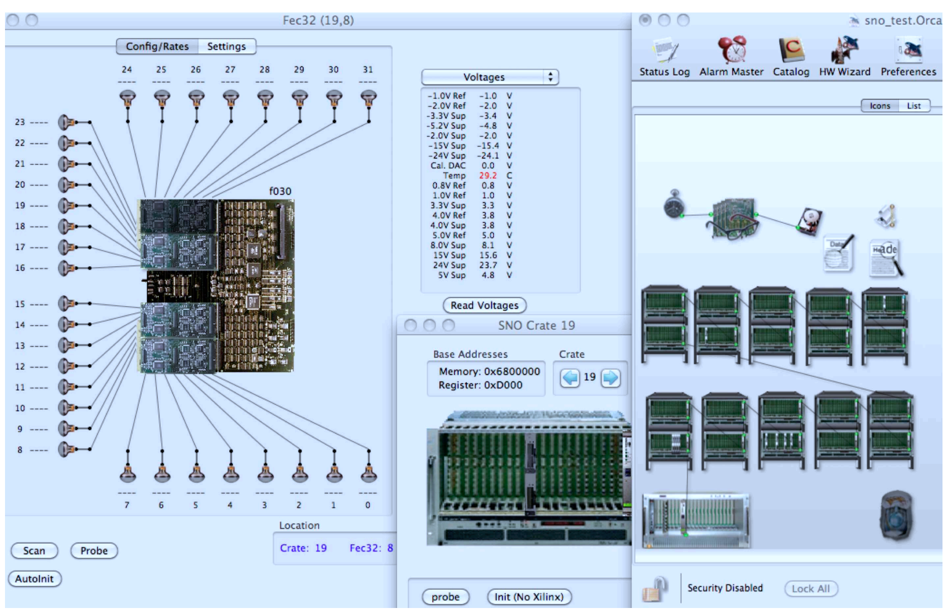

Figure 1.3-1. A graphical user interface to control a front-end card and a data crate is shown with a layout of the SNO+ experiment.

*University of North Carolina, Chapel Hill, NC

1.4 Status of the SNO+ slow control system

J. K. Nance

The SNO+ experiment will rely on the accurate collection of data from the approximately 10000 photomultiplier tubes which comprise the main detector package. In order for the experimenters to be reasonably confident in the validity of the data stream, a large amount of metadata regarding the state of the detector must also be collected and processed in parallel with the "physics" data. This metadata contains information such as the backplane voltages on the VME crates used to acquire the data, the magnitude of the electric current in the magnetic compensation coils which cancel the background magnetic field, and a number of other parameters without which the physics data itself would be difficult or impossible to interpret. In order to efficiently collect and store these data a "slow control" system is being designed at CENPA which incorporates all levels of data collection and data storage.

While many systems were considered, ultimately the decision was made to attempt to collect the slow control data as close to the source as possible in contrast to the original system in SNO which transported the data over long (30 m) cables to the collection system. This "distributed" approach has the potential to substantially reduce the noise in the measurements as well as making maintenance more manageable by isolating the hardware.

The back end of the slow control system will consist of a centralized database server running a PostgreSQL database cluster. If data were collected at 1 Hz intervals from each point of interest approximately 10^{10} data points would accrue during the operational lifetime of the SNO+ detector. This represents an intimidating volume of data for even very fast database clusters, so data will instead be collected and processed only when per channel pre-specified bounds are exceeded. The stored data will therefore consist of one very large dataset with all of the data points taken and a much smaller, faster database which contains the data represented in terms of intervals over which the data were within tolerances.

The front end data collection hardware itself will likely consist of modular, stand-alone analog-to-digital (ADC) cards which will then relay their data over ethernet to the database server. The design objective is to segment the data collection hardware in order to ensure that the failure of one particular module does not result in a systemic loss of operation of the slow control system. Numerous industrial standards exist for such modularized hardware and these standards will also act to minimize the overhead of repair or replacement.

Ultimately we believe that this design will lead to a system that will quickly and accurately report the state of the SNO+ detector both in real time and historically. Access to these data will ensure that the physics data collected by the detector is maximally useful to the SNO+ collaboration.

1.5 SNO+ Monte Carlo verification studies

D. Scislowski and H. S. Wan Chan Tseung

We report on work done to validate **R**eactor **A**nalysis **T**ool, the SNO+ Monte Carlo simulation package. RAT is a Geant4-based simulation that uses GLG4[1] to handle the scintillation process. Our efforts were focused on the two areas described below.

(1) Rayleigh scattering

We performed preliminary simulations to verify basic boundary reflection and refraction behaviors, and tested optical scattering against analytic formulae. It was found that the scattering momentum and polarization distributions in the Geant4.9.2 release did not agree with Rayleigh scattering theory. The GLG4 routine performed better but, having been written for machines of limited processing power (see Fig. 1.5-1), contains idiosyncracies. An alternative, modernized routine was written to replace these and will be used in future releases of RAT.

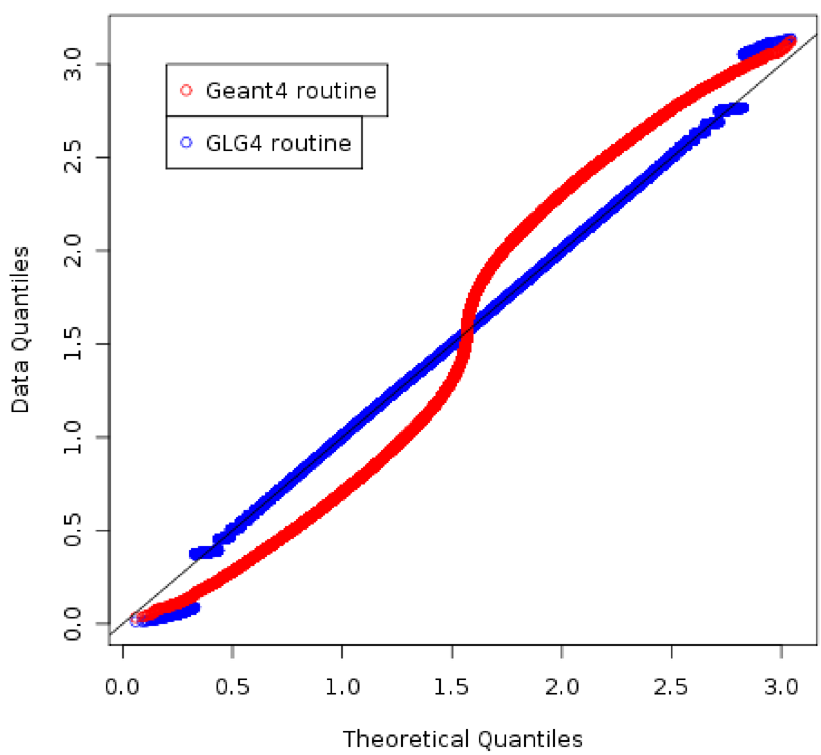

Figure 1.5-1. Quantile-quantile plots of scattering angles (measured between initial polarization and final momentum) generated from Rayleigh scattering routines against samples from the theoretical $\sin^3\psi$ distribution.

[1]**G**eneric **L**and **G**eant**4**– public domain release of KamLAND Monte Carlo code

(2) Neutron interactions and propagation

We compared Geant4.9.2 neutron interaction cross-section tables for all relevant nuclei (^{1}H, ^{2}H, ^{12}C, ^{13}C, ^{14}N, ^{15}N, ^{16}O, ^{17}O, and ^{18}O) in the SNO+ scintillator (LAB-PPO) with ENDF/B-VII.0, from thermal energies up to 20 MeV. Significant discrepancies in ^{16}O cross-sections were found. By means of simple, thin-target simulations performed with RAT we compared yields of the dominant neutron interactions with analytic calculations. We find that, in the RAT simulations, spurious low-energy γ-rays are emitted in neutron inelastic scattering. It appears that Geant4.9.2 introduces these non-physical γs to enforce energy conservation. We also find that the neutron-capture γ cascades of Nd isotopes are not implemented correctly. Finally, we compared computed neutron capture lengths and times from RAT, in both LAB-PPO and water, with SNOMAN[2] calculations. The agreement between RAT and SNOMAN in the LAB-PPO case is excellent. For water, RAT and SNOMAN give comparable results if the `G4NeutronHPThermalScattering` process, which takes into account molecular binding effects, is enabled in RAT.

[2] **SNO** **M**onte Carlo and **AN**alysis, the SNO Monte Carlo package, uses MCNP4 to propagate neutrons.

KATRIN

1.6 Overview of KATRIN

J. F. Amsbaugh, L. I. Bodine, T. H. Burritt, P. J. Doe, S. Enomoto, G. C. Harper, M. L. Leber*, E. L. Martin, A. W. Myers†, R. G. H. Robertson, K. Tolich‡, B. A. VanDevender, T. D. Van Wechel, and B. L. Wall

The KATRIN Neutrino Experiment is the latest, and perhaps the last of its type, in a long line of experiments that have used tritium beta decay to make a direct investigation of neutrino mass. A direct measurement is model independent, relying on kinematics to extract a value of the neutrino mass. KATRIN aims to reach a sensitivity of 0.2 eV, an order of magnitude improvement over the current direct measurement sensitivity of 2.3 eV. It does this by drawing on perhaps the best elements of preceeding experiments, principally, a windowless, gaseous tritium source and electrostatic retarding spectrometers. The experiment is located on the North Campus of the Karlsruhe Institute of Technology (KIT), formerly the Forschungszentrum, Karlsruhe, Germany. The choice of location was strongly influenced by KIT's license and experience in handling the large quantities of tritium required to reach the KATRIN sensitivity. The KATRIN collaboration was formed in 2001 and consists of over 100 scientists from four European countries and the USA. The participating US institutes consist of the University of Washington (UW, lead US institute and a founding member of KATRIN), the Massachusetts Institute of Technology (MIT), the University of North Carolina (UNC) and the University of California, Santa Barbara (UCSB).

KATRIN is currently in an intense construction phase. Data taking with tritium is tentatively expected to begin in late 2012 and to run through 2017, when the experimental sensitivity is expected to reach the systematic limit. To go significantly beyond 200 meV sensitivity would require impractical scaling of the KATRIN size. The UW is also participating in a project (see Sec. 1.19) that is investigating a novel technology that could potentially push beyond the KATRIN limit. Further information regarding the KATRIN experiment can be found at the KATRIN homepage[1].

1.6.1 Status of KATRIN hardware

The primary US responsibility in KATRIN is to supply the electron detector, the data acquisition system, and the so-called rear system used to monitor the tritium source. These and other KATRIN components are described below. The layout of the hardware of the KATRIN experiment is shown in Fig. 1.6-1

The heart of KATRIN consists of the windowless, gaseous tritium source (WGTS), a 10-meter long, 9-cm diameter tube, open at both ends and held at 27 K ±30 mK. Tritium

*Now at U.C. Santa Barbara

†Pacific Northwest National Laboratory, Richland, WA

‡Now at North Seattle Community College

[1] http://www-ik.fzk.de/ katrin/

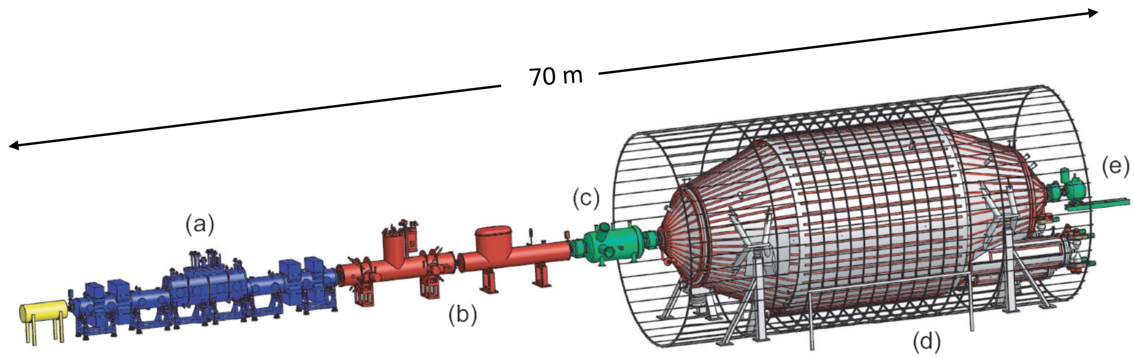

Figure 1.6-1. Schematic illustration of the KATRIN experiment showing the main components: (a) Windowless Gaseous Tritium Source (WGTS), (b) Transport system, consisting of the Differential Pumping System (DPS) and the Cryogenic Pumping System (CPS), (c) Pre-Spectrometer (PS), (d) Main Spectrometer (MS) surrounded by the Earth's magnetic field compensation coils, and (e) Detector

gas is injected into the WGTS to provide a column density of 5×10^{17} cm^{-2}. This results in approximately 10^{11} tritium decays per second. Decay electrons are constrained to be emitted from each end of the WGTS by a train of 3.6-T superconducting magnets. Those electrons emitted upstream (left in the figure) enter the Rear System, used to monitor the source. Those emitted downstream (right) enter the main analyzing portion of KATRIN. To control backgrounds in the spectrometers it is essential that tritium gas entering the spectrometers results in no more than 10^{-3} tritium decays per second, a reduction factor of 10^{14} in the decay rate. Tritium gas molecules escaping from each end of the WGTS are returned to the source by way of the Differential Pumping System (DPS), a series of turbo molecular pumps located at each end of the WGTS. The tritium pressure downstream of the DPS is reduced by 7 orders of magnitude. The DPS is followed by the Cryogenic Pumping System (CPS), another chicane of superconducting magnets where the wall of the beam pipe is coated with argon frost to cryosorb tritium molecules striking the wall. At the outlet of the CPS the tritium pressure, and therefore decay rate, has been reduced by a further 7 orders of magnitude. Decay electrons then enter the Pre-Spectrometer (PS) where the retarding potential is set to approximately 100 V below the tritium end point energy of 18.6 keV, allowing only the electrons of interest, at the high energy end of the spectrum, to pass into the Main Spectrometer (MS). The MS achieves an energy resolution of 0.93 eV by precisely controlling the retarding potential. Only those electrons with energy greater than the retarding potential pass though the MS to be recorded by the detector located at the exit of the MS. The detector's primary role is simply to count electrons, yielding an integral measure of the electron flux. It consists of a 10-cm diameter, monolithic array of PIN diodes. The spatial, temporal and energy information provided by the detector plays a vital role in understanding and controlling the sources of systematic error.

Acquisition and commissioning of the KATRIN hardware is occurring across a broad front. The WGTS has been challenging, in part because of a takeover and restructuring of the original manufacturing company. In April this year the source tube was delivered to KIT to demonstrate gas handling and temperature stability of the source. These tests will be completed by the end of the year. Details of the final assembly of the WGTS cryostat are under negotiation and are a critical path activity.

The DPS has been delivered to KIT and commissioning is expected to be complete by early 2011. The CPS magnets have passed tests and by years end it is expected to have completed cooling tests prior to delivery to KIT. Final acceptance tests will take place at KIT in March 2011. The pre-spectrometer continues to provide vital information regarding background sources such as Penning traps. In order to provide space for assembly of the WGTS, the pre-spectrometer will be relocated to its final position in front of the main spectrometer in October 2010. By March 2011 it will be ready for joint commissioning with the main spectrometer.

The Earth's magnetic field compensation coils that surround the main spectrometer have been installed and are being commissioned. Currently, the internal wire planes that shape the electric field and reduce backgrounds are being installed inside the main spectrometer vessel. The mechanical precision, high cleanliness, and working environment make this a very difficult task which is not expected to be complete until the end of 2010. Additional complications have arisen due to ^{219}Rn associated with radioactivity in the getter strips used for pumping the spectrometers. The resultant high energy Auger and conversion electrons have long cyclotron lifetimes in the UHV of the spectrometers resulting in rings of secondary electrons. To trap the Rn atoms liquid nitrogen cooled baffles will be installed in the pumping ports by the end of the year at considerable expense to the pumping efficiency. The spatial information from the detector is essential for understanding this background. The status of the detector is given below.

1.6.2 Status of the CENPA contribution to KATRIN

The detector system is currently being assembled and commissioned at UW with sub-components provided by MIT (the cosmic ray veto and radiation shield), UNC (DAQ software) and KIT (DAQ hardware and slow controls). A schematic of the entire detector hardware is shown in Fig. 1.6-2

A milestone was achieved with the delivery of the pinch and detector magnets in December 2009. These have passed their acceptance criteria and have been operated at their full field of 6 T, experiencing an attractive force of approximately 6 tonnes. The 500 kg lead and copper shield has been successfully installed into the bore of the detector magnet using the insertion device provided by MIT.

The electron and gamma calibration sources have been installed in the vacuum system. The original actuation devices which used flexible shaft drives have been replaced by air driven motors. The calibration system is under complete control of the slow controls system. In September 2009, the vacuum system was baked out and pumped on using the cryopumps.

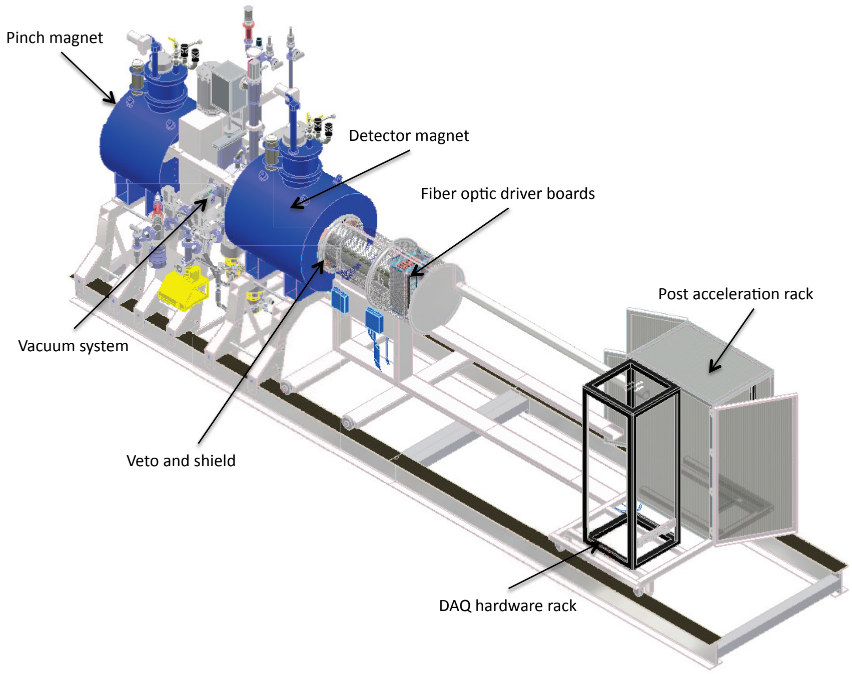

Figure 1.6-2. Schematic view of the detector system

A final pressure of 1.5×10^{-9} mbar was achieved at room temperature, satisfying the commissioning criteria. Final completion of the vacuum awaits the arrival of the new post acceleration electrode and the low background feed-through.

Preliminary results for a device built to provide an absolute calibration of the detector efficiency, PULCINELLA (see Sec. 1.9), indicate that it will reach the required sensitivity.

The DAQ hardware, consisting of the full complement of analog electronics and the Mark-IV DAQ crate, was received from KIT in October 2009. After debugging by UNC and UW, data was taken from all 148 pixels of the detector using the UW electron gun and gamma sources. This enabled the performance of the detector and analog electronics to be determined as a function of temperature and detector bias. Once these parameters have been optimized, the mono-energetic electron beam enables the dead layer thickness of the detector to be measured.

KIT is also responsible for providing the slow control system. In July 2009 the slow controls were integrated with the detector systems including the DAQ software. Completion of the slow controls awaits an interface unit for the magnet heaters.

Acquisition of some components have proved more challenging than anticipated. In order to reduce radioactive backgrounds, the detector is mounted on a custom 182 pin feed-through with low activity sapphire insulators. The technology of the company commissioned to provide this feed-through was not up to the job and more R&D is underway. Meanwhile, in order to proceed with commissioning, two custom feed-throughs using conventional technology have been purchased. These feed-throughs will suffice until actual tritium data taking begins in 2012. In order to minimize radioactive materials, connections between the feed-through and the detector wafer are made using pogo-pins. This unusual approach appears to be working well.

The first of two post acceleration electrodes was delivered to UW in June. Evacuating the electrode resulted in the stainless steel heat shield deforming by 1 cm. Examination of the heat shield revealed an area where the thickness of the spun metal was significantly less than specified. Although this electrode is still usable for commissioning the apparatus, new electrodes are being made and are expected to be ready by the time the apparatus is shipped to KIT.

MIT has supplied the cylindrical cosmic ray veto that surrounds the inert detector shield. It consists of formed plastic scintillator panels read out by wavelength shifting fibers and SiPMT's. Although this is a relatively conventional technique, the light collection efficiency is unexpectedly poor, resulting in unacceptable signal to noise levels. This has been traced to poor aperture matching of fibers and SiPMT's and a resolution is underway.

The schedule calls for commissioning at UW to be complete in mid July and shipping to KIT to take place in late August. Installation is expected to take until the end of the year and the first demand for the detector system is anticipated to occur in March 2011.

1.7 Commissioning of the KATRIN focal-plane detector and electronics

<u>B. A. VanDevender</u> and B. L. Wall

Initial tests of the KATRIN Focal Plane Detector (FPD)[1] and electronics[2] were conducted in 2009. The entire system, from detector to data-acquisition computer, has been assembled in a test chamber separate from the true KATRIN detector vacuum chamber. Radioactive sources used for commissioning are a 0.5 mCi ^{241}Am source and an electron gun capable of producing electrons with energies up to 30 keV focused onto a steerable beam spot with 0.1 mm diameter. The emphasis of the work so far has been to study the performance of the system and to diagnose and fix problems.

Fig. 1.7-1 (left) shows the best results to date for resolution of the FPD. The FWHM resolution is 1.8 keV for most channels. Virtually all missing channels (white) and poor performing channels (green–red) in Fig. 1.7-1 have been diagnosed and fixed resulting in more than 90% channels performing within the commissioning criteria (FWHM resolution<3.0 keV). The current performance is however short of our ultimate goal of FWHM resolution<1.2 keV with 100% working channels.

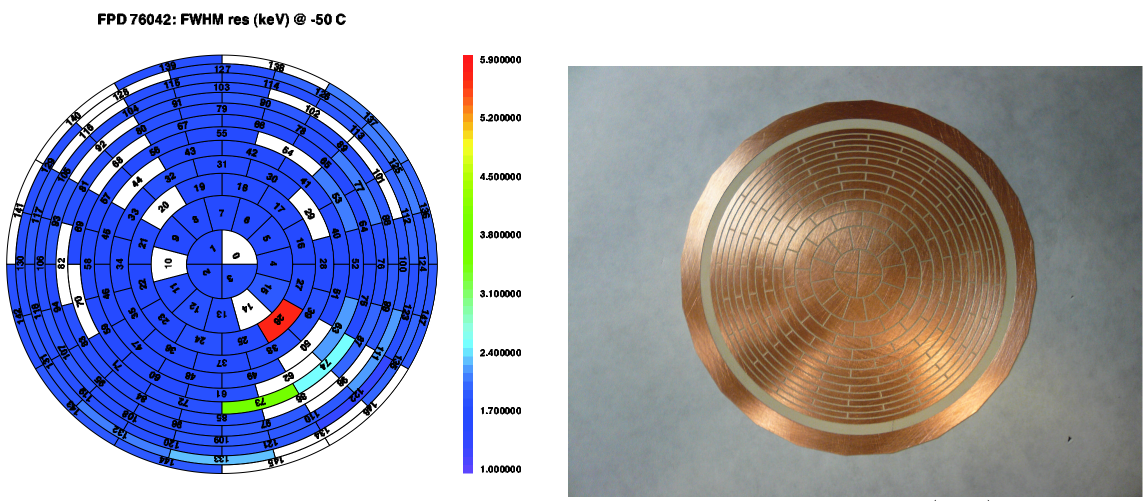

Figure 1.7-1. Left: The FWHM resolution of individual FPD pixels. Typical (blue) channels have 1.8 keV resolution for gammas at 60 keV. White channels are disabled and/or malfunctioning. The radially aligned missing channels between 10 and 11 o'clock are due to one entire preamp module which was laid aside for standalone testing. Right: A capacitive dummy used to extract the contribution due to detector leakage current.

Commissioning efforts now and in the near future are focused on understanding and mitigating the various contributions to the resolution. The discrepancy between achieved and expected resolutions is being investigated by measuring the FWHM resolution versus the shaping time (Fig. 1.7-2) and comparing to SPICE simulations. Direct measurements of the contribution from detector leakage current will be implied by measurements made with

[1]CENPA Annual Report, University of Washington (2009) p. 18.
[2]CENPA Annual Report, University of Washington (2009) p. 16.

a capacitive dummy (Fig. 1.7-1, right). This dummy is installed in place of a real detector and has similar pixel capacitance. Thus, resolution determined with a stable charge pulse generator will give the contribution due to everything except the shot noise on the leakage current. The performance of the system will be measured as a function of several parameters (primarily temperature, DAQ shaping time, and reverse bias potential) to find the optimum.

The system has already met minimum performance criteria required for it to be used in commissioning of the KATRIN main spectrometer. The detector still must meet its ultimate performance criteria required for neutrino mass measurements. Tests to be conducted in the coming months will indicate where performance of the system can be improved and we are confident that our goals can be met. The FPD and electronics will soon be installed in the KATRIN vacuum chamber so that commissioning of the entire detector section can begin.

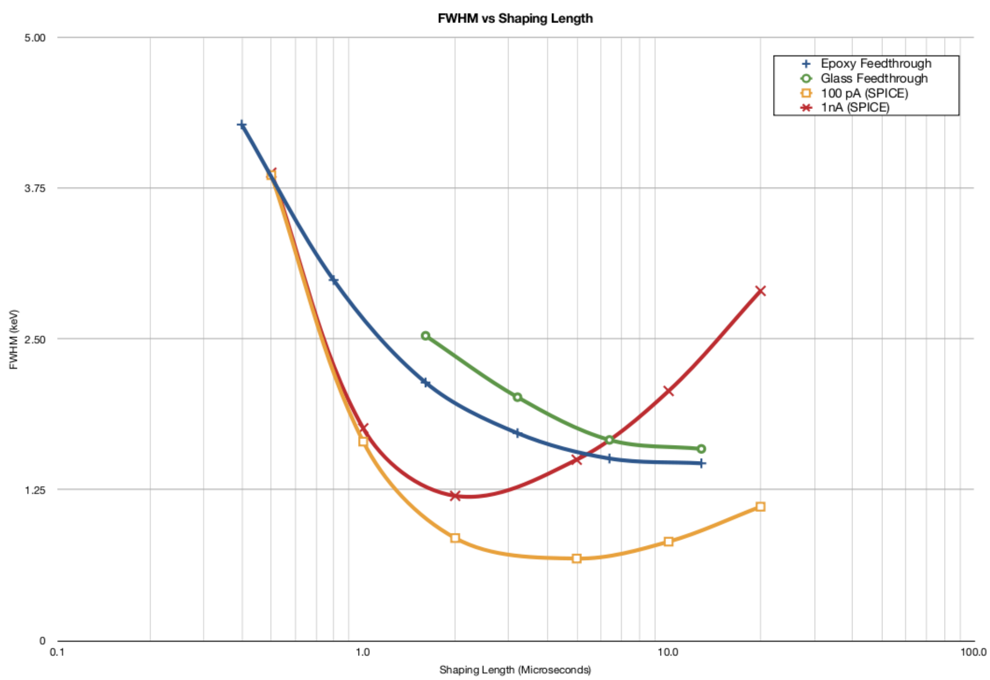

Figure 1.7-2. FWHM resolution versus shaping time for a single channel. The apparent difference in resolution between the epoxy and the glass feedthrough data is a consequence of using a different pre-amplifier. On average, detector-wide, no difference was seen between the two types of feedthroughs.

1.8 Status of the superconducting magnets for KATRIN

J. F. Amsbaugh, A. Beglarian*, L. I. Bodine, R. G. H. Robertson, and D. I. Will

The KATRIN detector section magnets[1] were manufactured by Cryomagnetics, Inc., Oak Ridge, TN and in November 2009, acceptance tests were performed at the factory. The magnets arrived at the university in January 2010 and were installed in the KATRIN lab in the Physics Astronomy building. The pair was run successfully at full field for a week of commissioning tests. The commissioning test results are in good agreement with the acceptance test results and the design specifications.

Both magnets are fully functional at 6 T with essentially no helium loss during running and minimal helium loss during ramping. The magnetic center of each magnet is within 2 mm of the mechanical center both axially and radially. The magnetic field drift is less than 2 ppb per hour, better than the design specification of 0.1% per month or 1.4 ppm per hour. Fig. 1.8-1 shows the axial magnetic field of the pair both as designed and as built.

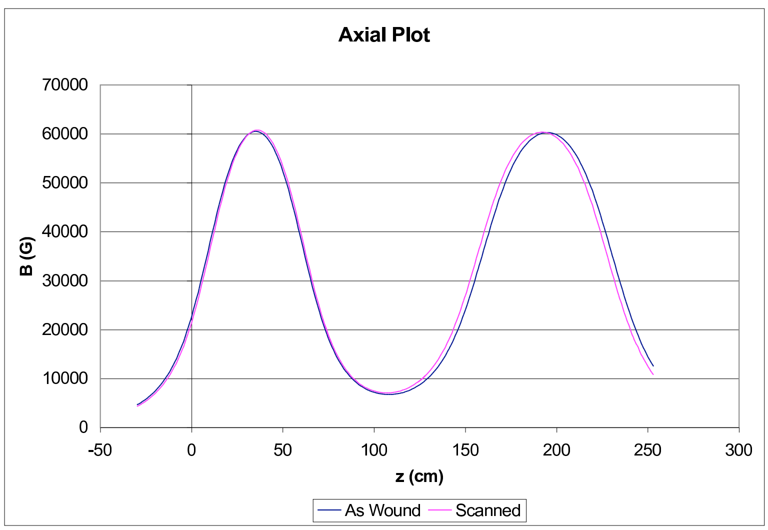

Figure 1.8-1. Axial field scan of the magnets as designed (blue) and as built (red)

The magnet commissioning has been completed and integration with other subsystems is in progress. The shield has been installed successfully in the detector magnet and the vacuum pump stand has been put in place between the magnets with the vacuum system extending through the detector magnet.

Integration of the magnet temperature sensors, level sensors, and power supplies with the KATRIN slow controls system has been completed. The magnet system is monitored in ORCA, the KATRIN Data Acquisition system, with email notifications of problems automatically sent to the relevant expert.

*Karlsruhe Institute of Technology, Karlsruhe, Germany.

[1]CENPA Annual Report, University of Washington (2008) p. 15.

1.9 Status of absolute calibration of KATRIN focal plane detector

E. L. Martin, D. A. Peterson, R. G. H. Robertson, and T. D. Van Wechel

In order to determine the absolute efficiency of the KATRIN focal-plane detector we intend to measure the electron current from a photoemissive electron gun and compare it to the count rate detected by the detector. This requires a current measurement of a femtoamp across a voltage of 20 kV.

PULCINELLA (precision ultra-low current integrating normalization electrometer for low-level analysis) is a current meter capable of measuring fA scale current. PULCINELLA consists of an integrator board floating at high voltage and a receiver board at ground. Power to the integrator board and output to the receiver board are optically isolated. Optical power isolation was accomplished by using an array of LEDs and a solar panel while data was transmitted over a fiber optic cable.

A copper disc is attached to a shaft which passes through a bellows to allow moving it in and out of the detector path. The integrator board is attached to the other side of the shaft outside of the vacuum along with the solar panel at high voltage. The LED array is mounted on a box at ground enclosing the high voltage components. UV light passes through a sapphire window to illuminate the photoelectode.

To allow for determination of the zero current offset the UV light will be pulsed and status of the light will also be sent to the receiver board and packaged with the charge measurement data. The receiver board converts the data to an ethernet signal which can be downloaded to a computer.

PULCINELLA was tested in a stand-alone vacuum system using a photocurrent of 2.3 pA. Using a Spellman high voltage power supply, noise was 300 $fA/\sqrt{Hz}$ at 20 kV. Using a low voltage, low noise power supply noise was 5 $fA/\sqrt{Hz}$. PULCINELLA was moved to the detector vacuum system and a filter was placed on the high voltage. Measurement of noise with no current was 50 $fA/\sqrt{Hz}$.

Majorana

1.10 Majorana Demonstrator activities

J. F. Amsbaugh, T. H. Burritt, J. Diaz Leon, P. J. Doe, M. A. Howe*, R. A. Johnson, M. G. Marino, M. L. Miller, A. W. Myers†, D. A. Peterson, R. G. H. Robertson, A. G. Schubert, T. D. Van Wechel, B. A. VanDevender, J. F. Wilkerson*, D. I. Will, and B. A. Wolfe

The Majorana Demonstrator collaboration is performing R&D to demonstrate the feasibility of building a 1-tonne modular array of 86% enriched ^{76}Ge capable of searching for neutrinoless double-beta ($0\nu\beta\beta$) decay in the inverted mass hierarchy region ($\sim$30 meV). A cornerstone of the plan is the development and construction of the Majorana Demonstrator, a R&D module comprised of 30 kg of 86% enriched ^{76}Ge and 30 kg of non-enriched Ge detectors. The use of a mixture of both enriched and natural or depleted Ge, has the advantages of lowering the costs in the R&D phase, accelerating the deployment schedule, and also giving the Majorana Demonstrator an opportunity to verify that any observed peak in the $0\nu\beta\beta$ region of interest is directly associated with the presence of ^{76}Ge. The goals for the demonstrator are:

- Show that backgrounds, at or below 1 count/ton/year in the $0\nu\beta\beta$ - decay peak 4-keV region of interest, can be achieved, a necessary condition for scaling to a 1 tonne or larger mass detector.
- Demonstrate sensitivity by testing the validity of the Klapdor-Kleingrothaus reported ^{76}Ge $0\nu\beta\beta$ observation[1].
- Show successful long-term operation of crystals in their respective environments.
- Demonstrate a cost-effective and scalable approach.

The proposed method uses the well-established technique of searching for $0\nu\beta\beta$ in high purity Ge (HPGe) diode radiation detectors that play both roles of source and detector. These detectors will be located in specially fabricated ultra low-background, electroformed Cu cryostats. The technique is augmented with recent improvements in signal processing, detector design, and advances in controlling intrinsic and external backgrounds. Major advances in detector R&D (both laboratory and industrial) have led to the choice of p-type point-contact (PPC) detectors for the demonstrator module. These detectors offer low capacitance and excellent resolution, providing the ability to (1) tag and veto two-site background interactions via pulse shape analysis and (2) probe ultra low-energy events (E>$\sim$300 eV) to competitively search for dark matter candidates (WIMPs, axions, etc)[2]. Project execution of the Majorana Demonstrator is currently underway. The 4850 ft underground laboratory at Soudan, MN is under preparation and the project is currently undergoing review by the DOE.

---

*University of North Carolina, Chapel Hill, N.C.

†Pacific Northwest National Laboratory, Richland, WA

[1] H. V. Klapdor-Kleingrothaus, I. V. Krivosheina, A. Dietz, and O. Chkvorets, Physics Letters B 586 198 (2004).

[2] C.E. Aalseth *et al.*, http://arxiv.org/abs/1002.470308

1.11 Surface-alpha measurements on HPGe detectors

T. H. Burritt, S. R. Elliott*, V. M. Gehman*, V. E. Guiseppe*†, R. A. Johnson, and J. F. Wilkerson‡

An alpha particle that loses kinetic energy before entering the active region of an HPGe detector will deposit only a fraction of its energy and might be mistaken for a neutrinoless double-beta decay ($0\nu\beta\beta$) event (Q-value in ^{76}Ge: 2039 keV). Alphas from the ^{232}Th and ^{238}U decay chains, particularly the ^{222}Rn daughter ^{210}Po, thus pose a background for $0\nu\beta\beta$ experiments such as MAJORANA and GERDA. Surface-alpha backgrounds can originate from the plateout of ^{210}Pb—a daughter of ^{222}Rn and progenitor of ^{210}Po. The 5.3 MeV alpha from the surface decay of ^{210}Po, if emitted at a shallow angle of incidence, can lose an appreciable amount of energy within the dead layer of a detector and become a background for $0\nu\beta\beta$.

We are finishing up the analysis of the surface-alpha test stand that we built[1] and ran[2] to study these surface-alpha backgrounds. Alphas from ^{241}Am were collimated at angles of 0°, 30°, 45°, and 60° incidence on an n-type HPGe detector surface. The data were compared with an analytic model based on charged-particle energy loss in matter as well as with Geant4 simulations. We have found that the Geant4 simulation underestimates the energy loss and the energy straggling that an alpha is subject to in the dead layer. A correction factor was applied to the simulation output to account for the deficit in energy loss and straggling. The data, analytic model prediction, and simulated spectra are shown in Fig. 1.11-1.

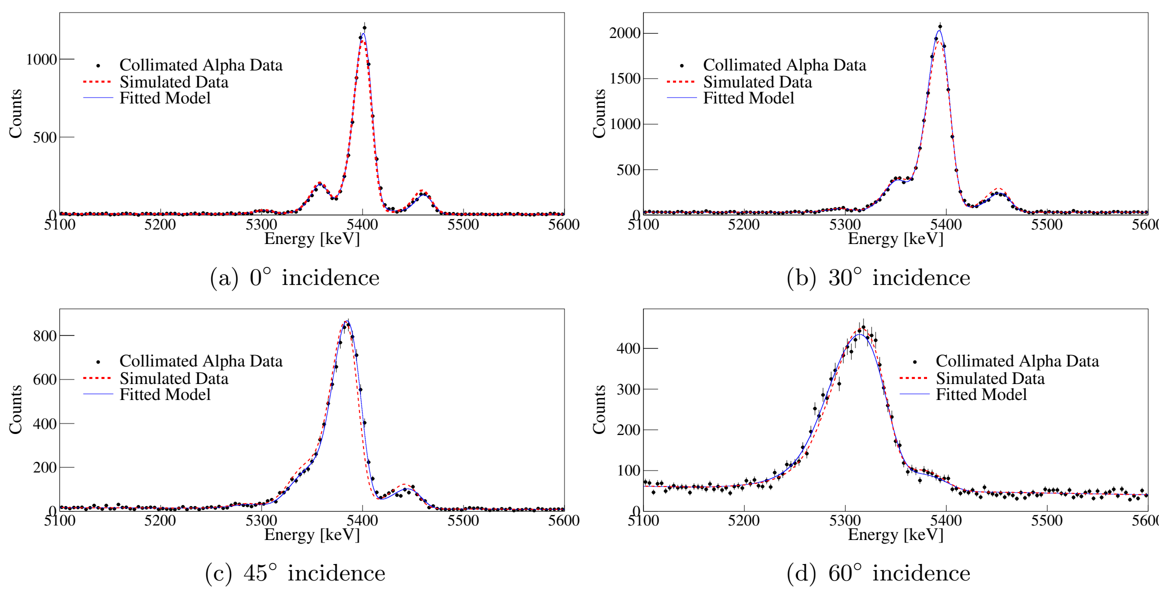

(a) 0° incidence

(b) 30° incidence

(c) 45° incidence

(d) 60° incidence

Figure 1.11-1. Collimated ^{241}Am alphas incident on an HPGe crystal surface. Data at four incidence angles are compared with predictions from an analytic model and from simulation.

*P-23, Los Alamos National Lab, Los Alamos NM, 87545
†Presently at University of South Dakota, Vermillion, SD 57069
‡Presently at University of North Carolina, Chapel Hill, 27599
[1]CENPA Annual Report, University of Washington (2008) p. 24.
[2]CENPA Annual Report, University of Washington (2009) p. 22.

1.12 A prototype DAQ system for the MAJORANA DEMONSTRATOR

M. A. Howe*, J. Diaz Leon, M. G. Marino, and J. F. Wilkerson*

The MAJORANA DEMONSTRATOR plans to deploy 60 kg of P-type point-contact (PPC) germanium detectors and to read these out with fast digitizers. These detectors have characteristics which make them desirable to be used in neutrinoless double-beta decay searches and dark matter searches (see Sec. 1.13), including low noise (low threshold) and long charge drift times. Both of these detector qualities enhance background reduction for double-beta decay and the low threshold increases sensitivity to dark matter. Development of a data acquisition (DAQ) system has been ongoing, investigating hardware specification needs to take full advantage of these detectors. In particular, the focus has been on minimizing both trigger threshold (< 1 keV) and the widths of peaks due to electronic noise.

Studies were performed using a PPC detector deployed at Soudan Underground Laboratory in Soudan, MN. This detector operated underground in the same shielded environment described in this report (see Sec. 1.13) for over 6 months. Software for the DAQ system has been developed in the ORCA DAQ and slow controls software package[1,2] at the University of North Carolina and at the University of Washington. The fast ADC used was the Mark IV digitizer designed by the Gretina collaboration[3]. The system was set up to facilitate remote control from outside the lab (e.g. from the University of Washington) as will be required by the MAJORANA DEMONSTRATOR. Some results of trigger efficiency tests measuring the ability of the electronics to trigger at low energies are given in Fig. 1.12-1(a). Results from studies looking at how the electronic noise scaled with the integration time of a digital trapezoidal filter are shown in Fig. 1.12-1(b). The results suggested that the capabilities of the Mark IV digitizer with its current firmware are insufficient and that either updates to the firmware would be required or different hardware should be selected.

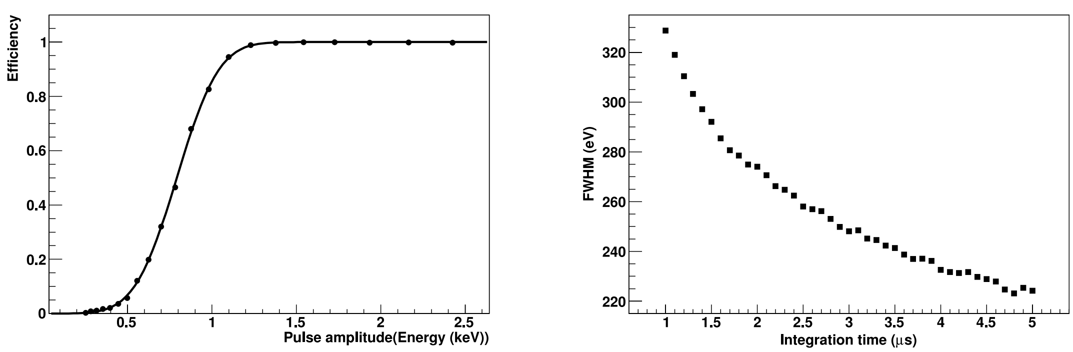

(a) Trigger efficiency, measured with an injected pulse of known amplitude.

(b) Noise versus integration time for a digital trapezoidal filter.

Figure 1.12-1.

*University of North Caroline, Chapel Hill, NC

[1] CENPA Annual Report, University of Washington (2001) p. 83.

[2] CENPA Annual Report, University of Washington (2007) p. 81.

[3] J. Anderson, et al., IEEE Trans. Nucl. Sci. **56**, 258 (2009).

1.13 Searches for direct detection of dark matter with a MAJORANA prototype

J. I. Collar*, M. G. Marino, M. L. Miller, J. L. Orrell†, and J. F. Wilkerson‡

P-type point contact (PPC) germanium detectors will be used in the MAJORANA DEMONSTRATOR because of their low noise and long charge drift times which make them well-suited for background reduction. The low noise of these detectors also allows a very low threshold (~ 0.5 keV) which makes them sensitive to low-mass WIMPs ≤ 10 GeV. A custom PPC BEGe (**B**road-**E**nergy **Ge**rmanium) detector from Canberra Industries similar to those to be used in the MAJORANA DEMONSTRATOR was deployed underground at the Soudan Underground Laboratory in Soudan, MN. Some care was taken to reduce backgrounds and some critical components internal to the detector cryostat were replaced with clean versions provided by J. Collar. This detector was placed underground in a shielded environment within a 2-inch inner shield of clean Pb from the University of Chicago and an 8-inch outer shield of less radiopure lead all inside a Rn-exclusion box. For mitigation of neutrons from cosmic-ray interactions in the rock walls of the lab, ~ 8 inches of borated polyethylene was placed surrounding the radon-exclusion box. The detector has been taking counting runs underground since 4 Dec 2009 and has demonstrated a threshold of < 0.5 keV. Analysis techniques have been developed to remove slow-rise-time pulses arising from poor charge drift and collection due to weak electric fields near the n^+ Li outer contact on the crystal[1]. This cut provides an effective fiducial volume cut on the crystal. Fig. 1.13-1 displays an example spectrum and an exclusion plot[1].

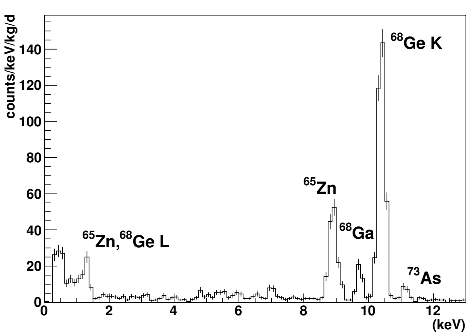

(a)

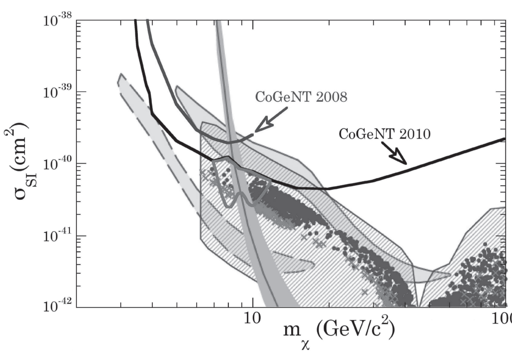

(b)

Figure 1.13-1. (a) Spectrum after 2 months of livetime with some prominent x-ray peaks from electron capture decays labeled. Noise peak (< 0.5 keV) is suppressed. (b) Exclusion plot, see text in reference[1] for details. CoGeNT 2010 refers to this work.

*University of Chicago, Chicago, IL

†Pacific Northwest National Lab, Richland, WA

‡University of North Carolina, Chapel Hill, NC

[1]Aalseth, et al., arXiv:1002.4703v2

1.14 Data management and workflow management for the MAJORANA DEMONSTRATOR

M. G. Marino, and M. L. Miller

The MAJORANA DEMONSTRATOR experiment is targeted squarely at scaling the deployment of enriched-Ge detectors from the well-established 1-10 kg scale to 100 kg and, ultimately, to 1 tonne. A major challenge in this enterprise is the automation of the data management and processing workflow management (DMWM). In the following we briefly highlight the design of a prototype DMWM system for the MAJORANA DEMONSTRATOR, lessons learned from continued operation with the prototype detector systems at Soudan Underground Laboratory, and the anticipated design for a system that scales to support 1 tonne of detectors. The MAJORANA DEMONSTRATOR will consist of 105 BEGe detectors, each having a low- and high-energy channel to span the energy range from ~300 eV to 10 MeV. A parallel DAQ system powered by ORCA (see Sec. 1.12) has been field tested at Soudan. The DAQ system generates data files in the ORCA binary format. These ("Tier-1") files are buffered underground, transferred via the WAN to CENPA for archival on durable storage, and converted to ROOT format ("Tier-2") for further processing. The ROOT files are then passed through iterative series of processing applications to create the MGDO encapsulation ("Tier-3") of event information (energy, timing, waveform data, etc). Finally, a series of flyweight analysis trees ("Tier-4") suitable for final analysis and publication are skimmed from the MGDO objects and published to a common cloud repository (Dropbox) for consumption by the entire collaboration. Every step in this process, including automated handling of calibration, run selection, etc, is fully automated and provenance tracked in the CouchDB database system that drives a custom python-based workflow management package. A prototype system was developed in Spring 2009 and deployed in Summer 2009 for DMWM of the Soudan prototype. It has been running reliably and efficiently for nearly a year and has managed data from three separate detectors installed at various times in Soudan.

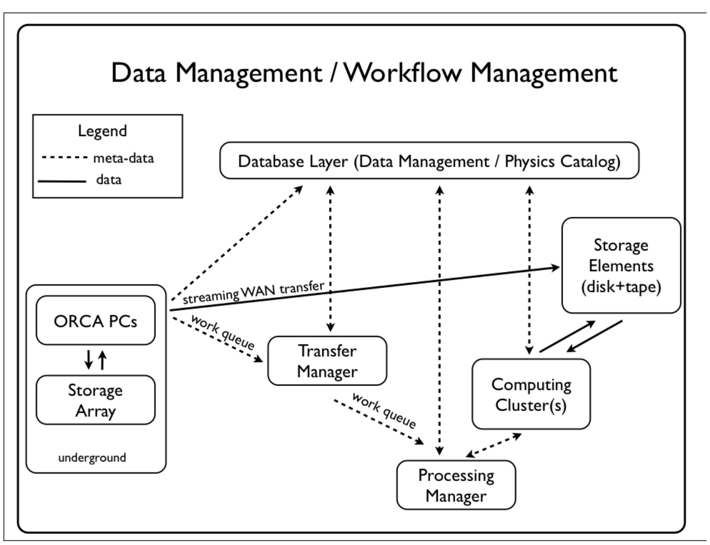

Figure 1.14-1. Schematic architecture of the production DMWM system.

1.15 Preparation and shipping of Pb bricks for the MAJORANA shield

J. Diaz Leon, M. L. Miller, R. G. H. Robertson, and D. I. Will

Old lead presently stored in the University of Washington's Atmospheric Sciences-Geophysics (ATG) building has been found to have very low radioactivity levels, thus providing a promising candidate for the MAJORANA detector's inner lead shield. A lead etching cleaning procedure has been established and shown to yield Pb bricks low in radioactive contaminants as well as potentially hazardous contaminants. Preparations to ship the bricks to the Deep Underground Science and Engineering Laboratory (DUSEL) at the Homestake mine near Lead, SD, are ongoing.

Due to its radiation-attenuating qualities, lead is being used as a passive shield from γ rays. The lead bricks themselves introduce a background from radioactive surface contaminants and embedded ^{210}Pb, and radio-assay results are required to evaluate the quality of the Pb. Presently, approximately 40 tons of lead bricks are housed in the ATG building. These pre-WWII lead bricks have an estimated value of a quarter million dollars and would represent a valuable asset if found to be sufficiently low in radioactive contaminants.

In order to improve the radio-purity of the lead, an etching procedure was designed to remove surface contamination by essentially exposing a new lead surface. The bricks are first cleaned with ethanol to remove most dirt, then placed in acid baths[1] where the lead oxide surface reacts to create lead salts (lead acetate and lead nitrate), which are particularly soluble in water. This surface layer is subsequently scrubbed off in water. This procedure was employed to clean the ATG lead bricks as well as commercial lead bricks[2].

Preliminary results from radio-assay[3] suggest the cleaning procedure yields Pb bricks with low backgrounds from surface contaminants. Also, the ATG lead bricks show no sign of ^{210}Pb, whereas this background signal is clearly visible in the commercial lead. Due to their previous use and location, the ATG Pb bricks were initially found to have surface contamination of Hg. As demonstrated by tests performed at CENPA, the cleaning procedure also serves to remove this potential health hazard.

Plans to extract the Pb housed in ATG and ship it to DUSEL, where it will be used, are in progress. In order to accommodate the transportation of 40 tons of Pb (approximately 20 lbs per brick), pallets have been constructed at CENPA (80 bricks per pallet) and are ready for use.

[1] Separate baths of glacial acetic acid and 10% nitric acid

[2] Sullivan Metals, Inc. www.sullivanmetalsinc.com

[3] Performed by colleagues from University of North Carolina at KURF

1.16 Simulated response of a MAJORANA detector string to ^{68}Ge

R. J. Cooper*, J. A. Detwiler†, R. Henning‡, D. C. Radford* A. G. Schubert, and J. F. Wilkerson ‡

The sensitivity of the MAJORANA experiment is limited by the presence of backgrounds in the $0\nu\beta\beta$ energy region of interest. MAJORANA will use several analysis techniques to distinguish potential neutrinoless double-beta decay events from background events. Events depositing energy in more than one detector or events depositing energy in multiple sites in one detector can be identified as background events. A model of the background energy spectrum is necessary to determine whether the DEMONSTRATOR achieves the MAJORANA background goal and to interpret results of the $0\nu\beta\beta$ search.

Monte Carlo simulations with MaGe, a Geant4-based package developed by the Gerda and MAJORANA collaborations, have been used to study detector response to expected backgrounds. Pulse-shape analysis emulation code can be applied to MaGe results to predict the ability of the experiment to distinguish single-site from multiple-site interactions. Response of a five-detector string to ^{68}Ge, a cosmogenically-induced background, is shown in Fig. 1.16-1. Analysis cuts can reduce this background by an order of magnitude in the $0\nu\beta\beta$ energy region of interest.

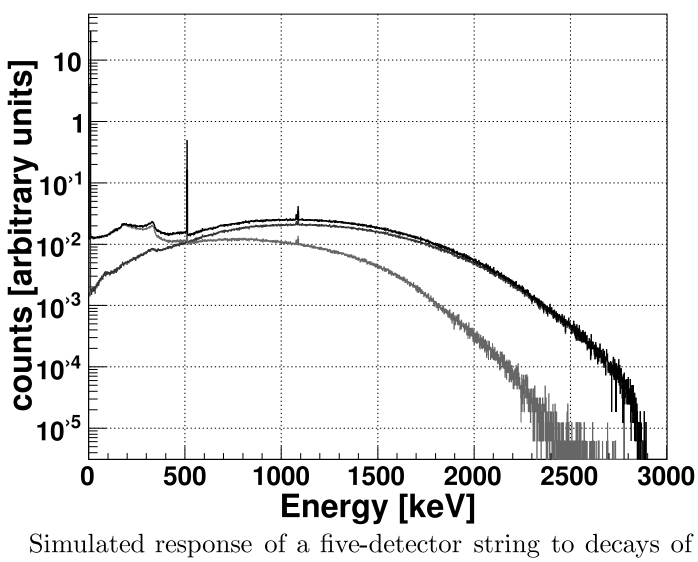

Figure 1.16-1. Simulated response of a five-detector string to decays of ^{68}Ge in the top detector: all counts (black), counts that pass a crystal-to-crystal granularity cut (dark grey), counts that are identified as single-site events (grey).

*Oak Ridge National Laboratory, Oak Ridge, TN, USA
†Lawrence Berkeley National Laboratory, Berkeley, CA, USA
‡Department of Physics, University of North Carolina, Chapel Hill, NC, USA and Triangle Universities Nuclear Laboratory, Durham, NC, USA

1.17 Thermal and vacuum measurements from a prototype MAJORANA cryostat and string

T. H. Burritt, S. R. Elliott*, V. M. Gehman*, V. E. Guiseppe†, S. P. MacMullin‡, A. G. Schubert, and J. F. Wilkerson ‡

The MAJORANA collaboration will search for neutrinoless double-beta decay with an array of germanium crystals enriched in ^{76}Ge. The germanium crystals will be deployed in vertical strings of four to five detectors and will be housed in radiologically-pure copper cryostats.

Strings for the MAJORANA experiment must be constructed from ultra-pure materials and maintain proper thermal and electrical operating conditions for Ge detectors. A prototype string was fabricated and is shown in Fig. 1.17-1. This string contains four detector blanks that approximate the thermal mass of germanium detectors. The string is instrumented with four resistive heaters that simulate the heat load of detector electronics.

A test cryostat at Los Alamos National Laboratory was used to test thermal properties of string designs for MAJORANA. The prototype string was deployed in this cryostat. Silicon diode sensors measure temperatures within the cryostat and on the string. Temperature data were collected while cooling the cryostat with liquid nitrogen and while operating the resistive heaters. These data will be used to evaluate the string design.

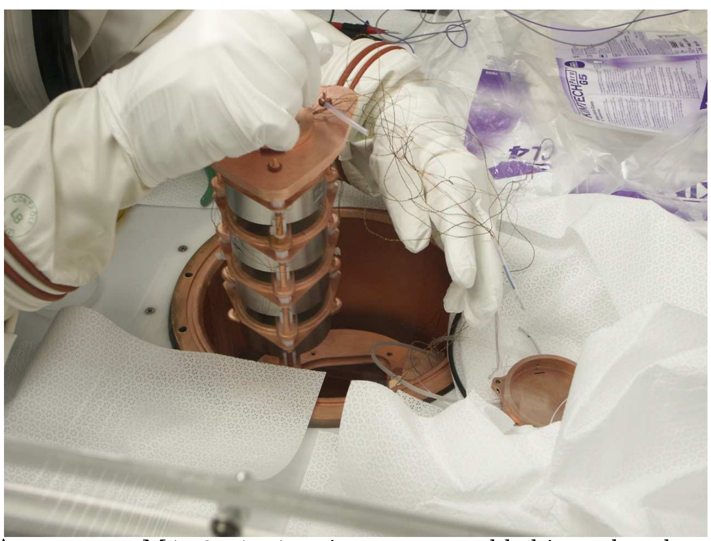

Figure 1.17-1. A prototype MAJORANA string was assembled in a glove box and deployed in the test cryostat. The string is instrumented with temperature sensors and heaters to simulate the thermal load of detector electronics.

*Los Alamos National Laboratory, Los Alamos, NM, USA.
†Department of Physics, University of South Dakota, Vermillion, SD, USA.
‡Department of Physics, University of North Carolina, Chapel Hill, NC, USA and Triangle Universities Nuclear Laboratory, Durham, NC, USA

1.18 Design and fabrication of ultra-low background parylene-copper ribbon cable for MAJORANA

T. H. Burritt, D. A. Peterson, M. L. Miller, A. W. Myers*, R. G. H. Robertson, and B. A. Wolfe

The radioactive background goal of MAJORANA is 1 count per ton-year in the region of interest. Because all commercial cable options are too radioactive, MAJORANA intends to reach this goal by making signal cables out of parylene and copper. Parylene is a polymer that has Th background limits of < 91 ppt and U limits of < 2.2 ppb. Other benefits from using parylene include its low leakage current and low dielectric constant. We are developing a 4-wire ribbon cable consisting of copper wires surrounded by parylene that is applied by a deposition chamber (Fig. 1.18-1). Production will occur in a class-1000 clean room located in the Physics Astronomy Building (B037).

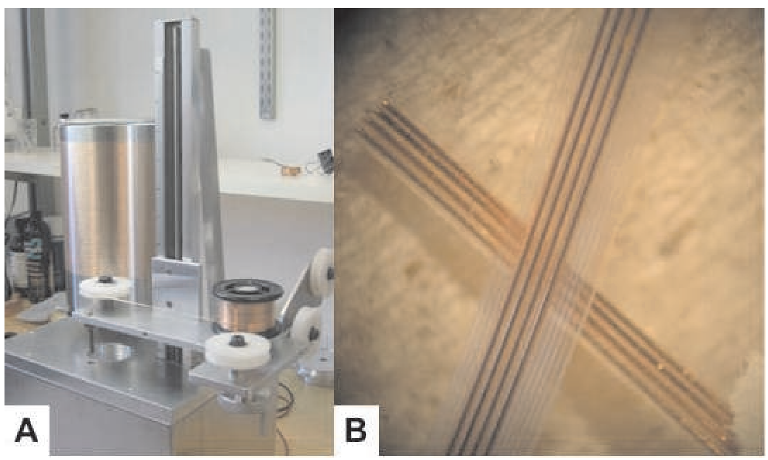

Figure 1.18-1.
A: Unwinding the ribbon cable onto a spool using the production winder.
B: Close up of the parylene ribbon cable. The inter-wire spacing is 0.006".

The ribbon cable will be created using a LABCOATER 2010[1] deposition chamber. Deposition of parylene is unlike the deposition of other materials because of its lack of a liquid form. Normally the vacuum must be held to 10^{-5} Torr or less, but parylene can be uniformly coated at pressures 100 times greater than this. Normally the liquid form of any deposition can create pooling and edge-effect flaws.

The ribbon cable consists of four 0.003" diameter copper wires. The spacing between wire centers is 0.006" (for a 0.003" gap between wires). The deposition process consists of coating a grooved cylinder with parylene, then wrapping the four strands of wire around the parylene coated cylinder and depositing a final coat of parylene. The wire is wound and cut by an apparatus (Fig. 1.18-1) developed by Tom Burritt. In one run we produced 160 ft of cable. We recently made 100 ft of cable (outside of the clean room), and measured a 0.79 m

*Pacific Northwest National Laboratory, Richland, WA
[1]Specialty Coating Systems, Inc., Indianapolis, IN

section for impedance and capacitance. We had predicted an impedance of 97 Ω for the cable and measured the actual impedance to be 110±10 Ω. A small capacitance is crucial to our low noise goal. Table 1.18-1 lists the three capacitances of the wire.

Future work includes moving the deposition system permanently into the clean room and making a clean version of the ribbon cable. We are also considering the use of parylene for other parts of the MAJORANA experiment because of its ultra-low background. Development for parylene cryostat gaskets is currently under study.

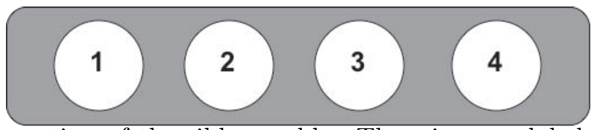

Figure 1.18-2. Cross section of the ribbon cable. The wires are labeled 1, 2, 3, and 4 to correlate with the pairs referenced in Table 1.18-1.

Wire Pair(s)	Predicted Capacitance (pF/foot)	Measured Capacitance (pF/foot)
1-2, 2-3, 3-4	16.6	16.8±0.2 (average)
1-3, 2-4	10.8	9.9±0.2 (average)
1-4	9.1	7.7±0.2 (average)

Table 1.18-1. Capacitance measurements on 0.79 m of ribbon cable. The wire numbers correlate with those in Fig. 1.18-2.

Project 8

1.19 Status of the Project 8 neutrino mass measurement prototype

L. I. Bodine, R. Bradley*, P. J. Doe, J. Formaggio†, R. A. Johnson, J. Kaspar, M. L. Leber‡, M.L. Miller, B. Monreal‡, M. F. Morales, R. G. H. Robertson, L. J. Rosenberg, G. Rybka, W. A. Terrano, T. Thuemmler§, and B. A. VanDevender

Neutrino mixing experiments indicate the average neutrino mass must be greater than 0.02 eV. The KATRIN experiment has a target neutrino mass sensitivity of 0.2 eV. If the neutrino mass is not within the reach of the KATRIN experiment, it will almost certainly be within the reach of an experiment an order of magnitude more sensitive. The Project 8 group is exploring ideas for a next-generation experiment sensitive to neutrino masses in the 0.02-0.2 eV mass range. Even in the event of a null measurement, such an experiment will be able to distinguish between normal and inverted hierarchies of neutrino mass.

Measuring the tritium beta decay endpoint spectrum is still the most attractive means to get at the neutrino mass, but a spectrometer with the required sensitivity would be prohibitively large. Another way of measuring the spectrum is to allow the emitted electrons to spiral in a magnetic field and measure the frequency of their cyclotron radiation, as in Fig. 1.19-1, a conceptual sketch of the technology[1]. Experiments in Penning traps, such as those measuring the electron magnetic moment, have shown that frequency measurement is a very powerful tool for precise energy determination.

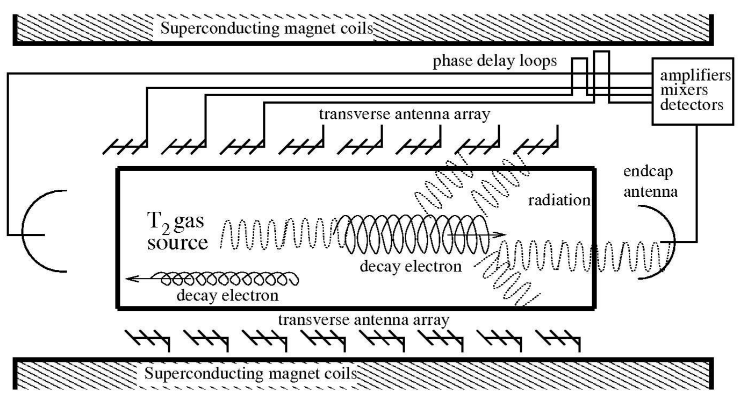

Figure 1.19-1. A conceptual sketch of the technology. Multiple antennas are used to image the path of electrons from tritium beta decay. The energy is determined from the frequency.

The goal of Project 8 is to produce a prototype (Fig. 1.19-2(b)) that demonstrates electron energy measurement using cyclotron radiation. This prototype will allow us to test different

*National Radio Astronomy Observatory
†Massachusetts Institute of Technology
‡University of California, Santa Barbara
§Karlsruhe Institute of Technology
[1] "Relativistic Cyclotron Radiation Detection of Tritium Decay Electrons as a New Technique for Measuring the Neutrino Mass," B. Monreal and J. Formaggio, April 2009. arXiv:0904.2860v1 [nucl-ex]

antenna and magnetic field configurations to optimize energy resolution. Once operational, the prototype will be used as a basis for design of larger experiments capable of precision measurements of nuclear decay spectra, with the eventual goal of determining the neutrino mass by way of the tritium beta decay spectrum.

In addition to ongoing basic physics analysis and design work, hardware development has begun. A superconducting solenoidal magnet, whose past involves the 1989 Nobel-prize winning experiments of Hans Dehmelt, was donated to our group. The magnet has been in storage for well over ten years but is currently being restored to working order (Fig. 1.19-2(a)).

(a) Superconducting magnet recommissioning

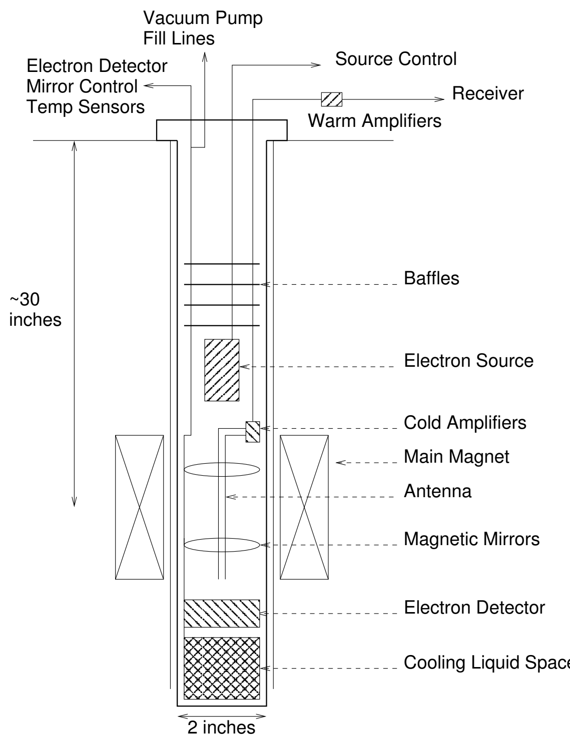

(b) Conceptual design of prototype insert

Figure 1.19-2. The superconducting magnet necessary for the Project 8 Prototype and the insert

We have also begun to develop in-house capability to produce ^{83m}Kr calibration sources by irradiating cells of natural Kr with protons from the CENPA tandem accelerator. Current schedules indicate that a functional prototype should be constructed by the end of 2010, allowing tests of this novel technique to begin in 2011.

Large Detector

1.20 Investigations into the feasibility of a very large liquid scintillator detector for next generation long baseline neutrino experiments

S. Enomoto, J. Kaspar, N. R. Tolich, and H. S. Wan Chan Tseung

The primary objectives of the next-generation neutrino experiments are to determine θ_{13}, the neutrino mass hierarchy, and to observe CP violation in the lepton sector. To achieve these goals, it has been proposed to direct a muon neutrino (ν_μ) beam of GeV energy onto a large (>100 kton) underground neutrino detector and study ν_e appearance[1]. So far extensive studies have been made on two large neutrino detector concepts: the well-established water cherenkov detector, and a detector filled with liquid argon. Recently, a liquid scintillator option has also been proposed by J. Learned[2]. Such a detector would benefit from superior light yield and, therefore, better energy resolution and lower energy threshold.

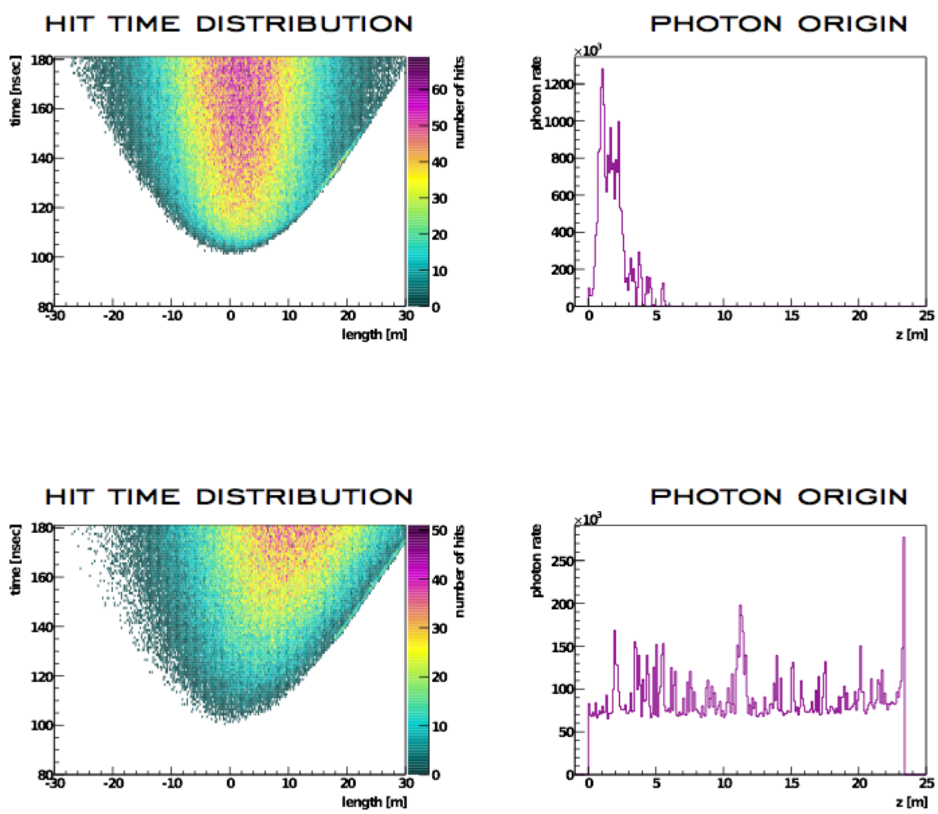

Figure 1.20-1. Top row: simulation of a 5 GeV electron in a large liquid scintillator detector, showing the phototube hit time distribution (left) and the distribution of scintillation photons along the particle track (right). Bottom row: the same for a 5 GeV muon.

[1] V. Barger *et al.*, arXiv:0705.4396v1

[2] J. G Learned, arXiv:0902.4009v1

We have begun feasibility studies for a large liquid scintillator detector at CENPA. A central issue is whether or not electrons produced in quasi-elastic ν_e scattering can be distinguished from other particles such as muons and pions. To address this problem a basic model of a prototype cylindrical detector has been built using Reactor Analysis Tool, the Geant4-based SNO+ Monte Carlo package. The detector simulation assumes LAB-PPO scintillator, whose properties (including absorption, re-emission, scattering, and quenching) are handled by `GLG4Scint`. Neutrino interactions are generated with the GENIE package[3], and a rudimentary data acquisition simulation is included.

Fig. 1.20-1 shows typical simulations of a 5 GeV electron (top row) and a 5 GeV muon (bottom row), both starting at the center of the detector and moving upwards along z. The phototube hit time distribution in each case is shown on the left and the z co-ordinate of the photon origin is plotted on the right. We find that electrons and muons differ by the uniformity of photon production along the particle trajectory. This means that track reconstruction (see Sec. 1.21) is very important for identifying electrons. The simulation has been used to propagate neutrino interaction events for testing our track reconstruction algorithm. In the near future we plan to use this algorithm to derive suitable parameters for robust electron discrimination. Work is also in progress to study charged and neutral pion separation from electrons.

[3] C. Andreopoulos *et al.* Nucl. Instrum. Meth. **A614** (2010) 104.

1.21 Reconstructing the light production distribution in a liquid scintillator detector

S. Enomoto, J. Kaspar, N. R. Tolich, and H. S. Wan Chan Tseung

We have begun feasibility studies for a large liquid scintillator detector as discussed in another article in this report (see Sec. 1.20). Particle types (primarily electron or muon) will be identified by looking at the different photon production patterns along tracks. For the same initial energy at the GeV scale, electron events tend to be short and wide due to electromagnetic showers while muon events tend to be long and narrow. A muon-decay electron associated with a muon event could be observed which further helps particle identification.

Fig. 1.21-1 shows examples of MC-generated photon production distribution, one 5 GeV electron event, and one 5 GeV muon event, respectively. One can see that the *shapes* of the photon production distributions are quite different from each other, and reconstruction of the light production distribution with enough resolution would enable us to identify the particle types. An event reconstruction algorithm is being developed to allow a quantitative study of particle identification ability, and also to find an optimal detector design.

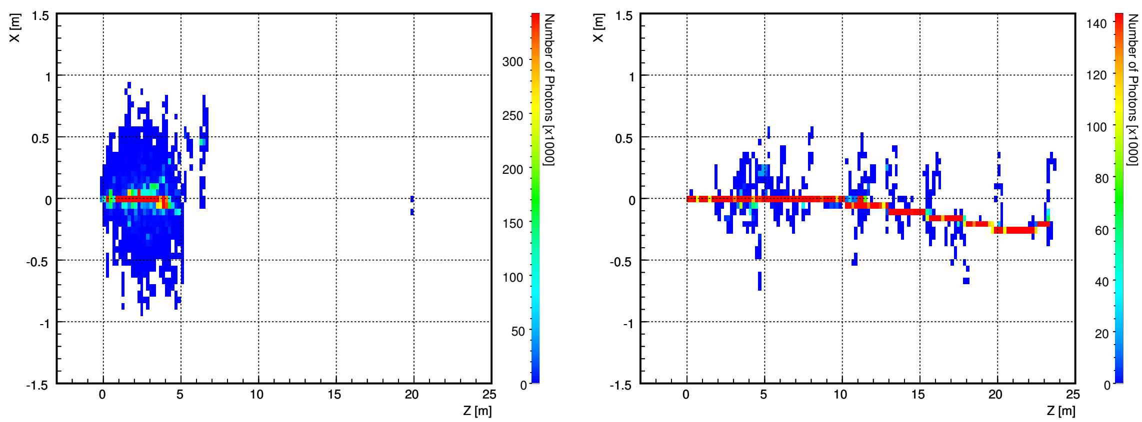

Figure 1.21-1. Light production distribution of MC generated events in liquid scintillator: One 5 GeV electron event (left) and one 5 GeV muon event (right), both started at the center of the detector ((x,y,z)=(0,0,0)) and moving to the +Z direction.

Traditionally, event reconstruction in a large scintillator detector has been done mostly by utilizing the maximum likelihood method, or similar/equivalent statistical methods, including geometrical (pre)*fits*, by assuming a single point as a vertex and/or single line(segment) as a track. Although this statistical method is optimal in terms of "maximum likelihood", it only gives the best set of parameters among given models, such as single vertex, track, etc. For a GeV scale neutrino interaction in a large scintillator detector, event topology will be far more complicated, possibly including multiple tracks, multiple showers and multiple isolated vertexes. This makes *fitting* based on event topology models much more difficult.

This study attempts to separate event reconstruction from model fitting. Since photon production is a process that occurs after physics interaction, reconstruction of photon production distribution should be possible without assuming physics models (i.e., event topology). If the photon production distribution were reconstructed with enough accuracy and resolution, event characteristics, such as showers and tracks, could be obtained at this stage and a physics model to fit could be determined. Fitting physical models to photon production distribution should be easier than fitting to photon detection distribution (PMT hit distribution) since parameters are more directly related to the statistical variables.

The reconstruction method used in this study is based on the Hoff transform; each PMT hit defines a set of points in the (x, y, z, t) space where the detected photon could have been produced, and takes the superposition of the sets. The Hoff transform itself does not directly give the production distribution, but it transforms hit-time distributions into more convenient space as shown below. Another advantage of the method is that the algorithm does not depend on any particular detector geometry and construction, which is an important feature for the work to find an optimal detector design.

Fig. 1.21-2 shows the result of the Hoff transform for the MC events shown in Fig. 1.21-1. A major difficulty of this method is the amount of calculation, and an adaptive thinning-out algorithm that reduces the calculation time to typically shorter than 1/1000 was developed and implemented. In the figure, only calculated points are shown as colored pixels, and due to the adaptive nature of the thinning-out algorithm, only the points surrounding the photon production points are calculated.

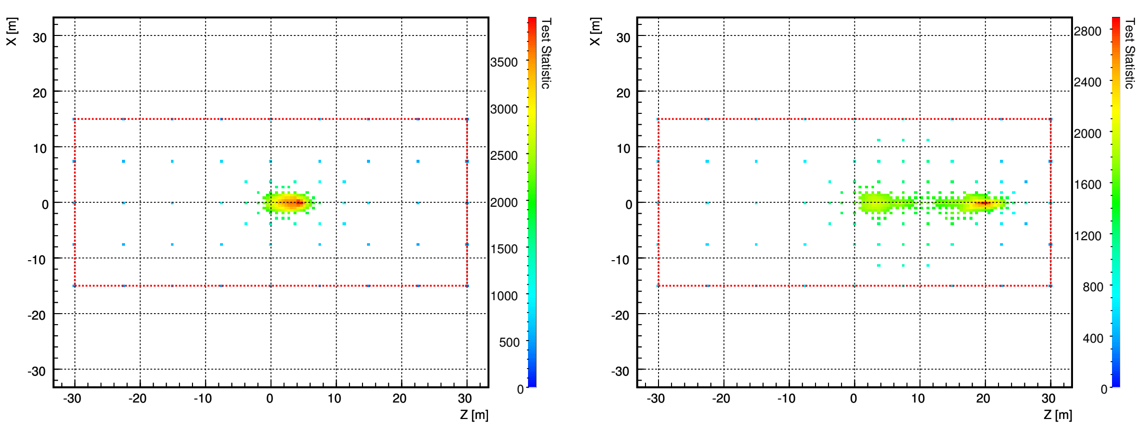

Figure 1.21-2. Reconstructed light production distribution: One 5 GeV electron-neutrino event (left) and one 5 GeV muon-neutrino event (right). Red dot lines indicate the size of the detector used in this study (cylinder with 30 m diameter and 60 m length)

Extraction of event characteristics from the transform result is underway. However, one can see that some important event characteristics, such as *length* of the *shape*, which may correspond to ionization characteristics, are already well visible. Currently the resolution is limited by broadened photon arrival time distribution due to photon absorption and re-emission in the scintillator. Various methods to improve the hit-time resolution are being examined.

HALO

1.22 The HALO supernova detector

C. A. Duba*, F. Duncan†‡, J. Farine‡, A. Habig§, A. Hime¶, M. A. Howe††, C. Kraus‡, R. G. H. Robertson, K. Scholberg‖, M. Schumaker‡, J. Secrest**, T. Shantz‡, C. J. Virtue‡, J. F. Wilkerson††, S. Yen‡‡, and K. Zuber[a]

HALO (Helium And Lead Observatory) is under construction at SNOLAB in Canada at a depth of 6000 m water equivalent. It is intended as a low-cost, low-maintenance neutrino detector sensitive to a nearby galactic supernova. The operating principle is based on the strength of neutrino charged-current transitions from the ground state of ^{208}Pb to neutron unstable states in ^{208}Bi, and also neutral-current excitations above the neutron-emission threshold in ^{208}Pb. At HALO's present size, with 76,000 kg of Pb, the intense neutrino flux from a supernova at 10 kPc would produce a burst of neutrons lasting several seconds, about 40 of which would be detected. As the galactic center is at 8 kPc and signals smaller than 40 neutrons can reliably be detected, most of the galaxy will be covered. The device is modular and can be expanded for still greater sensitivity. The more energetic neutrinos may liberate 2 neutrons in fast time coincidence, giving, in addition to rate, a crude spectroscopic measure of energy and hence temperature.

Figure 1.22-1. The HALO detector lead stack completed as of April, 2010.

*Digipen Institute of Technology, Redmond, WA 98052
†SNOLAB, Sudbury, ON P3Y 1M3, Canada
‡Laurentian University, Sudbury, ON P3E 2C6, Canada
§University of Minnesota Duluth, Duluth, MN 55812
¶Los Alamos National Laboratory, Los Alamos, NM 87545
††University of North Carolina, Chapel Hill, NC 27599
‖Duke University, Durham, NC 27708
**Armstrong Atlantic State University, Savannah, GA 31419
‡‡TRIUMF, Vancouver, BC V6T 2A3, Canada
[a]TU Dresden, D-01062 Dresden, Germany

The neutrons are moderated in polypropylene tubes and detected in an array of ^{3}He:CF$_4$ proportional counters that formerly served as the neutral-current detection array in SNO. Four counters fill each aperture in the stack of lead blocks salvaged from the decommissioned Deep River cosmic-ray neutron monitor (see Fig. 1.22-1).

Since the counters were made at CENPA, we are participating in HALO by providing some assistance with recommissioning them. The preamplifiers are being modified from current readout to charge readout to improve the signal-to-noise ratio. Splitters will connect two counters to each of 64 channels. The shaper-ADC cards will be replaced with versions suitable for charge readout. Our colleagues at the University of North Carolina are configuring the ORCA data acquisition system.

Funding for the construction of HALO is being provided by NSERC (Canada).

2 Fundamental Symmetries and Weak Interactions

Torsion Balance Experiments

2.1 Current status on improved equivalence principle limits for gravitational self-energy

E. G. Adelberger, J. H. Gundlach, B. Heckel, S. Schlamminger, and T. A. Wagner

Lunar laser ranging limits the strength of an equivalence-principle-violating interaction by comparing the Earth's and Moon's accelerations toward the sun. However, the Earth's and Moon's compositions as well as their gravitational self-energy differ. To test the equivalence principle solely for gravitational self-energy, we test for a composition-dependent acceleration difference of earth-like and moon-like test bodies toward the sun. We expect improvements from this composition dependent measurement combined with lunar laser ranging results will limit an equivalence principle violation for gravitational self-energy to a few parts in 10^4.

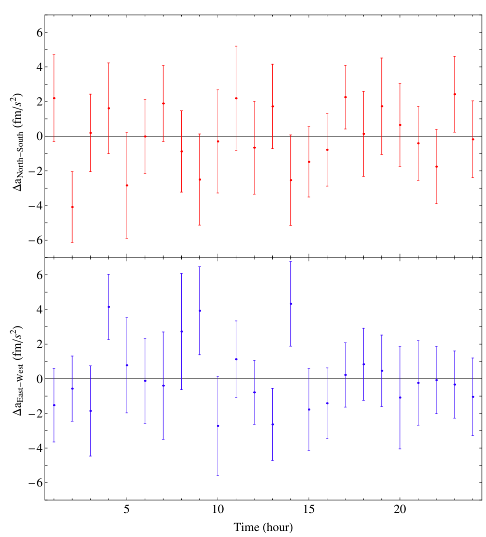

Figure 2.1-1. Daily component of the differential acceleration toward the sun in the North-South (upper) and East-West (lower) directions.

Our rotating torsion balance uses a composition dipole that mimics the difference in the Earth's and Moon's compositions. We have collected approximately 160 days of data over the past two years, with data collection ongoing. A portion of this data suffers from excess noise due to vacuum system pressure spikes, which have been ameliorated through recent apparatus updates. A preliminary analysis of this data leads to a 1-σ statistical uncertainty in $\Delta a_{CD}/a_s$ towards the sun of 1.4×10^{-13}. Baeßler *et al*[1] previously measured $(+0.1 \pm 2.7 \pm 1.7) \times 10^{-13}$. A signal would appear in Fig. 2.1-1 as a daily modulation in both components.

[1]S. Baeßler, B.R. Heckel, E.G. Adelberger, J.H. Gundlach, U. Schmidt, and H.E. Swanson, Phys. Rev. Lett. **83**, 3585-3588 (1999).

2.2 Parallel plate test of Newton's gravitational inverse square law

J. H. Gundlach, C. A. Hagedorn, S. Schlamminger, and M. D. Turner

We have continued work on a new torsion balance for a parallel plate test of the gravitational inverse square law[1]. We have nearly completed upgrades to the apparatus that address the most important sources of systematic uncertainty, undertaken a preliminary science campaign, contributed several months of time to our investigation of "Squeeze-film Damping" (see Sec. 2.8), further improved our data analysis, and made other improvements to the apparatus. In addition to understanding the systematic effects better, we are now able to hold our pendulum in feedback lock at the smallest pendulum-foil distances yet.

In our experiment, a torsion pendulum is suspended within tens of microns of a dense planar "attractor". The attractor is moved near and far from the pendulum and we study their mutual gravitational interaction. To ensure that their only interaction is gravitational, an electrically grounded beryllium-copper foil is tightly stretched between them. Effective shielding is only achieved if the foil does not move when the attractor is displaced. We built a fiber Fizeau interferometer to continuously monitor the foil displacement with subnanometer precision. The interferometer works well, and needs only improved laser frequency stabilization before it will fully meet our requirements.

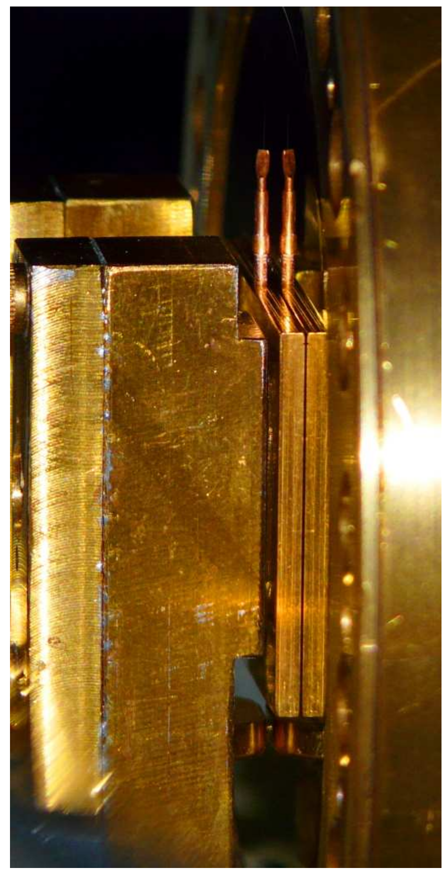

Figure 2.2-1. The pendulum and its reflection in the foil. Upgraded electrodes are seen at left. The optical fiber interferometer protrudes just below the pendulum. The 2 mm thick pendulum is locked in electrostatic feedback.

Further activities include: detailed studies of surface/contact potentials between the pendulum and foil, clear detection of the "microseismic peak" of seismic noise at frequencies near 100 mHz, improved signal routing and conditioning to reduce electronic interference, the installation of tilt sensors on the apparatus, the installation of ground-shielded feedback electrodes, in-vacuum sideways displacements of the pendulum, and more. Improvements to our data analysis have come through optimized windowing and the adoption of attractor motion schedules that allow the study of systematic effects in parallel with signal gathering.

At distances larger than 160 μm from the foil, the experiment nearly reaches the thermal torque noise limit. At shorter distances, we have been limited in torque sensitivity by a compliant piece of dust, despite our cleanroom environment. We expect to be able tore-move this noise source soon.

[1] CENPA Annual Report, University of Washington (2009) p. 27.

2.3 Wedge pendulum progress report: data and analysis

E. G. Adelberger, T. S. Cook, B. R. Heckel, and H. E. Swanson

We have completed taking a set of data with a pendulum and attractor consisting of tungsten wedges glued to a pyrex substrate and analyzed it for Yukawa deviations from the inverse square law. The results improve limits in the regime below λ =50 μm. The new limits, however, are not as good as expected, so improvements are underway in preparation for a second set of data that should be significantly more sensitive.

At first, our data seemed to have an anomalously large ratio of the 18-wedge signal to the 120-wedge signal. We were able to account for this by introducing parameters that handled the non-flatness of the pendulum and attractor surfaces. We introduced a parameter known as the *glue gap* that treated the surface of the glue as being recessed an average distance from the surface of the tungsten. Importantly, the 18-wedge signal has a larger *glue gap* (about 17 μm) than the 120-wedge signal (about 12 μm). We also introduced a *cone* parameter that accounts for the over-all non-flatness of the surfaces. The surface is coned due primarily to differences in the thermal expansion of tungsten and Pyrex during the gluing process. It is also affected by added stresses from attaching the Pyrex to the pendulum body or attractor holder. We found that the 18 wedges were on average 10 μm closer than the 120 wedges. Both of these parameters greatly helped the model fit the data. While values for these parameters were initially unknown, they have since been measured with great precision with the newly acquired OGP ZipLite SmartScope with DRS 500 laser attachment. It can perform non-contact characterization of surfaces with $<$1 μm precision. See Fig. 2.3-1.

Our limits were not as stringent as expected primarily because we were unable to take data with the pendulum to attractor separation as close as anticipated (achieving only $s = 75$ μm) because of coning. Using a new technique for attaching the Pyrex to the pendulum body, we can counteract the coning to produce a nominally flat pendulum surface. We hope to take additional data with $s \leq 60$ μm in the near future.

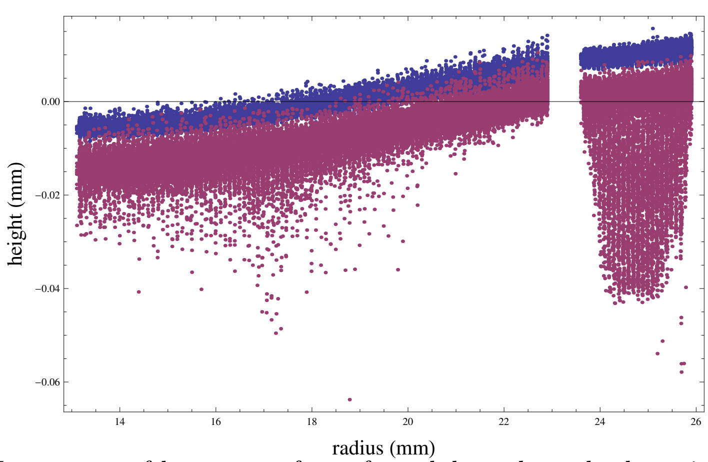

Figure 2.3-1. Laser scan of bottom surface of pendulum shows both coning and height separation of the tungsten surface (blue) from the glue surface (red).

2.4 Progress on a torsion balance test of new spin coupled forces

E. G. Adelberger, B. R. Heckel, and W. A. Terrano

The torsion balance experiment to measure spin dependent forces[1] is nearly ready for commissioning. All that remains is assembling it in the vacuum with the torsion fiber attachments. Since our pendulum will have large numbers of aligned spins in order to be sensitive to spin coupled forces, an essential component to the experiment is demonstrating that its magnetic couplings can be controlled.

To this end, after assembling the ring we tune the magnetizations of each individual segment. This reduces the measured peak to peak magnetic field 70 thousandths of an inch above the rings from 600 G to 30 G. Housing the magnets under two layers of magnetic shielding, as in the experimental design, further reduces the measured magnetic field to $\approx$ 1 mG ((Fig. 2.4-1)). Since we are only interested in torques at 10 times the rotation frequency of the attractor, we can take the fourier transform of these traces to get an idea of the shielding at the science signal. The torque on the pendulum depends on the product of the magnetic fields of the pendulum and attractor, and so we can get a very rough estimate of the shielding factor by comparing $5 \cdot 10^3$ G of spin contrast every $18\,^\circ$ to a magnetic field variation of $4 \cdot 10^{-5}$ G at the same frequency outside the ring. This means we have room to see spin coupled interactions down to 10^{-16} compared to magnetic interactions.

Using these data, we have designed and built a set of magnetic shields which will magnetically isolate the pendulum from the attractor.

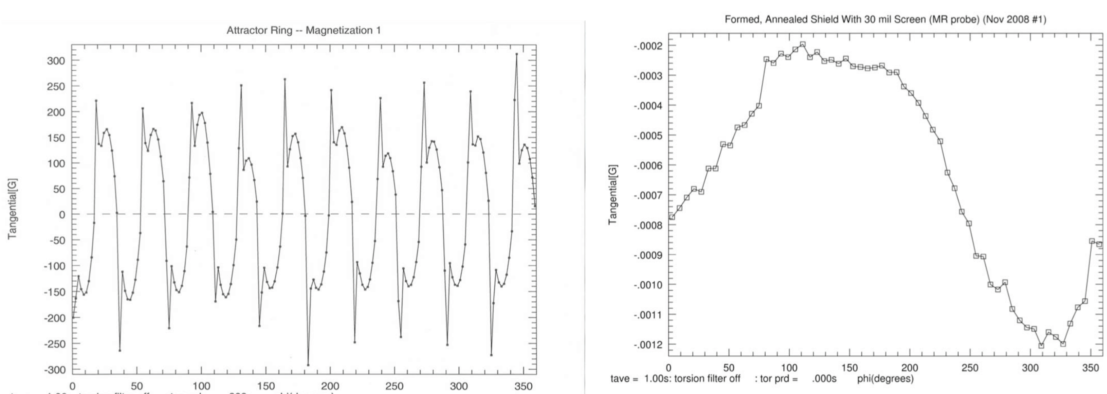

Figure 2.4-1. Left: Before tuning the Alnico magnetization. Right : After tuning and with magnetic shielding

[1]CENPA Annual Report, University of Washington (2007) p. 38

2.5 Designing an equivalence-principle pendulum containing a hydrogen-rich test body

E. G. Adelberger, J. H. Gundlach, B. R. Heckel, S. Schlamminger, and W. A. Terrano

Ordinary luminous matter is believed to be less than one quarter of the total mass of the universe, however these estimates rely on the assumption that the only long-range interaction between Dark and Luminous is gravity. This important assumption can be tested in the lab by looking for an equivalence- principle violating interaction between the Dark Matter in our galaxy and a composition dipole in our pendulum as any non-gravitational interaction is expected to violate the equivalence principle. The sensitivity of an equivalence principle test is proportional to the degree to which the test bodies differ. To date, all equivalence-principle tests have employed test bodies that have varying degrees of neutron excesses. One can gain roughly a factor of 10 in sensitivity by using test bodies of polyethylene (which has a 1 in 7 proton excess) and beryllium (which has a 1 in 9 neutron excess)[1].

We are gearing up for new version of the classic torsion balance tests of the Equivalence Principle with this test-body pair. The major difficulty at this point is working with a plastic material. All of our previous test bodies consisted of metals. We have built the prototype (Fig. 2.5-1) that was proposed earlier[2]. The prototype will allow us to take gravitational data and allow us to evaluate the thermal and mechanical stability of the Ultra High Molecular Weight Polyethylene.

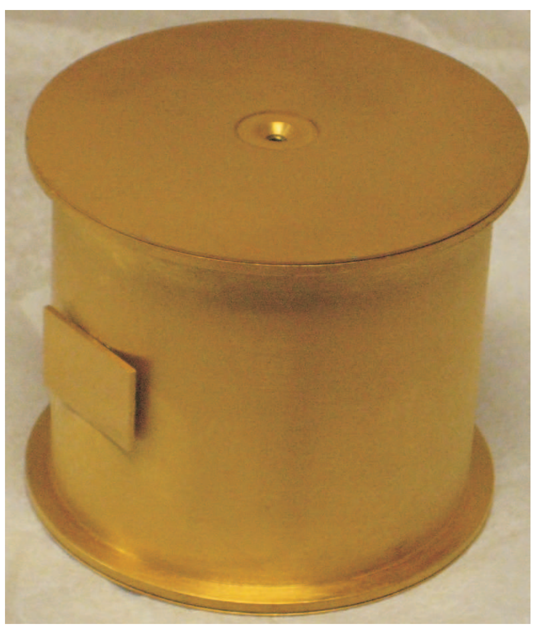

Figure 2.5-1. Photo of completed pendulum

---

[1]E.G. Adelberger, J.H. Gundlach, B.R. Heckel, S. Hoedl, and S. Schlamminger, Prog. Part. Nucl. Phys. 62, 102 (2009)

[2]CENPA Annual Report, University of Washington (2009) p. 31.

2.6 Looking for signatures of space-time granularity with a spin-polarized torsion pendulum

E. G. Adelberger, B. R. Heckel, S. Schlamminger, and W. A. Terrano

Attempts at detecting a fundamental granularity of space-time have often looked for violations of Lorentz symmetry as a signal. Bonder and Sudarsky[1] propose a phenomenological signature of a Lorentz invariant granularity that would manifest itself in the lab as a coupling between (1) the curvature of space due to the earth and local masses, (2) the angular momentum of the earth and (3) the spin of the particle. We are looking for this signal using a spin-polarized pendulum[2] and a large quadrupole source that can be rotated between data taking runs. Rotating the Q22 source by 90° changes the relative orientation of the local curvature and the earth's angular momentum and shifts the lowest energy orientation of the accumulated electron spin in the pendulum. Comparing runs taken with different Q22 configurations allows us to isolate effects due to the proposed signal of Bonder and Sudarsky.

In certain mass distributions used for the Q22 source we saw a non-gravitational systematic effect on the pendulum. By changing the mass distribution of the sources relative to the turntable without changing the Q22 moments, it seems that this systematic is related to objects placed down near the rotating turntable. Presumably the systematic is mediated through thermal gradients between the temperature-stabilized lead and the turntable which is subject to heating due to friction. In order to test this, we have built a mount which will hold a temperature sensor at the location of the Q22 masses, hopefully allowing us to better understand the mechanism by which the mass distribution feeds into the pendulum torque.

[1] Y. Bonder and D. Sudarsky, Class. Quantum Grav. **25**, 105017 (2008).
[2] CENPA Annual Report, University of Washington (2003) p. 11

2.7 A cryogenic torsion balance for tests of the equivalence principle

E. A. Adelberger, M. Bassan*, F. Fleischer, B. R. Heckel, and H. E. Swanson

As described in the previous annual report[1], we have designed and built a cryostat to operate a torsion balance at temperatures near 5 K. The instrument will be used to test the equivalence principle, using the sun or the center of the galaxy as an attractor. As previously reported, the cryostat has been successfully cooled down, and it has been demonstrated that a temperature of $5 - 6$ K can be reached.

Since then, work on the basic parts of the experiment has been completed and a number of tests have been performed to ensure their correct performance. Using commercially available accelerometers, we have tried to quantify the level of vibrational isolation achieved by our passive isolation system. Due to the noise floor of these devices, we could not determine the exact isolation factor. The data, however, indicate that the accelerations on the top flange of the cryostat are smaller by at least by a factor of 500 than measured on top of the cold head of the pulse tube cooler.

Furthermore, a moment-free test pendulum has been built to evaluate the noise performance of the torsion balance at room temperature and at cryogenic temperatures. Using this pendulum, first test data have been recorded. Additionally, the whole setup has been shown to work at low temperature. During these test runs a few problems have been identified and work on fixing these issues is in progress. As an example, improvements to the optical readout system are being made to remove the excess noise introduced by instabilities of the laser beam. Fig. 2.7-1 shows the apparatus with the vacuum chamber and the thermal shields removed.

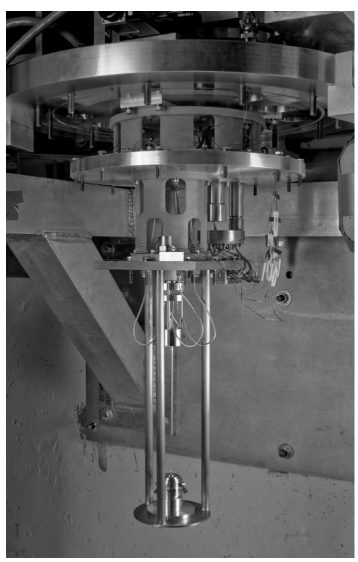

Figure 2.7-1. The inside of the cryostat (thermal shields removed) with the test pendulum.

*Università di Roma Tor Vergata, Rome, Italy.

[1]CENPA Annual Report, University of Washington (2009) p. 28.

2.8 Observation of Lévy walks in torsion balance squeeze film damping

J. H. Gundlach, C. A. Hagedorn, and S. Schlamminger

Torque noise due to the fluctuating impacts of residual gas particles can limit the sensitivity of our torsion balances and also gravitational wave interferometers[1]. The noise, and its related damping, are expected to be significantly enhanced when the gas flow is constrained by restrictive geometry. This enhancement is known as "squeeze film damping[2]" (SFD). We used both the parallel-plate inverse-square-law experiment (see Sec. 2.2) and the LISA prototype experiment (see Sec. 2.10) to measure this distance-dependent effect.

In both experiments, the flat torsion-pendulum plate and a nearby flat surface were arranged to make a rectangular area of close proximity (Area 12 or 40 cm^2, distance 0.1-9 mm). The free-decay quality factor of torsional oscillation was measured as a function of pendulum-surface separation. We found that the traditional Gaussian calculations of the strength of SFD were incorrect. We made Monte Carlo simulations of particle paths within the gaps and found that the diffusion time for particles to move in and out exhibited scale-invariance. We identified the paths as Lévy walks. The damping of both torsional oscillators scaled with the gap size d as $d^{-\gamma}$, with $1 < \gamma < 2$, indicative of fractal behavior. Our parameter-free simulation matched the data from both experiments well. These results have had immediate impact on the design of modern gravitational wave detectors.

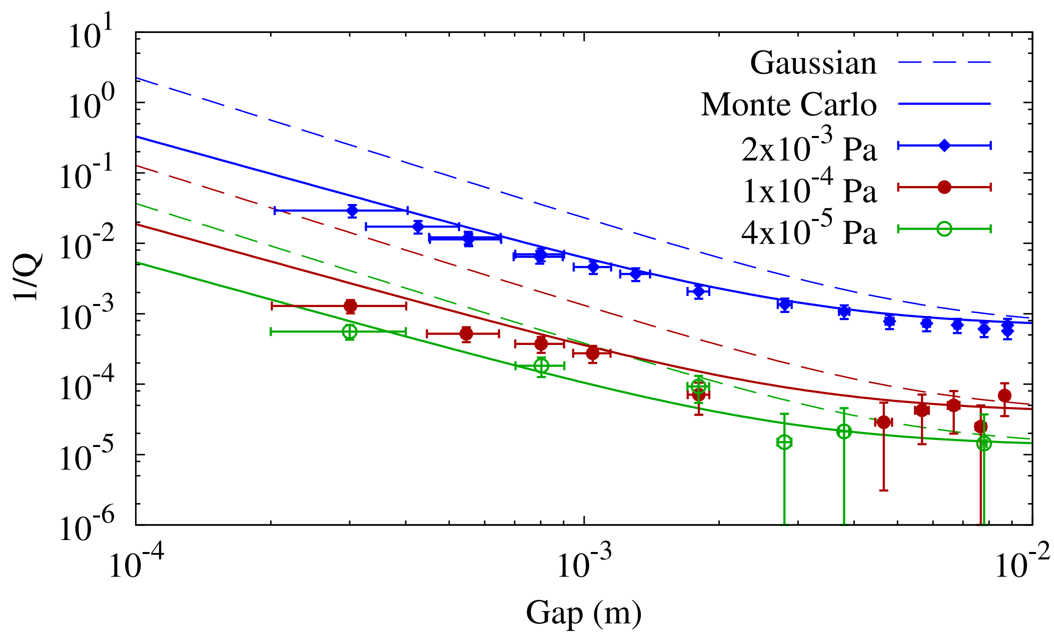

Figure 2.8-1. The measured loss in the LISA torsion balance as a function of surface-pendulum separation. Data were taken at three different pressures. The solid lines are generated using the Monte Carlo-simulated diffusion time. The dashed lines are generated using Gaussian diffusion. Measured residual gas speciation at each pressure were taken into account.

[1]A. Cavalleri et. al. Phys. Rev. Lett. 103, 140601 (2009)

[2]M.A.G. Suijlen et al., Sens. Actuators A 156, 171 (2009).

2.9 Development of a high-precision interferometric quasi-autocollimator

J. H. Gundlach, C. A. Hagedorn, S. Schlamminger, and M. D. Turner

We are currently developing a high-precision angle readout instrument with target angular sensitivity of less than 1 picoradian at 1 Hz. This has potential use in any of our group's torsion balance experiments. It uses the quantum weak value amplification effect[1] and is based on the setup described by Dixon, *et al.*[2]. As shown in Fig. 2.9-1(a), the device is based around a Sagnac interferometer, with additional optical components added to increase the device's utility.

In Sagnac interferometers, the port through which the light enters is referred to as the light port, and the other is the dark port. The weak value amplification effect used by this device results in a deflection of the beam spot at the dark port, which is much bigger than the deflection that would occur without the beamsplitter. The amplification factor is inversely proportional to the path-length difference for the two paths in the interferometer, which can be adjusted with a piezo actuator on one of the mirrors. Manipulation of the polarization by quarter waveplates allows for the light exiting the light port to be monitored, allowing deflection due to mirror movement to be subtracted from the measurement at the dark port.

For the data shown in Fig. 2.9-1(b), linear photodiodes were used as the position sensitive detectors (PSDs); a piezo-actuated mirror, with a 10-nrad, 2-Hz sine-wave injected signal, was used in place of a pendulum; and the quarter waveplates were not in place. An amplification factor (visible as a system noise reduction) of approximately two orders of magnitude is shown. We are currently working on developing an alternate geometry that more closely resembles an autocollimator, which would make the device insensitive to pendulum swing.

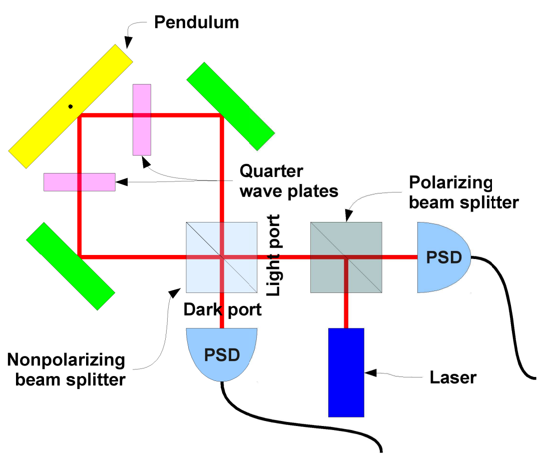

(a)

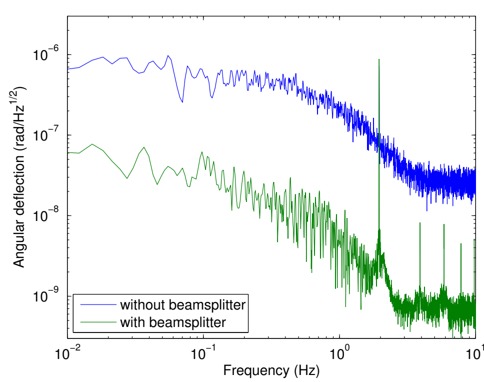

(b)

Figure 2.9-1. (a) A diagram of the device. (b) Data collected with and without the nonpolarizing beam splitter in place. Since the data are scaled to the injected signal, the weak value amplification appears as a reduction in the system noise.

[1]Y. Aharonov, D.Z. Albert, and L. Vaidman, Phys. Rev. Lett. **60**, 1351 (1988).
[2]P. B. Dixon, D. J. Starling, A. N. Jordan, and J. C. Howell, Phys. Rev. Lett. **102**, 173601 (2009).

2.10 UV charge management for gravitational wave observatories

J. H. Gundlach, C. A. Hagedorn, S. Schlamminger, and M. D. Turner

The effect of charge accumulation on the test masses in future gravitational wave interferometers such as Advanced LIGO and LISA is poorly understood. Charges can accumulate on a test mass due to cosmic rays or triboelectric processes. Triboelectric charge transfer can occur, for example, when the test mass hits a nearby surface during an earthquake. Once a test mass has acquired electric charge, spurious forces between the charged test mass and nearby surfaces can degrade the sensitivity of the interferometer. A mechanism to discharge the test mass is required to restore the performance of the instrument after a charging event.

We have built a torsion balance to investigate forces between an electrically insulated test mass and a grounded plate, shown in Fig. 2.10-3. A silicon pendulum is suspended from a quartz fiber, which has a measured resistance of $R = 10^{19}\ \Omega$. Two copper plates are placed in the vicinity of the pendulum and the gap between the plates and pendulum can be varied from 0.1 mm to 9 mm. The angular excursion of the pendulum is measured by an autocollimator and processed by a digital feedback loop into a control voltage that is applied to either of two control electrodes to hold the pendulum parallel to the copper plates. In order to avoid large contact potentials all surfaces have been gold plated. The charge on the torsion pendulum can be measured with a procedure outlined in last year's annual report[1]. In the past year, we have used our torsion balance to study charge control using UV light.

Two devices are used to control the charge on the pendulum: (1) A UV LED shines light with 244 nm wavelength directly on the pendulum. The photon energy of 5.1 eV is enough to liberate electrons from the gold surface with a typical work function of 5 eV, by the photoelectric effect. (2) To add negative charge carriers to the pendulum, an electron gun is used. A cross sectional drawing of the electron gun is shown in Fig. 2.10-2. UV light is used to create photo-electrons from a magnesium coated cathode. The electrons are accelerated by an electric potential of 6 V between the photo-cathode and the copper anode. The electrons keep their momentum in the field free region of the copper anode and exit the electron gun towards the pendulum. To avoid charging the pendulum positively by light leakage, the wavelength of the light source was chosen such that the photon energy 3.8 eV is below the work function of gold.

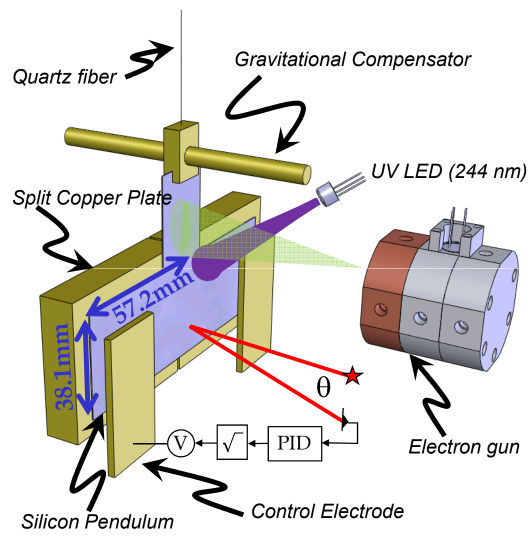

Figure 2.10-1. Schematic drawing of the torsion balance and the two devices for charge control: a UV LED and an electron gun. Electric charge on the pendulum couples to the copper plate behind the pendulum and creates a measurable torque on the pendulum. The distance between the plate and the pendulum can be adjusted between 0.1 to 9 mm.

[1]CENPA Annual Report, University of Washington (2009) p. 24.

With the UV LED and the electron gun complete charge control is achieved. Fig. 2.10-3 shows the charge on the pendulum as a function of time. The pendulum can be charged negatively and positively with a charging rate of about 10^{-14} C/s. This is sufficient to control the charge on the test mirrors for planned gravitational wave interferometers.

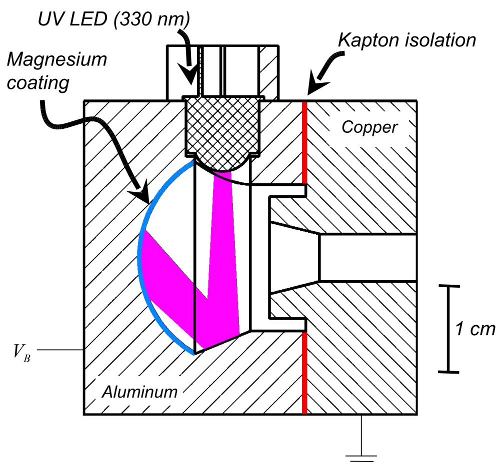

Figure 2.10-2. A cross-sectional drawing of the electron gun.

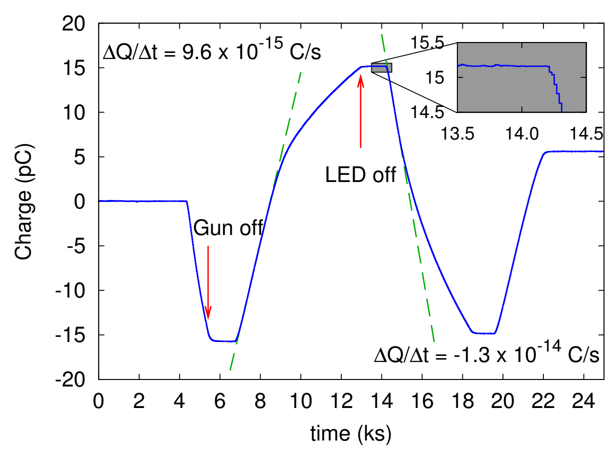

Figure 2.10-3. The charge on the pendulum can be controlled in both directions.

Weak Interactions

2.11 Laser trap developments for ^{6}He

A. García, A. Knecht, Z.- T. Lu*, P. Mueller*, A. S. C. Palmer, W. Williams*,
C. Wrede, and D. W. Zumwalt

Developments to put together a Magneto-Optical Trap (MOT) have been performed at Argonne National Lab. Although a similar trap had been used there before to determine the charge radii of ^{6}He and ^{8}He, several parts needed to be re-assembled. In addition, modifications were made to improve its efficiency.

To optically trap neutral helium, the atom must be prepared in a state with a net magnetic moment. Additionally, it must have an atomic cycling transition of sufficiently low energy to be accessed by currently available laser systems. The ground state of helium satisfies neither condition since it is nearly 20 eV below the first excited state (corresponding to a 62 nm wavelength) and thus the helium must be prepared in the 2^3S_1 metastable state. The lifetime of the metastable state is much longer than the lifetime of ^{6}He, so it will not interfere with trapping. To achieve this state, the helium is first mixed with krypton and xenon gas at low pressure (a few mTorr) inside an RF-coupled discharge tube. We use krypton and xenon due to their convenient chemical properties and relatively low ionization energies which make for a stronger discharge. Several Watts of RF power ionize the gas creating electron collisions which populate many atomic states. Some small fraction (10^{-5}) of these atoms are left in the metastable state.

Because most of the gas exiting the discharge tube is not metastable helium, we must select out and collimate the metastable gas. This is accomplished using transverse cooling consisting of two pairs of long mirrors which run parallel to the atomic beam (two vertical and two horizontal). Lasers with $\lambda = 1083$ nm are then introduced transverse to the atomic beam and are bounced back and forth hundreds of times by the mirrors. Because only the metastable helium has a cycling transition sensitive to 1083 nm light, it is the only population which is collimated. The rest of the gas is pumped out by a 250 L/s turbopump.

When the gas exits the discharge tube, it is traveling at nearly 1000 m/s. The magneto-optical trap requires the helium to be entering at around 10 m/s, and thus the gas must be cooled before it enters the trapping chamber. This is accomplished using a 1.8 m long Zeeman slower (see Figure 2.11-1), which is a solenoid with an axially-dependent magnetic field achieved by tapering the number of coils along the length of the slower. A 1083 nm circularly-polarized laser counter-propagates along the atomic beam axis opposite to the direction of the atoms. The purpose of the slower is to introduce a Zeeman shift in the atomic levels of the atoms to account for the changing Doppler shift caused by the atoms slowing down in the presence of the laser. The laser is circularly-polarized to couple to a particular change in the magnetic quantum number according to the direction of the surrounding magnetic field.

Once the gas is sufficiently slow, it can be trapped. Two coils in an anti-Helmholtz

*Physics Division, Argonne National Laboratory, Argonne, IL

configuration in a chamber introduce a quadrupole magnetic field with zero field in the center, linearly increasing in magnitude outward. Six counter-propagating 1083 nm laser beams shine onto the atoms in three orthogonal directions. For each pair of beams, each laser has a counterpart with opposite circular polarization. The laser beams Doppler cool the atoms while the magnetic field introduces a potential gradient with a minimum in the center of the trap. In this way, we have trapped millions of ^{4}He atoms with a cloud size about 1 mm in diameter. A 150 L/s turbopump removes any background gas in the trap chamber to minimize loss mechanisms.

We were able to achieve trap efficiencies of 10^{-7}. With further tuning and modification, we believe we will reach our trap efficiency goal of 10^{-5}. We will make a two-dimensional MOT to focus the atomic beam before entering the Zeeman slower, which should increase our efficiency by a factor of 2. We will also use more laser power (from 0.5 W to 4 W) which should yield another factor of 3.5. Because most of the gas doesn't go into the metastable state, we plan to use the 250 L/s turbopump to recirculate the remaining gas through the RF-discharge before it all decays, which should yield a factor of 5 increase in efficiency. With these modifications, we expect to be able to reach our trapping goals. If the proof-of-production runs scheduled until the beginning of summer go as expected, the trap apparatus will be moved from Argonne to CENPA. We estimate that this could happen before the end of the summer.

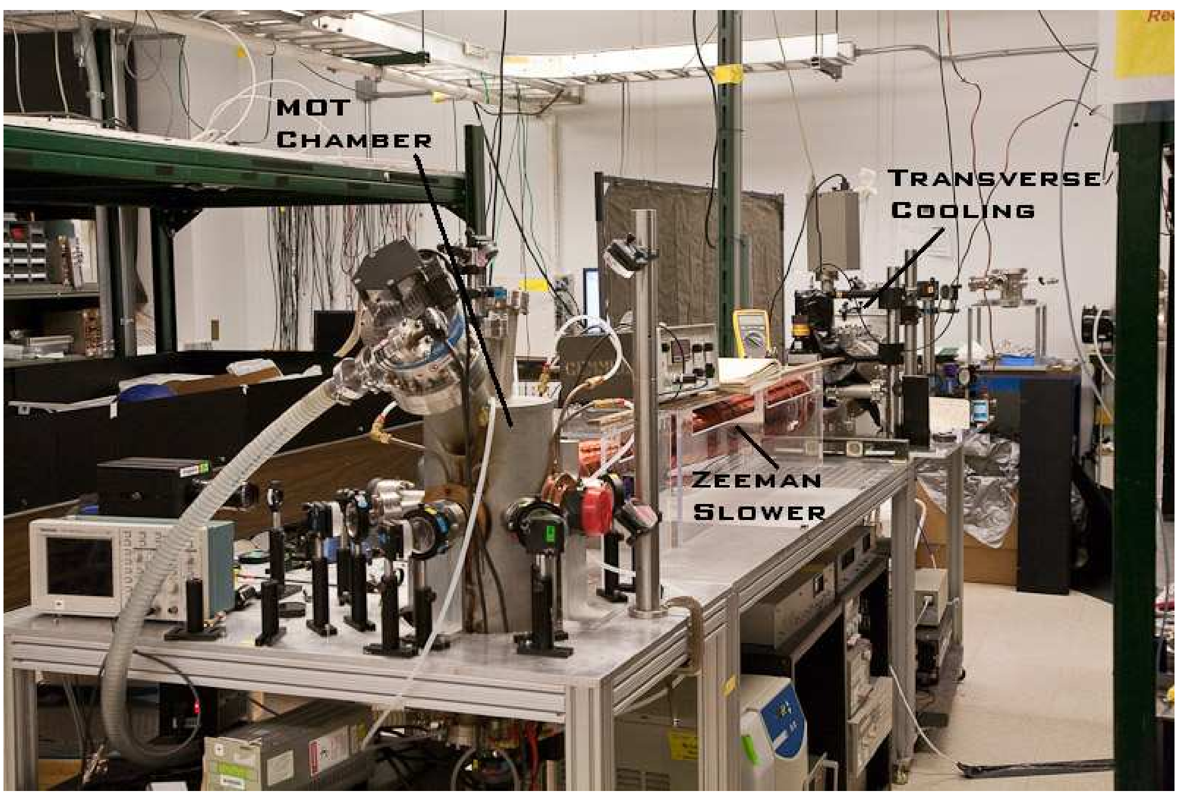

Figure 2.11-1. Laser trapping setup with MOT chamber in foreground

2.12 Production of ^{6}He at CENPA

A. García, G. C. Harper, A. Knecht, Z. T. Lu[*], P. Müller[*], A. S. C. Palmer,
R. G. H. Robertson, D. I. Will, W. Williams[*], C. Wrede, and D. W. Zumwalt

During summer 2009, we assembled the target for the production of ^{6}He using the ^{7}Li(d,^{3}He)^{6}He reaction on molten Li outlined in last year's annual report[1]. Fig. 2.12-1 shows the assembled target. The lithium was purchased as 12.5 mm thick bars sealed under mineral oil. Due to the high reactivity of the lithium, a 2 cm long piece was cut from the bar and transferred into the target cell under an argon atmosphere inside a glove box.

Figure 2.12-1. Left: Principle of the apparatus for the production of the molten lithium target. Middle: Target insert holding the lithium. Also visible is the white ring made of ceramic to electrically insulate the target from the rest of the beam line. Right: Final setup of the target to be mounted onto the beam line critically eyed by D. Zumwalt and A. Palmer.

The first tests were conducted in September 2009 with 12 MeV deuterons and a beam current of 10 nA. The ^{6}He produced was guided away from the target in an approximately 1 m long tube including a 90 degree bend. The end of the tube featured a 0.25 mm thick copper window. Right next to that, we had mounted a 5 mm thick scintillator detecting the decay electrons. The scintillator was shielded from the direct line of sight to the molten lithium in order to count only decay electrons from ^{6}He atoms liberated from the lithium. After having the beam on the target for 8 s, we switched the beam off for 8 s and counted typically 300 decays during that time. This amount N is related to the ^{6}He incoming rate R as $N \approx \eta R \tau$ with η the efficiency of detecting betas and τ the lifetime of the ^{6}He atoms of 1.16 s. We have calculated the efficiency using a simulation to be $\sim$0.005. We conclude therefore, that the production rate amounts to $R \approx 5 \times 10^{4}$ atoms/s.

Several improvements will be implemented in the coming year in order to reach the targeted production rate of 10^{9} atoms/s: (1) beam current of 20 μA, (2) deuteron energy of 15 MeV, and (3) stirring of the molten lithium in order to reduce contamination on the surface and thus improving the efficiency of the extraction of ^{6}He atoms from the molten lithium. In addition, we will set up a transfer beam line to a low background area where the laser system for the trapping of the ^{6}He atoms will be installed.

---

[*]Physics Division, Argonne National Laboratory, Argonne, IL

[1]CENPA Annual Report, University of Washington (2009) p. 32.

2.13 Permanent electric dipole moment of atomic mercury

B. R. Heckel, E. N. Fortson, B. Graner, and T. Loftus

Atomic EDM experiments offer perhaps the most sensitive probe of CP violation in theories of physics beyond the Standard Model, and our measurements of the ^{199}Hg EDM over the years have achieved the most precise EDM limit on any system. The leading theoretical extension to the Standard Model, supersymmetry (SUSY), is expected to generate a ^{199}Hg EDM comparable to our experimental limit. By increasing the precision of our result, we can provide important information about the model parameter space of SUSY and other theories.

We recently published a new upper limit[1] for the EDM of ^{199}Hg: $|d(^{199}\text{Hg})| < 3.1\times 10^{-29} e\,\text{cm}$ (95% confidence level), a seven-fold improvement in the upper limit over previous work. The experiment uses a frequency-quadrupled laser diode on the 254 nm mercury absorption line to orient the ^{199}Hg nuclear spins, and to measure their Larmor frequency.

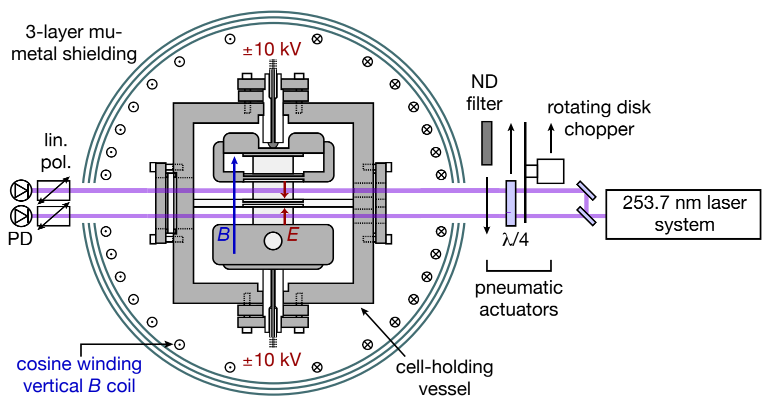

Figure 2.13-1. Simplified diagram of the ^{199}Hg EDM apparatus showing details of the vapor cell holding vessel and middle cell light beams. High voltage ($\pm$ 10 kV) is applied to the middle two cells with the ground plane in the center, so that the electric field is opposite in the two cells. The outer two cells are enclosed in the HV electrodes (with light access holes as shown here for the bottommost cell), and are at zero electric field. A uniform magnetic field is applied in the vertical direction.

In the past year, we have completed a detailed review paper that describes our recent results. We have embarked on an upgrade to the apparatus that allows us to measure both polarization states of the light that it transmitted through the vapor cells. Measuring both polarizations doubles our signal amplitudes and allows us to remove the noise to our frequency measurements due to laser intensity fluctuations. We have also measured a linear Stark interference effect on the 254 nm transition we use to optically pump and probe the spin precession of ^{199}Hg. The effect can lead to a fractional change in the absorptivity that is linear in a static electric field. The measured interference amplitude, $a_{SI} = (a_{M1} + a_{E2}) = (5.8\pm1.5)\times10^{-9}\ (kV/cm)^{-1}$, agrees with relativistic, many-body predictions and thus resolves a 10× discrepancy between these calculations and earlier central-field estimates. This study validates the capability of the ^{199}Hg EDM search apparatus to resolve non-trivial, controlled, and sub-0.1 ppb Larmor frequency shifts with EDM-like characteristics.

[1] W. C. Griffith, *et al.*, Phys. Rev. Lett. **102**, 101601 (2009).

2.14 Progress in determining the beta asymmetry from neutron decay

A. García and C. Wrede for the UCNA collaboration

The UCNA collaboration is working toward a precise determination of the beta asymmetry from polarized neutrons using ultra-cold neutrons that are produced at the Los Alamos Neutron Science Center (LANSCE). The motivation is to determine the ratio of the axial to vector coupling constants, g_A/g_V with precision better than 1%. This can be used in combination with the neutron halflife to extract $V_{\rm ud}$, the up-down element of the quark weak mixing matrix. Alternatively it can be used in conjunction with the precise measurements of $V_{\rm ud}$ from $0^+ \rightarrow 0^+$ nuclear beta decays to extract the neutron halflife. These three quantities, the $V_{\rm ud}$ from $0^+ \rightarrow 0^+$ nuclear decays, the neutron halflife, and g_A/g_V can be considered as three basic elements of the Standard Model that should fit together. Presently there are significant discrepancies[1].

Last year we published the first measurement of the beta asymmetry from ultra-cold neutrons[2] which determined the asymmetry to approximately 5%. During the last year the collaboration continued to take data which has statistical uncertainty below 1%. The analysis should be finished before the end of the summer of 2010.

2.15 Progress in analysis of emiT data

A. García for the emiT collaboration

The emiT collaboration worked on an experiment to search for the breaking of the time-reversal symmerty in neutron beta decay[3]. The experiment has already been performed and data analysis is proceeding using a 'blinding' method that allows tracking of possible systematic errors without biasing the result. During the past year we have worked on finishing open issues which required several MonteCarlo calculations for which the UW was responsible. The collaboration is considering 'opening the box' and publishing the results during the summer of 2010.

[1] C. Amsler et al. (Particle Data Group), Physics Letters **B667**, 1 (2008) and 2009 partial update for the 2010 edition.

[2] R. W. Pattie, Jr. et al. (UCNA Collaboration), Phys. Rev. Lett. **102**, 012301 (2009).

[3] See Mumm et al, Rev. Sci. Instr. **75** , 5343 (2004) for a description of the apparatus.

2.16 Parity non-conserving neutron spin rotation experiment

C. Bass*, K. Gan†, B.R. Heckel, D. Luo‡, D. Markoff§, A. M. Micherdzinska†, H.P. Mumm*, J. Nico*, A. Opper†, W.M. Snow‡, and H.E. Swanson

The apparatus and motivation for the parity non-conserving (PNC) neutron spin rotation experiment are described in previous CENPA annual reports[1]. The experiment was completed in June 2006, and ran for a total of 3 reactor cycles or about 106 calendar days. The observable is the spin rotation angle ϕ_{PNC}. Turning off a spin precessing field allows us to make a null measurement which we refer to as ϕ_{NULL}. This data is taken concurrently with the PNC data and analyzed in the same manner.

We have completed data analysis and estimates of possible systematic effects. In analyzing the data a filter was used to remove spurious effects from time varying background magnetic fields. The filter was validated using data taken at the end of the run series with cold ^{4}He gas instead of a liquid as the target medium which produces no PNC spin rotation. The slow warmup of the apparatus caused a monotonic drift in the ambient magnetic field. These data were analyzed with and without the filter for the PNC and $NULL$ spin rotation angles. The results are shown in Table 2.16-1.

Analysis	ϕ_{PNC}	ϕ_{NULL}
No Filter	$18.2 \pm 6.6 \times 10^{-7}$	$-26.5 \pm 5.6 \times 10^{-7}$
Filter	$1.0 \pm 5.4 \times 10^{-7}$	$-0.48 \pm 4.3 \times 10^{-7}$

Table 2.16-1. Effect of applying the filter to a data set taken with ^4He gas (no liquid) and a time varying background magnetic field

The PNC spin rotation results from all three reactor cycles are shown in Fig. 2.16-1. The null data are included to show both sets of points come from similar distributions. Each data point corresponds to about 8 hours of running. The mean and one sigma error of these data is

$$\phi_{PNC} = 0.9 \pm 3.7 \times 10^{-7} radians. \tag{1}$$

The largest source of systematic uncertainty is the residual longitudinal magnetic field which precesses the neutron spin by about 4 orders of magnitude more than the predicted PNC angle. Estimates come from calculations of the dependence of neutron trajectories on properties of the target and from exaggerating the various sources and scaling the measured results to nominal run values. We considered in these calculations the optical potential and diamagnetism in liquid Helium, small angle scattering, multiple scattering, target reflections

*NIST Center for Neutron Research, 100 Bureau Drive, Stop 8461, Gaithersburg, MD 20899-8461
†The George Washington University, Department of Physics, Corcoran 105, 725 21st St, NW, Washington, DC 47408
‡Department of Physics, Indiana University Cyclotron facility, 2401 Milo B Sampson Land, Bloomington, IN 47408
§North Carolina State University, TUNL, Raleigh, NC 27695

[1]CENPA Annual Reports, University of Washington (2003) p. 5, (2009) p. 37.

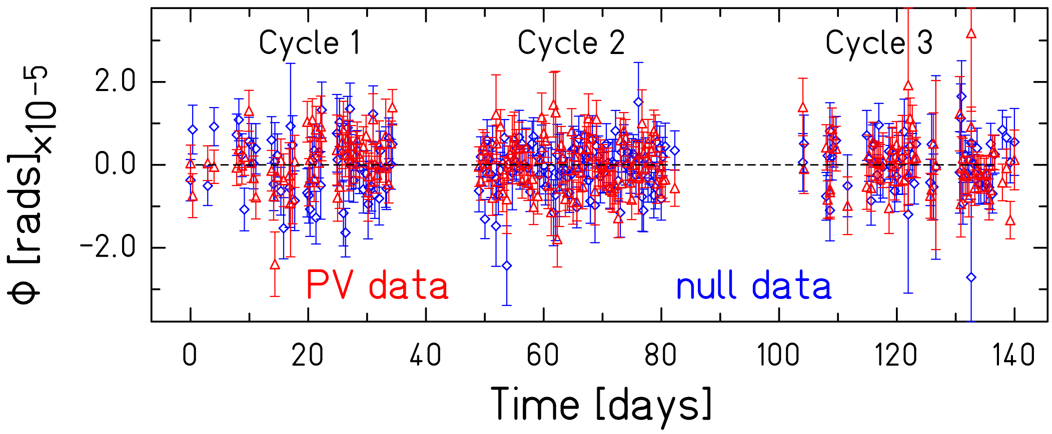

Figure 2.16-1. Experimental data from all reactor cycles. Both the PNC (labeled PV data in red) and $NULL$ data points (blue) are included to show they both come from similar distributions.

and refraction, and non-uniformity in the analyzing power across the target. The total of these calculated systematic effects is $\sim 4 \times 10^{-8}$. Upper limits from measurements are given in Table 2.16-2.

Systematic sources	ϕ_{PNC}
B-Field	$\leq 4 \times 10^{-8} rad/m$
B-Field gradient	$\leq 3 \times 10^{-8} rad/m$
Polarizer-Analyzer misalignment	$\leq 6 \times 10^{-8} rad/m$

Table 2.16-2. Measured limits on potential systematic effects. The sources are greatly exaggerated and the PNC angles are scaled to typical run values.

The effective length of the target is about 0.41 meters. Scaling our result for comparison with predictions gives

$$\frac{d\phi_{PNC}}{dz} = +1.7 \pm 9.1(stat) \pm 1.3(sys) \times 10^{-7} rad/m. \tag{2}$$

The $NULL$ measurement is also zero within comparable errors.

$$\frac{d\phi_{NULL}}{dz} = -1.2 \pm 10.0 \times 10^{-7} rad/m \tag{3}$$

2.17 M1 width of the 2_1^+ state in ^{22}Na and searches for tensor contributions to beta decays.

E. G. Adelberger, G. C. Ball[*], M. K. Djongolov[*], A. García, G. Hackman[*], G. C. Harper, D. A. Short, S. P. R. Steininger, C. E. Svensson[†], S. Triambak[*], P. A. Vetter[‡], D. M. Williams, and C. Wrede

A determination of the $\beta - \gamma$ angular correlation from ^{22}Na beta decay with the GAMMASPHERE array[1] has been used to extract induced-tensor-currents contributions to the weak interaction. The result, together with other available experimental data yielded an unexpectedly large induced tensor (second class) component to the hadronic current, which is at variance with the Standard Model. A weak link in the data used for this analysis is another recoil-order term, the weak magnetism form factor, which is extracted from an independent unpublished[2] determination of the analog isovector magnetic dipole ($2^+ \rightarrow 3^+$) gamma-ray transition strength in ^{22}Na. The state of interest in ^{22}Na at $E_x = 1952$ keV was produced using a ^{25}Mg$(p, \alpha\gamma)$ reaction. The result had low statistics and relatively significant backgrounds. We are currently setting up an experiment to measure the Γ_{M1} value from $E_x = 1952$ keV state using a well known ^{21}Ne(p, γ) resonance at $E_p = 1112$ keV. This resonance leads to a gamma cascade in ^{22}Na at $E_x = 7800 \rightarrow 1952 \rightarrow 0$ keV. We will use a γ–γ coincidence setup with a 120% HPGe detector and a large $10'' \times 10''$ NaI detector. This method will provide both high detection efficiency and reduced backgrounds.

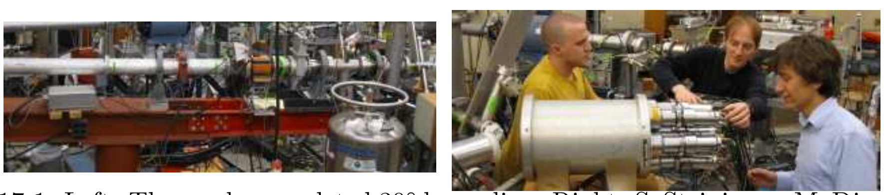

Figure 2.17-1. Left: The newly completed 30° beam line. Right: S. Steininger, M. Djongolov and D. Williams setting up the detectors for testing.

For this experiment we have dismantled the 30° left beam line in cave 1 and constructed a new one in its place. We installed two sets of steerers, rastering coils, two gate valves, a beam profile monitor and a collimated target chamber with electron suppression. The vacuum in the downstream part of the beam line is maintained at $\approx\ 2 \times 10^{-7}$ torr using one turbo pump and a LN_2 filled cold trap. We have performed a feasibility test of the coincidence method using a low-intensity proton beam at ≈ 1.0 MeV on a thick aluminium target to produce ~ 11 MeV gamma-rays in coincidence with ~ 1.7 MeV gammas analogous to the planned experiment. We found good beam transmission and the coincidence setup to work satisfactorily. We are now planning a test run using an implanted ^{21}Ne target and a high current proton beam. Target development for this purpose is currently underway.

[†]Department of Physics, University of Guelph, Guelph, Ontario, N1G 2W1, Canada
[*]TRIUMF, 4004 Wesbrook Mall, Vancouver, British Columbia V6T 2A3, Canada
[‡]Lawrence Berkeley National Laboratory, Berkeley, CA 94720
[1]C. J. Bowers *et al.*, Phys. Rev. C **59**, 1113 (1999).
[2]R. B. Firestone *et al.*, Lawrence Berkeley Laboratory Report No. LBL-12219, (unpublished).

3 Axion Searches

3.1 ADMX axion search

M. Hotz, D. Lyapustin, L. J. Rosenberg, G. Rybka, A. Wagner, and D. I. Will

The Axion Dark Matter eXperiment (ADMX) is a large-scale RF-cavity search for galactic dark-matter axions. This experiment has been in operation since the mid-1990s, and has recently completed the "Phase I" upgrade and data-taking run. The goal of this upgrade was to significantly improve the experiment sensitivity by replacing the key technology in the experiment, cryogenic microwave amplifiers, with Superconducting Quantum Interference Device (SQUID) amplifiers. This upgrade was successful and the first-year data set has been published. The experiment is in the process of moving to CENPA from Lawrence Livermore Lab, and will simultaneously be upgraded again to further increase the sensitivity. This "Phase II" upgrade, sited at CENPA, will be a "definitive" experiment: it will have sufficient sensitivity to either detect axions or rule out the QCD-axion hypothesis at high confidence.

The axion was postulated three decades ago to explain why QCD conserves the discrete symmetries P (parity) and CP (charge conjugation times parity). QCD's predictions depend upon a parameter θ. When θ differs from zero, QCD violates P and CP. Since the strong interactions appear P- and CP-symmetric in the laboratory, θ must be very small. The upper limit on the neutron electric dipole moment requires $|\theta| < 10^{-10}$. In the Standard Model, however, P- and CP-violation by the weak interactions feeds into the strong interactions so that the expected value of θ is of order unity. The inability of the Standard Model to account for P- and CP-conservation by the strong interactions is called the "strong CP problem". Peccei and Quinn proposed a solution to this problem in which the Standard Model is modified whereby θ becomes a dynamical field and relaxes to zero. The theory's underlying broken continuous symmetry results in the existence of a new particle, called the axion. The axion is the quantum of oscillation of the θ field and has zero spin, zero electric charge, and negative intrinsic parity. So, like the neutral pion, the axion can decay into two photons.

Despite the prodigious local density of dark-matter axions (in the neighborhood of 10^{14}/cc), however, the expected electromagnetic signal would be extraordinarily weak, around 10^{-23} Watts in the ADMX apparatus. Our present ADMX Collaboration (with original core institutions Washington, LLNL, Florida, NRAO and Berkeley) constructed and operated a large-scale dark matter axion experiment that, for the first time, reached sensitivity to plausible dark-matter axions. This experiment consists of a large microwave cavity immersed in a static magnetic field. Nearby galactic halo axions scatter off the static field and convert into microwave photons within the cavity. The present ADMX experiment, fitted with SQUID amplifiers in the Phase I upgrade, has just completed a scan of the $1.9 - 3.5$ μeV axion mass range. The ADMX detection apparatus is essentially an extraordinarily low-noise radio receiver with a RF cavity forming a tuned tank circuit. A short electric-field probe couples power from the cavity into a cryogenic amplifier, which is cooled to near the cavity temperature, (around 2 K for the original ADMX and Phase I upgrade).

The motivation for lowering the system noise temperature is clear: (i) for a given axion-photon coupling, the scan rate grows as the square of the system temperature, and (ii) for a given scan rate, the power sensitivity which can be reached increases linearly at the system temperature. In ADMX the system noise temperature is essentially the noise temperature of the amplifier plus the cavity physical temperature. We developed SQUID amplifiers in the 100-1000 MHz range specifically for ADMX and this development allowed more than an order-of-magnitude reduction in system noise temperature. We have retrofitted these SQUIDs (but not yet a dilution refrigerator) to ADMX for the Phase I upgrade and recently published first results.

The apparatus within the insert's LHe reservoir is shown in Fig. 3.1-1. The annular space at the center of the reservoir is the location of the SQUID amplifier. This SQUID system consists of, inside to outside, the SQUID itself in its connectorized packaging, superconducting magnetic shields, Cryoperm magnetic shields, an iron shield and the superconducting bucking-coil system. Also shown is the pumped LHe "1K pot" and plumbing that cools the cavity and SQUID.

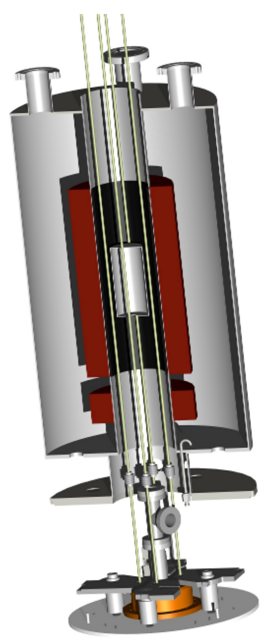

Figure 3.1-1. Sketch of the Phase I apparatus above the cavity. Approximately at the center of this reservoir is the area containing the SQUID amplifier. The bucking-coil and force-compensation coil are shown in red. As the bottom is the 1 K pot attached to the cavity top plate.

Commissioning of the Phase I experiment began in 2007, and the first LHe cool-down was on September 20, 2007. In January 2008, in-situ SQUID amplification was demonstrated, where a weak test-signal injected into a weakly-coupled cavity port was tracked through the full receiver chain. Shortly thereafter, field cancellation using the bucking coil was confirmed to over 7 Tesla in the main coil. By the summer of 2008, operation of each component of the new Phase I system had been demonstrated and science data-taking began.

As of April 2010, the Phase I upgrade has scanned the previously unexplored axion mass region of 812-890 MHz at the "KSVZ" level of sensitivity (one of two benchmark axion models). All technical goals are met and we have characterized the RF and cryogenic systems. The first results from this experiment (see Fig. 3.1-2) were published in a Physical Review Letter, where we have reported results from the medium-resolution data channel at KSVZ sensitivity. This publication[1] marks the last major milestone of the Phase I program.

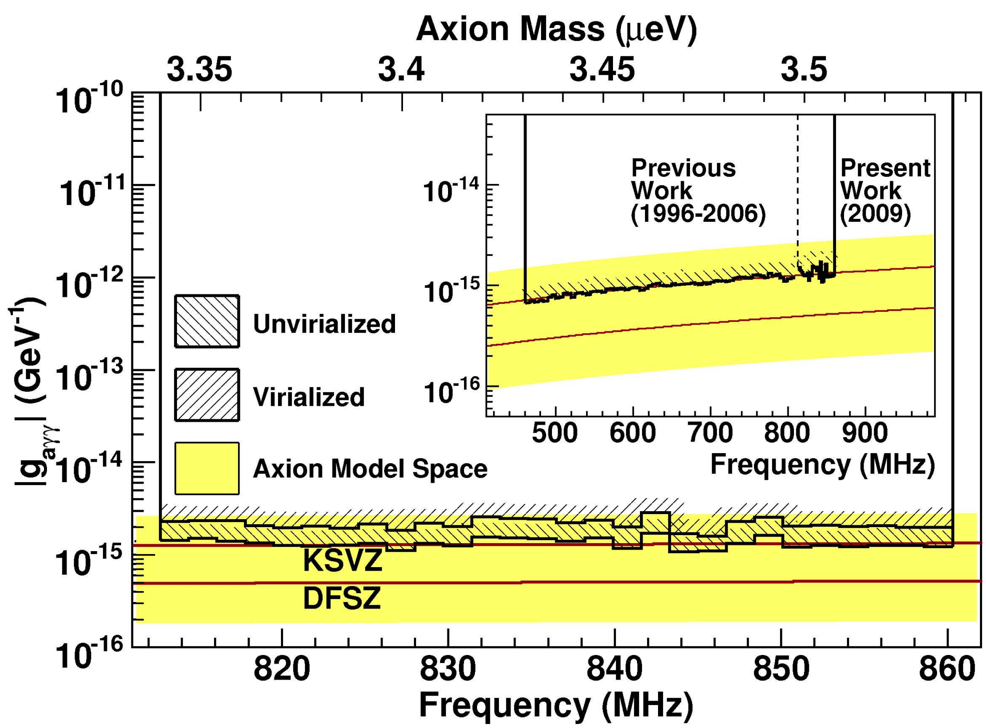

Figure 3.1-2. Axion mass and coupling limits from Phase I upgrade.

Since ADMX is the most sensitive microwave receiver in the world, it is ideal to search for weakly-coupled beyond-standard-model particles besides axions. One such study is a search for scalar chameleons. Chameleons are nonlinearly self-coupled particles whose mass depends on the local density of matter . They are conjectured to play a role in the dark energy of our universe, but their unusual properties evade detection by the short-range gravity experiments traditionally used to search for new light scalars. A different approach is to search for photon-chameleon-photon mixing using the "afterglow" effect, so-called because the slow decay of chameleons after their production by photons may cause a residual "glow" of photons after a source is removed. The GammeV experiment at FNAL used the absence of "afterglow" in their apparatus to exclude a limited region of chameleon-photon coupling parameter space for a range of masses.

The ADMX experiment was run for one day in a configuration to search for chameleon

[1] S.J. Asztalos *et al.*, , Phys. Rev. Lett. **104**, 041301 (2010).

scalars. In this experiment, an RF source was used to excite the TE_{010} mode of the ADMX RF cavity for a period of 10 minutes. During this period, photons in the electromagnetic cavity mode would have mixed with chameleons in an approximately similarly shaped chameleon mode. The RF source was then shut off, and the usual high-sensitivity ADMX receiver chain recorded the power spectrum of the ADMX cavity over another 10 minutes. The cavity resonance was shifted and the process repeated. With these data, we were able to exclude a large region of chameleon-photon coupling over a range of chameleon masses (Fig. 3.1-3). That such a short run produced this result demonstrates the power for these searches of having high sensitivity to electromagnetic radiation. A paper detailing the results of the search has been submitted for publication.

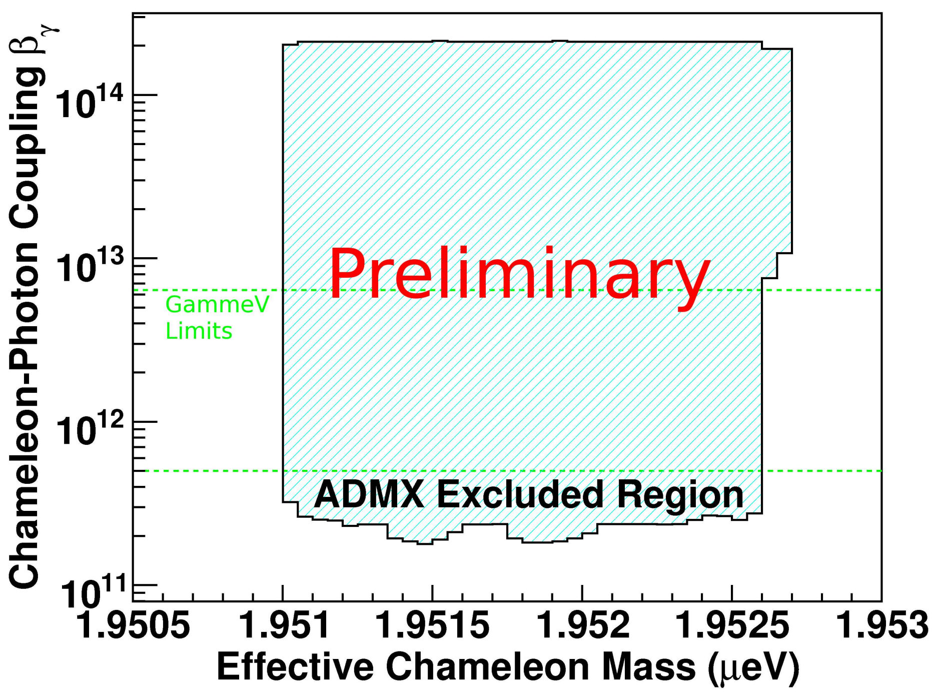

Figure 3.1-3. Excluded region of chameleon-photon coupling and chameleon masses from the chameleon-search operation of ADMX. Results from a FermiLab experiment are also shown.

Another search for beyond-standard-model particles using ADMX is a search for hidden sector photons. These particles arise in theories with extra hidden symmetries. Such new photons behave like extremely weakly-coupled photons having mass. These low-mass hidden sector photons may mix with normal photons, and this mixing can be exploited in a search by the use of two microwave cavities tuned to the same frequency. If one cavity is excited by a signal source, the photons in the cavity may mix with hidden sector photons, which due to their feeble coupling to normal matter and radiation, are then free to escape the cavity. They may then reconvert to photons in the other cavity, thereby providing a means to weakly-couple the two cavities. Additionally, this search is able to take place during normal axion-search operations with only the addition of a source cavity tuned to the frequency of the detector cavity. A demonstration run of this type of search has been completed. The excluded region of hidden-sector photon mixing and mass is shown, along with prior results from other groups.

Note how competitive is the short ADMX test-run result, another consequence of the high sensitivity of ADMX to electromagnetic radiation (Fig. 3.1-4).

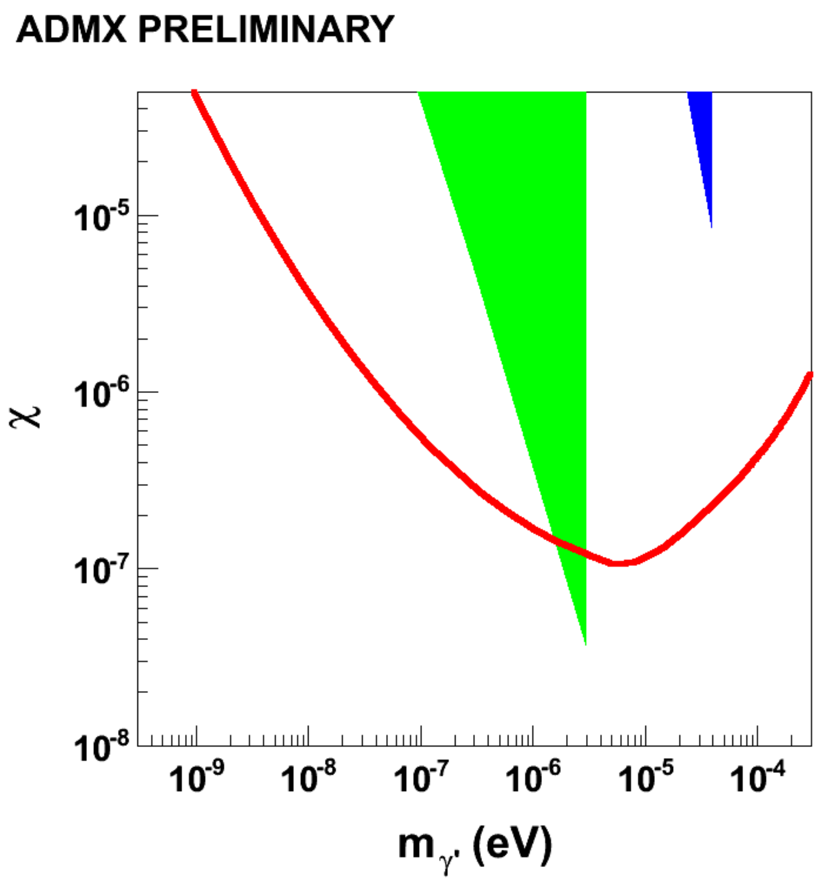

Figure 3.1-4. The preliminary excluded region of hidden-sector-photon mixing at 95% c.l. from ADMX (large green triangle region). Also shown is the competing RF cavity limit (small blue triangle), and the limit from deviations from $1/r^2$ electric field (region above red line)

In an early SAGENAP review of the ADMX upgrade program, operation of SQUIDs in high magnetic fields was deemed very high risk. We therefore adopted a two-phase upgrade path: first, demonstrate the use of SQUIDs (Phase I) in the ADMX high-magnetic-field environment, but with the original pumped-LHe cooling, second, (Phase II) with the SQUID operation thus demonstrated, cool the amplifiers and cavity with a dilution refrigerator to realize a system noise temperature 200 mK.

This second phase was triggered by the successful Phase I operation. The large ADMX magnet is scheduled to move to CENPA in summer 2010, beginning a 3-year Phase II construction program. This program mainly consists of adding the dilution refrigerator system, but also includes upgrades to the liquid helium systems. As mentioned, this is the "ultimate" dark-matter axion search.

3.2 Acceleration predictions for moving the ADMX cryostat through a mock move experiment

J. A. Heilman, L. J. Rosenberg, G. Rybka, K. Tracy, and D. I. Will

We are in the process of moving the ADMX main magnet and cryostat from Lawrence Livermore National Lab (LLNL) to CENPA. The magnet coil and helium can are suspended from the cryostat top plate by three support tubes, essentially creating a pendulum inside of the main vacuum can. It is conceivable that, with enough of an impulse, the pendular mass could deflect sufficiently to cause internal damage to several of the cryostat's systems. Therefore we performed a study of the forces the cryostat might experience in transit.

After discussing the challenges involved in moving the experiment to CENPA with experts and vendors we have decided to ship it on a double-drop air ride trailer. This will give us the most cushioning as well as keep us under the height of most highway overpasses. In November, 2009 we traveled to San Francisco, CA to run an experiment with a qualified moving vendor in the area. We loaded a 12-ton forklift as a test mass on the type of tractor and trailer we would likely use for moving the cryostat and instrumented it with shock loggers at strategic locations to record the forces on the mass. We then drove the rig around local freeways as far north as Sacramento and then back to the vendor's yard.

We collected 8 hours of acceleration data over the 253 miles we drove the test mass. Some of the most interesting data collected were from one of the instruments that was designed with a very high sample rate but only triggered a write cycle at a user defined threshold[1]. This transient logger recorded two seconds of data sampled at 512 Hz at each trigger event. This gave us a detailed look at the larger acceleration events felt by the test mass and how they dissipated. For assessing damage to the cryostat we care about how far the pendulum is displaced from equilibrium. While there are several possible failure modes, they are all related to pendular displacement.

The other thing we are interested in is the power spectrum of the accelerations felt by the test mass. The cryostat pendulum weighs approximately 10 tons, so high frequency accelerations will not deflect the cryostat very much in their cycle time even if they have large amplitude. Our data show a low amplitude but high power dominant 5-Hz component, with high amplitude components being of frequencies over 50 Hz and dying off very quickly. This is encouraging because it tells us that the very high instantaneous accelerations die off quickly and will not deflect the pendulum very much. Still, the high power 5-Hz vibration could cause problems if it excites a resonance inside the cryostat. Analysis of the design of the motion restraints inside the cryostat suggest a resonant frequency of around 35 Hz alleviating any worries of a low frequency excited resonance.

Criteria for live monitoring of the cryostat move have been developed from the data collected and analysis of the cryostat design. The move is scheduled for late Spring, 2010.

[1]OMEGA TSR101 Triggered Shock Recorder

3.3 Continued studies of systematic errors in the "axion" torsion-balance experiment

E. G. Adelberger, F. Fleischer, B. R. Heckel, and S. A. Hoedl

Our torsion pendulum search for an axion-like particle (ALP) offers a significant improvement over the most recent such measurement[1]. A torsion-pendulum based search is possible because an ALP will mediate a macroscopic pseudo-scalar potential between polarized and unpolarized fermions. By observing the motion of a planar torsion pendulum (source of *unpolarized* fermions) positioned near the pole faces of an energized ferromagnet (source of *polarized* fermions), we can observe such a force. Note, however, that given the experimental limit, $\Theta_{QCD} < 3 \times 10^{-10}$, our apparatus is not sensitive to conventional axion models.

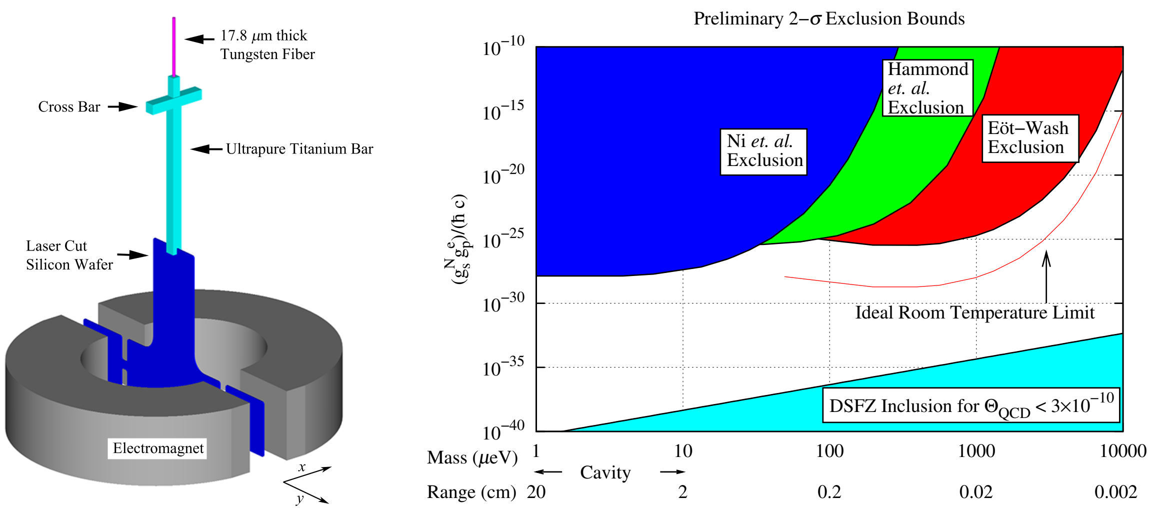

Figure 3.3-1. A scale diagram of one of our pendulums positioned in between the magnet pole faces; our exclusion bounds compared with recent experimental searches and the expected coupling for $\Theta_{QCD} < 3 \times 10^{-10}$.

In the past year, we have developed a data taking strategy that mitigates the most troubling sources of systematic errors, such as a frozen ferromagnetic impurity in or on the silicon. In addition, we have constrained five other types of systematic errors: a temperature asymmetry in the two magnet states, a magnetic-field dependent difference in the apparatus' alignment to local vertical, an asymmetry in the magnetic field *squared* in the two magnet states, a steady external magnetic field and a steady external magnetic field gradient. The correction due to each systematic error is far below the statistical noise. We find that in total, the uncertainty in the systematic errors is a factor of twenty smaller than the statistical error. At present, our data set puts a limit on a macroscopic parity and time violating force which is more than 10 trillion times more restrictive than Hammond *et al.* for an ALP heavier than 1.3 meV. We have modified the apparatus slightly to gain additional sensitivity to lighter ALPs and are presently taking data in this new configuration.

[1]CENPA Annual Report, University of Washington (2009) p. 42.

4 Nuclear Astrophysics

4.1 Measurements of ^{33}S$(p,\gamma)^{34}$Cl at nova temperatures

B. G. Delbridge, B. M. Freeman, A. García, A. Knecht, A. Parikh,* A. L. Sallaska, and C. Wrede

Presolar grains are micron sized grains of material found in some meteorites, with isotopic ratios differing from those in the solar system at large. The majority of presolar grains that have been examined are thought to be from asymptotic giant branch (AGB) stars or supernovae. A possible astrophysical source for grains of unknown origin is classical novae. Existing nova models predict an overproduction factor for ^{33}S of 150 times the solar abundance[1]. This prediction would allow for identification of presolar grains from novae but is subject to a large uncertainty due to a lack of data on the main destruction mechanism for ^{33}S in novae, the ^{33}S$(p,\gamma)^{34}$Cl reaction. Additionally, the ^{33}S$(p,\gamma)^{34}$Cl reaction populates the metastable state, ^{34m}Cl ($t_{1/2}$=32m). The gamma rays emitted following the β^+ decay of this state have been suggested as a possible observable signature of a classical nova[2].

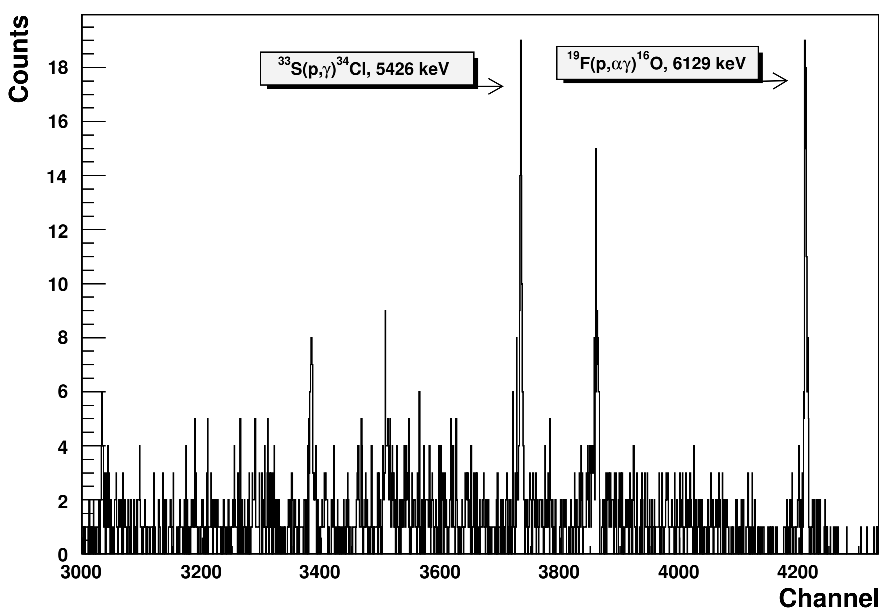

Figure 4.1-1. ^{33}S$(p,\gamma)^{34}$Cl spectrum from the E_r=432 keV resonance showing the 5426 keV branch as well as the 6129 keV background from the ^{19}F$(p,\alpha\gamma)^{16}$O reaction. Photopeaks are labeled.

Recent measurements of the ^{34}S(^{3}He,t)^{34}Cl and ^{33}S(^{3}He,d)^{34}Cl reactions have identified several potential resonances in the energy range relevant for novae, within 600 keV of the

*Physik Department E12, Technische Universität München, Garching, Germany.
[1]J. José, A. Coc, and M. Hernanz, Astrophys. J. **560**, 897 (2001).
[2]A. Coc *et al.*, Phys. Rev. C **61**, 015801(1999).

^{33}S+p threshold (5143 keV)[3]. In May 2010 an experiment using the DRAGON facility at TRIUMF is scheduled to make measurements of strengths for potential ^{33}S$(p,\gamma)^{34}$Cl resonances in this energy range using inverse kinematics with a recoil separator and BGO gamma ray detectors[4]. We are attempting to measure gamma ray branching ratios for these resonances using HPGe detectors. When combined with data from the TRIUMF experiment our data are expected to result in more accurate resonance strength measurements. Additionally, new resonances with strong branchings to the ^{34m}Cl state would increase the chances of using ^{34m}Cl as a nova observable.

Our experimental setup[5] was initially used to measure the ^{22}Na$(p,\gamma)^{23}$Mg reaction and consists of a beamline with a target chamber and two germanium detectors with cosmic ray shielding. We used OFHC copper substrates implanted with approximately 10^{16} ^{33}S atoms at an energy of 45 keV over a 5 mm diameter. These targets were produced at CENPA using the General Ionex 860 sputter ion source (SpIS) during the fall of 2009.

Data were taken from January through March 2010 and data analysis is set to begin in April 2010. We were generally able to maintain beam currents of around 45 μA and took approximately 135 hours of data. We spent time taking data at 6 potential resonances as well as 3 that have been previously measured[6]. Extra time was spent measuring a potential resonance at E_p=273 keV where a previous ^{33}S$(p,\gamma)^{34}$Cl measurement detected a small increase in yield[7]. During our data collection the ^{33}S$(p,\gamma)^{34}$Cl yield at the energies of the potential resonances was low. If we are unable to find statistically significant branches from these resonances during our data analysis we will attempt to place rough upper limits on their resonance strengths and confirm the branching ratios of previously measured resonances.

We face several challenges in the analysis of our data including a strong background at lower energies from the decay of residual ^{22}Na in the beamline, carbon build up on the target, and a relatively weak background at higher energies due to the ^{19}F$(p,\alpha\gamma)^{16}$O reaction. Additional problems are expected to arise when attempting to set upper limits on resonance strengths since much of the experiment was run under the assumption that we would only be attempting to make relative strength measurements to determine branching ratios. Depending on the results of our data analysis and the results from the DRAGON experiment in May 2010 we may consider collecting additional data. If a strong resonance is found in the DRAGON experiment, we will focus on obtaining branching ratios for that resonance.

[3] A. Parikh *et al.*, Phys. Rev. C **80**, 015802 (2009); private communication.
[4] A. Parikh *et al.*, TRIUMF-ISAC Experiment S1122.
[5] CENPA Annual Report, University of Washington (2008) p.43.
[6] F.B. Waanders *et al.*, Phys. Nucl. Phys. **A411**, 81 (1983).
[7] F.B. Waanders, private communication.

4.2 Determining the reaction rate for ^{22}Na(p,γ): final results

T. A. D. Brown, L. Buchmann*, J. A. Caggiano*†, A. Garcia, D. A. Hutcheon*, D. F. Ottewell*, C. Ruiz*, A. L. Sallaska, K. A. Snover, D. W. Storm, C. Vockenhuber*, and C. Wrede

The isotope ^{22}Na is a long sought after gamma emitter ($t_{1/2} = 2.6$ yr, $E_\gamma = 1.275$ MeV) that has yet to be observed with orbiting gamma ray telescopes. It has been proposed that the principal production sites may be novae, and because of its short half life, the ^{22}Na ejecta could be used as a tool to investigate nova outbursts. Thermonuclear reaction rates involved in the production and destruction of this nuclide are essential inputs to models of nova nucleosynthesis. We have directly measured the resonances in the ^{22}Na(p,γ) reaction which contribute significantly in the temperature region 0.1 to 0.4 GK. Our ^{22}Na targets were fabricated at TRIUMF, and we have previously reported progress for this experiment[1], involving a relative analysis. This year we have focused on an absolute analysis, which has only been done for this reaction in one other experiment[2]. Critical elements for this analysis include absolute detector efficiency, beam density, and total number of ^{22}Na atoms.

The detector efficiency was established first in an absolute way with a calibrated ^{60}Co source with $E_\gamma = 1332$ keV and then in a relative way up to 11 MeV by performing ^{27}Al(p,γ) on a thick aluminum target. A ^{24}Na source was also fabricated to determine the relative efficiency at 2754 keV. At gamma-ray energies in between, a PENELOPE simulation was then used to interpolate the efficiency, on which a 5% systematic error has been placed.

The beam density, which is the number of beam particles on target per unit area, was measured with ^{27}Al(p,γ) by comparing yields on a thick target to a "coin" target. This coin target had the same physical dimensions as the ^{22}Na targets but had a thick, 5 mm diameter disc of ^{27}Al in the center. The yields were measured at different times with different beam tunes with $E_R = 405$ and 992 keV. Systematic errors were explored with physical measurements of the beam area based on burn marks on the target and also by simulations.

The total number of atoms can be extracted from the total charge implanted and from the measured activity *in situ*, and target degradation must be monitored. As the total number of atoms is proportional to the integral of the excitation function over the resonance, repeated measurements of a strong resonance were performed to monitor target degradation. Due to the 200 Å protective layer of chromium, the two main ^{22}Na targets experienced minimal degradation over the bombardment of 20 C per target.

During the previous year, we performed a number of measurements with ^{23}Na implanted targets in order to validate our experimental techniques with resonances whose strengths are well-known. We find the absolute strengths for the resonances on ^{22}Na from 214 to 607 keV proton energy to be significantly larger than results in the literature. We are presently preparing these results for publication.

*TRIUMF, Vancouver, BC V6T 2A3, Canada
†Presently at LLNL, Livermore, CA 94550
[1] CENPA Annual Report, University of Washington (2009) p. 48.
[2] S. Seuthe *et al.*, Nucl. Phys. **A514**, 471 (1990).

4.3 Correlations between solar activity and nuclear decay rates?

E. G. Adelberger, A. García, A. S. C. Palmer, and H. E. Swanson

In a recent publication, Fischbach and Jenkins[1] found that the observed decay rate for a sample of ^{54}Mn anomalously decreased during the solar flare of 13 December, 2006. Fischbach and Jenkins propose that solar activity might have an effect on the nuclear decay rates of certain isotopes. Since this initial observation there have been no other independent observations confirming or denying this proposed effect. We are running an experiment to look for the claimed effect.

Our experiment consists of samples of ^{54}Mn and ^{241}Am which are placed next to a HPGe detector and shielded by lead bricks so as to prevent possible interference from cosmic radiation. ^{54}Mn decays via K-capture with a halflife of 312 days and emits an 835 keV γ ray. ^{241}Am decays via α decay with a halflife of 433 years and emits a 60 keV γ ray. These γ ray events are recorded together on a series of single histograms each spanning 2-4 hour periods. The ratio of ^{54}Mn to ^{241}Am background-subtracted counts is then taken so as to reduce systematic effects. Fig. 4.3-1 shows the ratio which exhibits the expected ^{54}Mn half-life dependence. For comparison we show the solar activity data from the NOAA GOES-14 satellite[2].

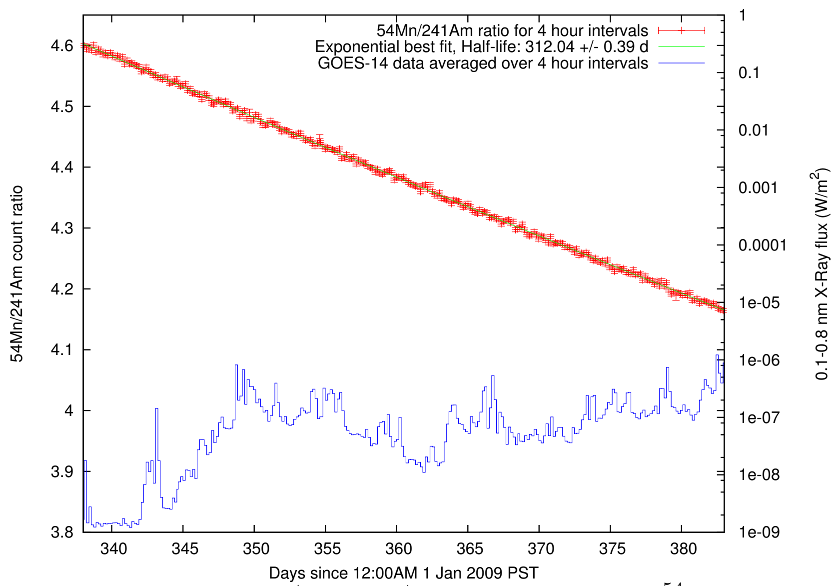

Figure 4.3-1. The upper curve (left scale) shows the ratio of ^{54}Mn decay counts to ^{241}Am background-subtracted decay counts in 4 hour intervals from 4 December, 2009 to 18 January, 2010 with an exponential best fit. The lower curve (right scale) shows solar data over the same period averaged over each interval.

As shown in Fig. 4.3-2 we have so far not observed any of the claimed correlations. Given the results of the original Fischbach and Jenkins paper an effect of 0.15$\pm$ 0.02% would be

[1] E. Fischbach and J.H. Jenkins, arXiv:0808.3156 [astro-ph] 22 Aug 2008.

[2] NOAA/NWS Space Weather Pred. Ctr., http://www.sec.noaa.gov/

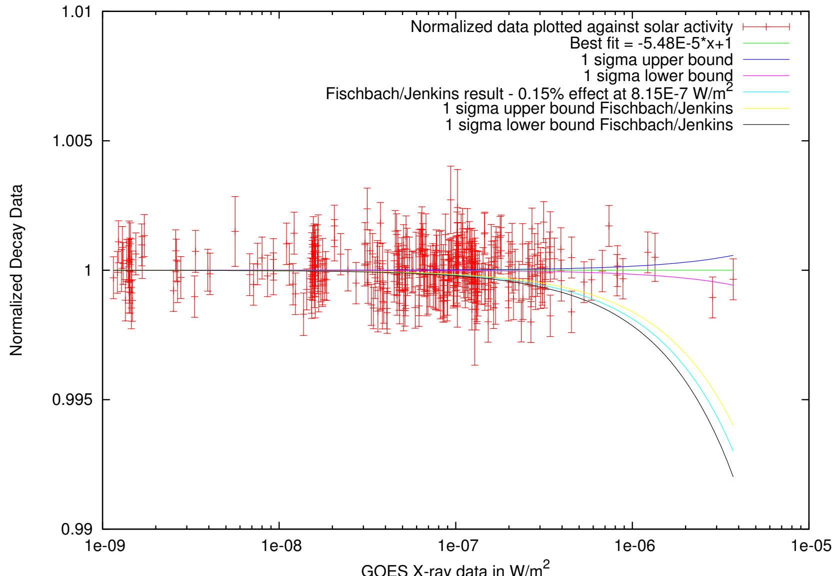

Figure 4.3-2. The ^{54}Mn/^{241}Am 4 hour data normalized to an exponential best fit versus solar activity from GOES over each period plotted in logarithmic scale. A linear best fit of the data is given along with 1σ upper and lower bounds showing consistency with zero. Fischbach and Jenkins' results are plotted in the same manner and are seen to trend downward, assuming no effect at zero solar activity. Decay data is from the period of 1 December, 2009 to 25 January, 2010.

expected at an average measured solar X-ray flux of 8.15×10^{-7} Watts/m^2 in the 0.1-0.8 nm regime. Our results indicate an effect of 0.000±0.013% at the same rate of solar activity, excluding the claimed effect.

5 Nuclear Structure

5.1 Electron capture on ^{116}In and 2β decay

A. Algora*, J. Äystö†, T. Eronen†, A. García, J. Hakala†, V. S. Kolhinen†,
I. D. Moore†, H. Penttilä†, M. Reponen†, J. Rissanen†, A. Saastamoinen†, S. K. Sjue‡,
H. E. Swanson, and C. Wrede

The observation of a neutrinoless double beta ($0\nu2\beta$) decay would determine the effective neutrino mass if the corresponding nuclear matrix element were known. Two candidates for this exotic mode are the $0^+ \rightarrow 0^+$ double beta decays of ^{100}Mo to ^{100}Ru, and ^{116}Cd to ^{116}Sn. Calculations of the $0\nu2\beta$ decay matrix elements for these systems may be bench-marked using quantities that are experimentally accessible such as the regular single and double β decay rates. An extensive experimental data set is available for the $A = 100$ system, but the $A = 116$ system could provide a simpler test because of the possible effects of deformation in the $A = 100$ system. The branch for electron-capture decay of the intermediate nucleus ^{116}In ($J^\pi = 1^+$) to the ground state of ^{116}Cd is particularly interesting because the $2\nu2\beta$ decay of ^{116}Cd may be dominated by the virtual transition through the ground state of ^{116}In. Measurements of this branch can also be used to test the accuracy of charge-exchange reactions in reproducing the Gamow-Teller strength.

At the time of the last annual report, we were preparing for an experiment to measure the small ($\approx 2 \times 10^{-4}$) electron-capture branch in the decay of ^{116}In at the University of Jyväskylä[1]. We completed the assembly and testing of the decay station, detectors, and associated electronics at CENPA in August 2009, and shipped the apparatus to the University of Jyväskylä's IGISOL facility. The apparatus was reassembled at the end of IGISOL on schedule for our five days beam time in September 2009. Ions of ^{116}In were produced using the ^{115}In(d,p) reaction on a natural indium target, separated from ions of different mass using a Penning trap, and delivered to the decay station. Roughly 1500 ions/second of ^{116g}In were counted at the decay station together with substantial quantities of the isomers ^{116m1,m2}In, which could not be mass-separated. Electron-capture decays of the ^{116}In ground state were measured by detecting the corresponding Cd X-rays with a planar Ge detector. Preliminary analysis suggests that our measurement will be competitive with the only other measurement of this branch[2]. Detailed data analysis is scheduled to commence in summer of 2010.

---

*Instituto de Física Corpuscular, University of Valencia, Valencia, Spain
†Department of Physics, University of Jyväskylä, V. V. Elomaa†, Jyväskylä, Finland
‡TRIUMF, Vancouver, BC, Canada

[1] CENPA Annual Report, University of Washington (2009) p. 54.

[2] M. Bhattacharya *et al.*, Phys. Rev. C **58**, 1247 (1998).

5.2 Precise measurements of ^{20}Na, ^{24}Al, ^{28}P, ^{32}Cl, and ^{36}K

S. Bishop*, A. A. Chen†‡, J. A. Clark§, C. M. Deibel§¶, K. Eppinger*, T. Faestermann*, B. M. Freeman, A. García, R. Hertenberger‖, R. Krücken*, O. Lepyoshkina*, A. Parikh*, G. Rugel*, K. Setoodehnia†, H.-F. Wirth‖, and C. Wrede

Precise, accurate nuclear masses and excitation energies for unstable proton-rich nuclides are valuable for a number of reasons. For example, they may contribute to studies of rapid proton capture (rp)-process nucleosynthesis and superallowed $0^+ \rightarrow 0^+$ β decays. We have measured the (^{3}He,t) reactions leading to ^{20}Na, ^{24}Al, ^{28}P, ^{32}Cl, and ^{36}K using 32-MeV ^{3}He beams and the Q3D magnetic spectrograph at the Technical University of Munich. Thin, ion implanted, carbon foil targets of ^{20}Ne, ^{24}Mg, ^{28}Si, ^{32}S, and ^{36}Ar were prepared using the ion sources, injector deck, and low energy beam line at CENPA.

Using the known momenta of tritons from the ^{36}Ar(^{3}He,t)^{36}K reaction for calibration, the masses of ^{20}Na, ^{24}Al, ^{28}P, and ^{32}Cl have been determined to 1.1 or 1.2 keV. The masses of ^{20}Na and ^{32}Cl are found to be in good agreement with the values from the 2003 Atomic Mass Evaluation (AME03)[1], and the precision has been improved by a factor of 6 in both cases. The masses of ^{24}Al and ^{28}P are both found to be in disagreement with the values from AME03 by $> 3\sigma$ and the precision has been improved by a factor of 2.5 in both cases. The new masses for ^{24}Al and ^{28}P resolve a discrepancy in the energy of the lowest-lying resonance in the ^{23}Mg$(p,\gamma)^{24}$Al reaction between direct[2] and indirect[3] measurements, and further constrain the measured strength of the resonance. The new mass for ^{32}Cl combined with other data yields a new Q_{EC} value for the superallowed $0^+ \rightarrow 0^+$ β decay of ^{32}Ar that will affect the results of a search for scalar current contributions to nuclear β decay[4], and a test of the isospin symmetry breaking correction to the ft value for this decay[5].

The excitation energies of proton-unbound states of astrophysical interest in ^{32}Cl and ^{36}K have also been determined. The ^{32}Cl measurements resolve a systematic discrepancy of ≈ 11 keV between two previous measurements. The excitation energies of ^{36}K levels are found to be higher than previous measurements by ≈ 10 to 40 keV, and the uncertainties have been reduced by over an order of magnitude. At least one new proton-unbound level has been discovered in ^{36}K, and the ^{36}K-^{36}Cl mirror analog-level assignments have been rearranged accordingly. As a result, the thermonuclear ^{35}Ar$(p,\gamma)^{36}$K reaction rate is found to be much higher than, and inconsistent with, the currently accepted rate[6].

---

*Physik Department, Technische Universität München, Garching, Germany
†Department of Physics and Astronomy, McMaster University, Hamilton, ON, Canada
‡DFG Cluster of Excellence Universe, Technische Universität München, Garching, Germany
§Physics Division, Argonne National Laboratory, Argonne, IL, USA
¶Joint Institute for Nuclear Astrophysics, Michigan State University, East Lansing, MI, USA
‖Fakultät für Physik, Ludwigs-Maximilians-Universität München, Garching, Germany
[1] G. Audi, A. H. Wapstra, and C. Thibault, Nucl. Phys. **A729**, 337 (2003).
[2] L. Erikson *et al.*, Phys. Rev. C (accepted).
[3] G. Lotay *et al.*, Phys. Rev. C **77**, 042802 (2008); D. W. Visser *et al.*, Phys. Rev. C **76**, 065803 (2007).
[4] E. G. Adelberger *et al.*, Phys. Rev. Lett. **83**, 3101 (1999).
[5] M. Bhattacharya *et al.*, Phys. Rev. C **77**, 065503 (2008).
[6] C. Iliadis *et al.*, Astrophys. J. **524**, 434 (1999).

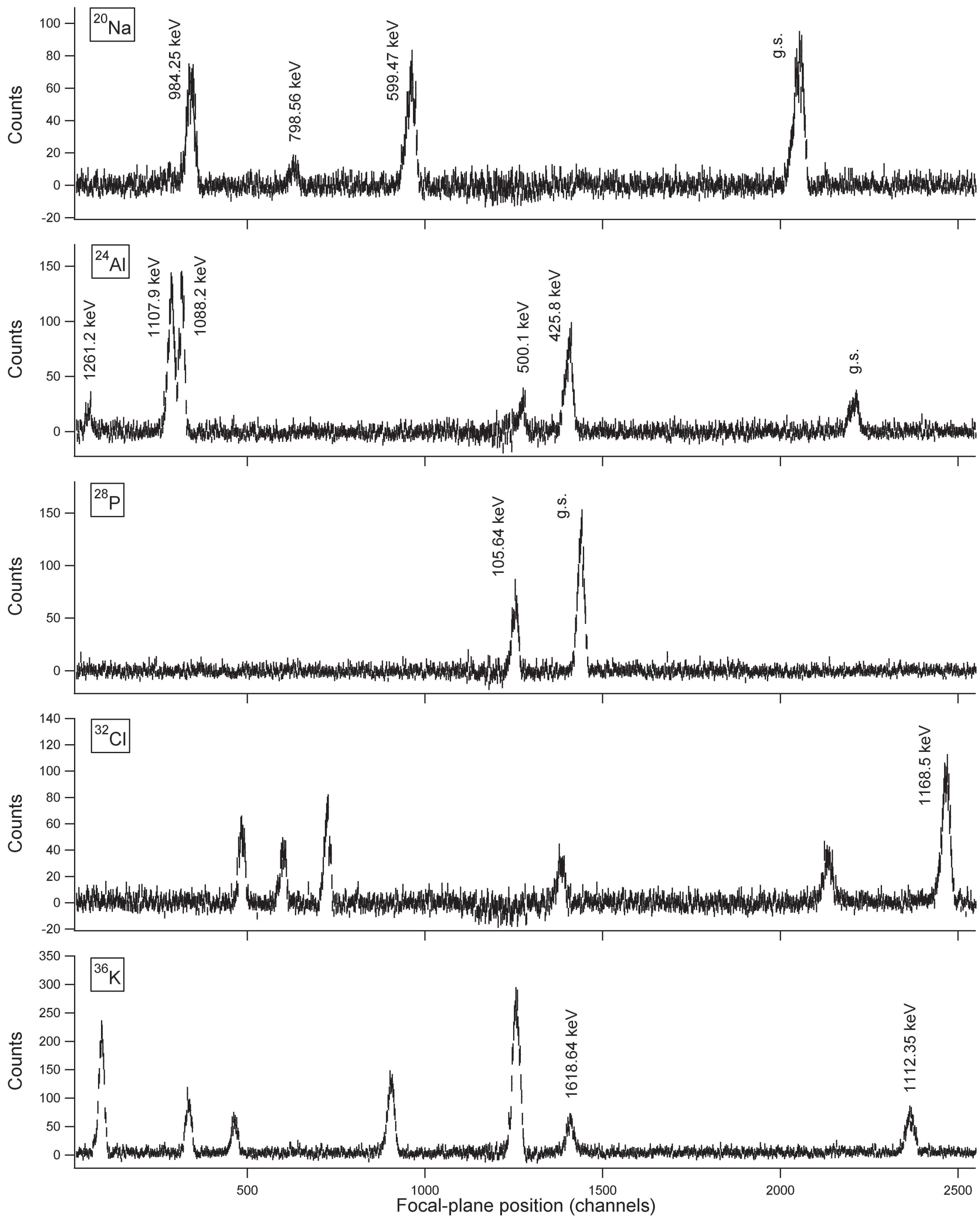

Figure 5.2-1. Q3D focal-plane position spectra of tritons from the (^{3}He,t) reactions leading to the indicated nuclides, acquired at $\theta_{lab} = 10°$. For each bin, the datum is plotted as a vertical line with a length that spans the standard deviation. Increases in fluctuations between channels 1100 and 1300 are due to the subtraction of background from the ^{13}C(^{3}He,t)^{13}N reaction. Peaks used in the mass measurement are labeled by "g.s." for ground states and the excitation energy for excited states.

5.3 Mass of ^{31}S with the Canadian Penning Trap

S. Caldwell[*†], A. Chaudhuri[‡†], J. A. Clark[†], C. M. Deibel[§†¶], J. Fallis[‡†], A. García, S. Gulick[‖], D. Lascar[**†], G. Li[‖†], G. Savard[†*], K. S. Sharma[‡], M. Sternberg[*†], T. Sun[†], J. Van Schelt[*†], and C. Wrede[¶]

At the time of the last annual report we were preparing for our second period of allotted beam time at Argonne-ATLAS to measure the mass of ^{31}S with the Canadian Penning Trap[1]. During this period in May of 2009 we successfully acquired cyclotron resonances for $^{31}S^+$ (Fig. 5.3-1) and the calibrants COH_3^+ and O_{16}^{2+}.

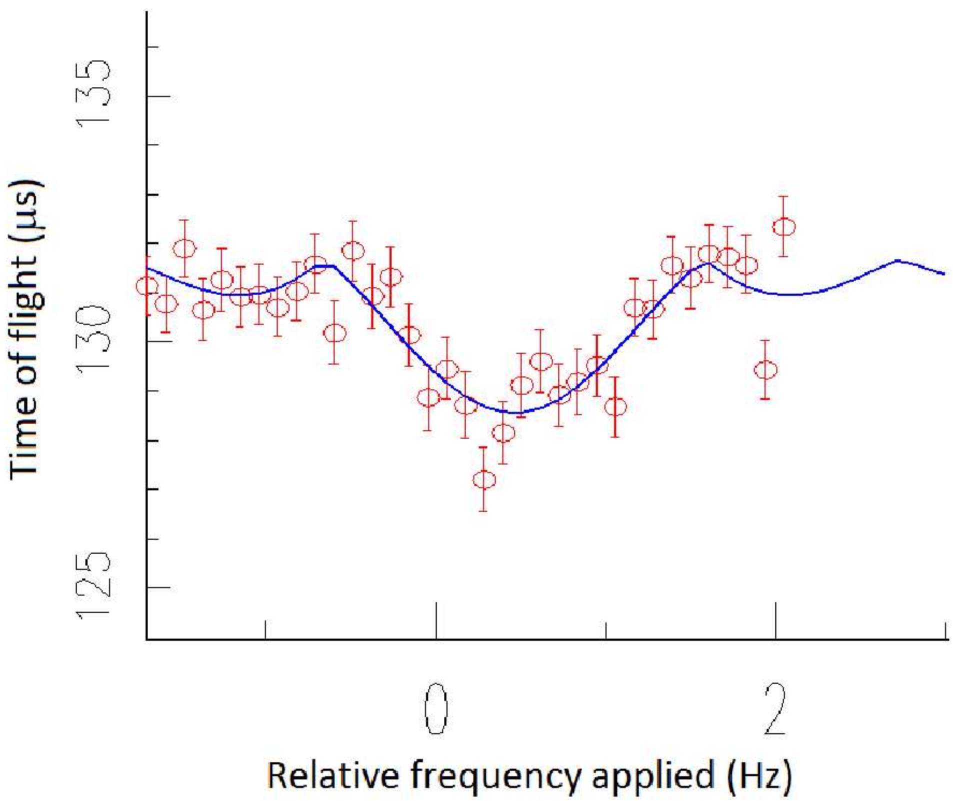

Figure 5.3-1. Time of flight spectrum for $^{31}S^+$ ions ejected from the Canadian Penning Trap as a function of applied frequency. The minimum occurs at the cyclotron frequency.

The data analysis has progressed to the point that a central value for the mass of ^{31}S has

[*]Department of Physics, University of Chicago, Chicago, IL, USA
[†]Physics Division, Argonne National Laboratory, Argonne, IL, USA
[‡]Department of Physics and Astronomy, University of Manitoba, Winnipeg, MB, Canada
[§]Joint Institute for Nuclear Astrophysics, Michigan State University, East Lansing, MI, USA
[¶]Co-spokesperson for Argonne-ATLAS Experiment 1259.
[‖]Department of Physics, McGill University, Montreal, QC, Canada
[**]Department of Physics and Astronomy, Northwestern University, Evanston, IL, USA
[1]CENPA Annual Report, University of Washington (2009) p. 55.

been determined and a statistical uncertainty of 0.4 keV has been assigned. The analysis of systematic effects that may contribute additional uncertainties is in progress. The preliminary value for the mass is $\approx$ 3 keV different from the only other measurement of comparable precision[2], which carried an uncertainty of 1.5 keV and was adopted in the 2003 Atomic Mass Evaluation[3].

Combining our new value for the mass of ^{31}S with the energy of the beta-delayed proton emission from the lowest $T = 2$ level in ^{32}Cl yields a new value for the mass excess of this level that is significantly different from previous values. This result further constrains the isobaric multiplet mass equation (IMME) fit for the $A = 32$, $T = 2$ quintet (which was already the most stringent test of the IMME)[4,5] and confirms the failure of the quadratic form of the IMME for this multiplet with unprecedented confidence.

Using the known mass of ^{32}Ar together with the mass excess of the lowest $T = 2$ level in ^{32}Cl we derive a new Q_{EC} value for the superallowed $0^+ \rightarrow 0^+$ β decay of ^{32}Ar. This new value has an effect on the results of a search for scalar current contributions to nuclear β decay[6], and a test of the isospin symmetry breaking correction to the ft value for this decay[7].

[2] A. Moalem and B. H. Wildenthal, Phys. Rev. C **8**, 1961 (1973).
[3] G. Audi, A. H. Wapstra, and C. Thibault, Nucl. Phys. **A729**, 337 (2003).
[4] S. Triambak *et al.*, Phys. Rev. C **73**, 054313 (2006).
[5] A. A. Kwiatkowski *et al.*, Phys. Rev. C **80**, 051302(R) (2009).
[6] E. G. Adelberger *et al.*, Phys. Rev. Lett. **83**, 3101 (1999).
[7] M. Bhattacharya *et al.*, Phys. Rev. C **77**, 065503 (2008).

6 Relativistic Heavy Ions

6.1 Summary of event structure research

T. A. Trainor

In previous work we established a direct quantitative relation between pQCD calculations and measured "hard-component" data, relating a calculated minimum-bias pQCD parton spectrum and fragmentation functions to measured hard-components (fragment distributions) in spectra and correlations. We also observed "elliptic flow" v_2 as an isolated azimuth quadrupole (v_2) component in 2D angular autocorrelations.

In the past year we have extended p_t/y_t-integrated measurements of jet and azimuth quadrupole correlations to Cu-Cu collisions and improved the accuracy of 2D model fits. We have extracted y_t-dependent jet and quadrupole correlations and converted the latter to *quadrupole spectra* which directly reveal the boost distribution associated with the quadrupole, a primary prediction of hydro theories.

In related work we have developed methods to infer jet properties and fragment spectra accurately from jet angular correlations. Detailed comparisons between fragment spectra derived directly from minimum-bias jets and pQCD predictions are then possible.

General topics include

- Broad survey of y_t-integrated jet angular correlations for 62 and 200 GeV Au-Au and Cu-Cu, both number and p_t correlations
- First factorization of $v_2(\sqrt{s_{NN}}, p_t, b)$ to obtain separate energy-, centrality- and p_t-dependent factors, leading to a compact and accurate parametrization
- Establishing near centrality *in*dependence of transverse boost in quadrupole spectra from 200 GeV Au-Au collisions, with implications for hydro interpretations of v_2.
- Determining the centrality evolution of minimum-bias jet properties in 200 GeV Au-Au collisions from p_t-integrated 2D jet angular correlations
- Determining the centrality dependence of the absolute minijet contribution to total particle yield in 200 GeV Au-Au collisions
- Measurements of the marginal p_t/y_t dependence of jet properties (same-side 2D correlation peak, amplitude and widths)
- Extracting minimum-bias parton (minijet) fragment spectra from marginal-on-y_t 2D jet angular correlations
- Comparing fragment spectra inferred from jet correlations with spectrum hard components and pQCD predicted fragment distributions

6.2 Tracking issues affecting two particle angular correlations in STAR

D. J. Prindle and T. A. Trainor

Precision inner-tracking (IT) silicon detectors (SSD and SVT) were installed within the STAR TPC detector for data taken between 2005 and 2008. Tracks reconstructed in the TPC and matched to measured space points in the IT detectors have an improved distance of closest approach (DCA) to the primary vertex, which is important when searching for particles that decay near the primary vertex. Tracks from the TPC incorrectly matched with IT detector hits have their parameters adversely affected. The Cu-Cu data taken in 2005 and the Au-Au data taken in 2007 had the IT included in the track finding and fitting.

200 GeV Au-Au data taken in 2007 also had a sample of 1M events reconstructed without the IT, allowing a direct comparison of tracking. The first panel of Fig. 6.2-1 shows the like-sign 2D autocorrelation on $(\eta_\Delta, \phi_\Delta)$ for the 20-30% centrality bin when the IT was omitted from reconstruction. We used tracks that are associated with the primary vertex and pass quality cuts. The second panel is for the same dataset reconstructed with the IT included in reconstruction. There is a clear difference, with track pairs missing near $(0, 0)$.

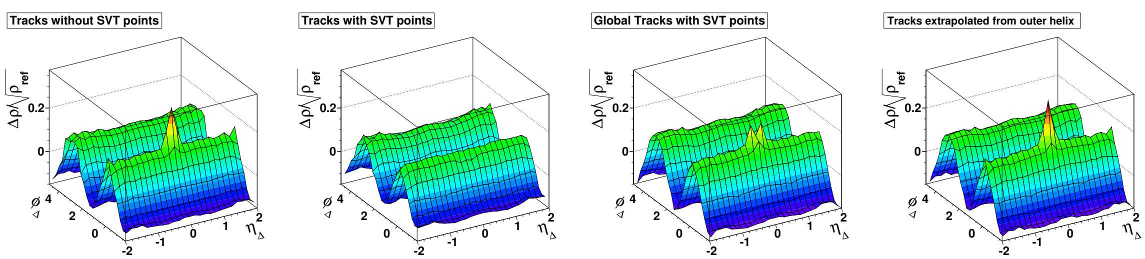

Figure 6.2-1. Panel 1: like-sign joint autocorrelation on $(\eta_\Delta, \phi_\Delta)$ for 20-30% central 200 GeV Au-Au data taken during 2007 and produced without the IT in the tracking code. Panel 2: the same data with the IT included in the tracking code. Panel 3: the same data using global tracks . Panel 4: the same data from panel 3, but using outer helix parameters to estimate track η and ϕ at its closest approach to the primary vertex.

Tracks are associated with the primary vertex based on their DCA, a 3 cm cut without the IT and based on DCA uncertainty with the IT. We expect the IT to reject about 10% of tracks as primaries, the majority due to weak decays. We check if this is the cause of the reduced correlation strength by using tracks before the primary vertex association and imposing a 3 cm DCA cut. The result, shown in panel 3 of Fig. 6.2-1, does not recover all the correlation strength. Finally we extrapolated from the outer helix to calculate η and ϕ at the DCA. [The STAR track model is based on a Kalman filter that accounts for energy loss and multiple Coulomb scattering (MCS), with helical approximations stored at the first and last measured points.] Shown in panel 4, this recovers the correlation strength.

Tracks extrapolated from the outer helix can be several cm from their true position at the DCA. We are only using the angles, and with bins about 15° wide an error of a degree is not too important. We believe that some lower-momentum tracks have incorrect IT points attached during track finding. The Kalman filter then adjusts the direction near the primary vertex to better fit the high resolution points, attributing the angle change to MCS.

6.3 Fitting charge-independent joint angular autocorrelations

D. J. Prindle, R. L. Ray*, and T. A. Trainor

We have measured charge-independent joint angular autocorrelations for a number of centralities, beam energies and collision systems. We describe them with the simplest model possible, with a goal of describing the data as succinctly as possible to give an easy comparison to theory. We find the major components can be interpreted as minimum-bias jets, described by a same-side 2D Gaussian, away-side ridge $-\cos(\phi_\Delta)$ and azimuth quadrupole $\cos(2\phi_\Delta)$. To complete the description we also need a 2D exponential at $(0, 0)$, for HBT and e^+e^- pairs as well as a 1D Gaussian on η_Δ observed in 'soft' fragmentation in p-p collisions. This is a total of 11 parameters controlling shapes that are mostly orthogonal to one another.

Some of the many histograms we fit do not always converge to a true χ^2 minimum. We address this by using multiple independent fitting programs and starting the fits in random places within the parameter space. Some regions of the parameter space fall into local minima, but by sampling widely and finely enough we are confident we do find the global minimum.

With more data and better statistics our simple description gives a poor χ^2 in some cases. Resonances and conservation rules (such as charge and strangeness) do also contribute. The question then arises whether we should include more terms in the fit model or retain the simplest model and describe general features of the data. One of the large contributions to the χ^2 is the failure of the sharp exponential to describe the narrow peak. We have recently worked out the shape due to HBT, and we can accurately model e^+e^-. We hope to replace the 2D exponential with a more accurate description and no additional parameters.

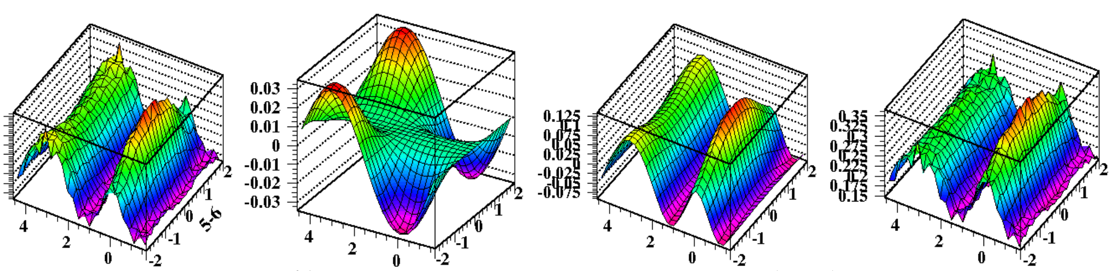

Figure 6.3-1. Panel 1: 0-5% central Au-Au angular autocorrelation (data) after subtracting a sharp peak at the origin. Panel 2: The "residuals" shape added to our initial model to describe the data of panel 1. Panel 3: the new model with the inclusion of the term in panel 2. Panel 4: Data minus non-jet model components revealing jet structure (data).

A more interesting discrepancy between our existing model and data is seen in the away-side ridge for central Au-Au data. The first panel of figure Fig. 6.3-1 shows data after subtracting the narrow e^+-e^-/HBT peak at the origin. There is clearly a saddle shape on the away-side ($\phi_\Delta \sim \pi$). We can describe the Au-Au data more accurately by adding a component shown in the second panel. The third panel shows the modified model. We don't have a physical basis for this term, and there is concern that including it will distract attention from the main features of the data. However, the fourth panel shows data minus non-jet model components revealing nearly-ideal jet structure for central Au-Au collisions.

*University of Texas, Austin

6.4 Progress on understanding the Cu-Cu data

D. J. Prindle and T. A. Trainor

Several issues significantly affect the quality of the 2D autocorrelations on $(\eta_\Delta, \phi_\Delta)$ obtained from Cu-Cu data. The most important problem is multiple-event pileup. At larger beam luminosities there is a significant probability that more than one collision event may be present within the TPC detector at the same time (relatively displaced along the z axis according to relative time). Tracks from a pileup event may be introduced into a triggered event, causing artifacts in correlations. We discussed pileup issues previously[1].

To handle pileup we developed event-topology cuts that look for multiple primary vertices and identify pairs of them as being due to pileup. This technique fails if the pileup collision is too close in time to the triggered collision, especially if the pileup occurs after the trigger. We do a statistical subtraction of the pileup contribution by making analysis passes with and without the pileup rejection cut, using the difference to extrapolate to zero pileup. Pileup extrapolation requires knowing the efficiency of our pileup finding algorithm. We estimated a 75% efficiency by observing that of all pileup events we find twice as many before the trigger, where we expect rejection to be highly efficient, as after the trigger where there are known inefficiencies.

Another way to estimate pileup rejection efficiency is to examine the extrapolated 2D angular autocorrelations as a function of assumed efficiency. We observe that pileup has a signature of a sharp ϕ_Δ-independent ridge centered at $\eta_\Delta = 0$. If this structure is minimized we obtain a centrality-dependent efficiency which is fairly close to 75% for central data but becomes unexpectedly large for peripheral data. Part of the increase may be due to over-subtracting the so-called "soft component" observed in p-p and peripheral Au-Au collisions (where we have little pileup). The presently-remaining uncertainty on the pileup contamination in our Cu-Cu data is significant and compromises soft-component measurements.

We can circumvent tracking issues introduced by inclusions of the SVT by using the track parameters at the last measured point to estimate η and ϕ of the track. This strategy increases angular errors, possibly by as much as 1°. But an error at that level will have no effect on our large-scale correlation structure although it may broaden the sharp peak we observe at the origin. The tracking issue, combined with the (expected) broader HBT peak for the smaller Cu-Cu system (compared to Au-Au), causes the data to be poorly described by a 2D exponential in that region. To improve Cu-Cu fit quality we must either describe that region more accurately or remove it from fits (by adjusting appropriate bin errors) so it does not dominate the fit χ^2. We are currently investigating an improved HBT model.

A second tracking problem is clearly apparent in the like-sign charge combination. For the most-central collisions the same-side jet peak we expect at $(0, 0)$ manifests a central depression. The "hole" appears to be an artifact caused by inclusion of the SVT in track reconstruction. The problem affects unlike-sign correlations in the same way but is not easily visible there because e^+e^- pairs fill in the affected area.

[1]Nuclear Physics Laboratory Annual Report, University of Washington (2009) p. 58.

6.5 Two-particle correlations with marginal y_t cuts for 62 and 200 GeV Au-Au collisions

D. T. Kettler and T. A. Trainor

We have previously used 2D autocorrelations to study angular correlations. An autocorrelation is derived from pair density $\rho(x_1, x_2)$ by averaging it along diagonals parallel to the sum axis in space (x_1, x_2). A 2D autocorrelation is formed by applying that procedure to pairs of angular variables simultaneously, e.g. projection from $(\phi_1, \phi_2, \eta_1, \eta_2)$ onto $(\phi_\Delta, \eta_\Delta)$. The right three panels in the figure below are examples of 2D autocorrelations.

To study the transverse-momentum or -rapidity dependence of 2D angular correlations we make cuts in space $p_t \times p_t$ or $y_t \times y_t$. One useful cut is a marginal p_t (y_t) cut in which one of the particles is restricted to a certain momentum (y_t) range and the other particle is allowed to be from the full momentum range. Those cuts correspond to cross-shaped regions in $y_t \times y_t$ due to the inherent diagonal symmetry, as shown in the first panel of the figure below. Marginal distributions allow us to study the y_t-dependence of correlations with maximum possible statistics (since the number of particles at given p_t drops rapidly for higher p_t values) and are also useful for relating quadrupole amplitudes to conventional $v_2(p_t)$ data.

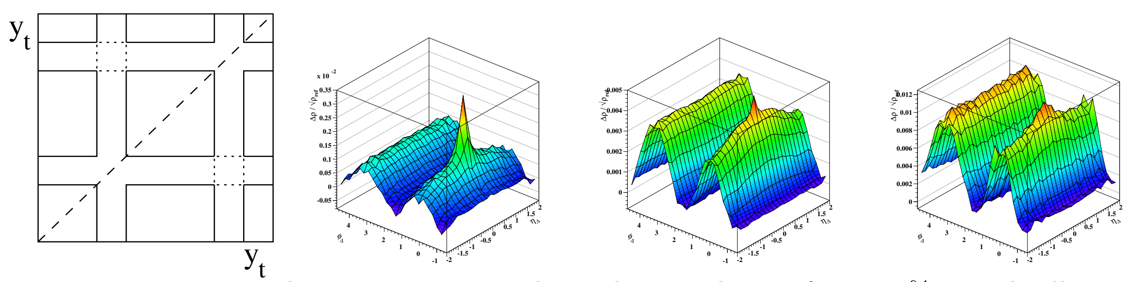

Figure 6.5-1. Marginal y_t cut space, example number correlations for 30-40% central collisions for $y_t < 1.4$, $2.2 < y_t < 2.6$, and $3.4 < y_t < 3.8$.

For cuts made on transverse rapidity y_t and for unidentified particles (hadrons) the pion mass is assumed and $y_t = \ln\{(p_t + m_t)\}/m_\pi$. y_t scales as $\ln(p_t)$ for larger p_t values but remains well defined for $p_t = 0$ and can therefore be used over the entire kinematic range of particles produced at RHIC. There are nine marginal y_t bins corresponding to $y_t < 1.4$ and evenly spaced increments of 0.4 up to $y_t > 4.2$, which corresponds to $p_t \sim 5$ GeV.

Different components of 2D histograms are isolated by fitting them with a model function. Principal structures are a 2D same-side Gaussian peak, a negative dipole component $\cos(\phi_\Delta)$, and a quadrupole component $\cos(2\phi_\Delta)$. For certain p_t ranges and centralities it is desirable to model the away-side azimuth structure with both dipole and 1D Gaussian.

Studying both 62 and 200 GeV collisions for eleven centrality and ten (nine marginal plus y_t-integrated) y_t bins requires 220 histograms. Probing alternative fitting models increases the required number. To avoid traps in local minima we seed the fitting algorithm with random starting points in the allowed parameter space and repeat the fit for each histogram 1000 times. The fit for global-minimum χ^2 is adopted and the distribution of χ^2 values provides a check on the fit stability.

6.6 Quadrupole component marginal p_t dependence

D. T. Kettler and T. A. Trainor

Measurements of the azimuthal quadrupole moment, conventionally denoted by v_2 and attributed to the hydro phenomenon "elliptic flow," have been one of the major results at RHIC. Although there is a large variety of techniques used to measure v_2, most of them either do not distinguish reliably between so-called flow and nonflow effects or do so in physical-model-dependent ways. Previously we described a method which makes use of 2D angular autocorrelations to accurately and effectively measure the azimuth quadrupole even in the presence of large nonflow terms (jet contributions). We extract v_2 values from the quadrupole term of two-particle correlation histograms described in the previous section.

Correlation amplitudes are extracted from pair ratio $\Delta\rho/\rho_{\rm ref}$ normalized by a reference histogram constructed from mixed pairs (particles from different events). For this correlation measure the quadrupole amplitude is equal to $2v_2^2$. Quadrupole amplitudes from fits to marginal distributions of 2D angular correlations for 62 and 200 GeV Au-Au data at several centralities are shown in the left two panels of Fig. 6.6-1.

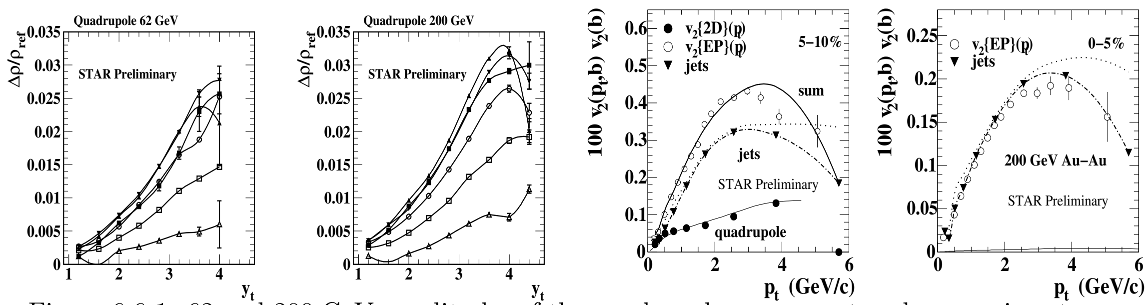

Figure 6.6-1. 62 and 200 GeV amplitudes of the quadrupole component and comparison to 200 GeV event-plane v_2 for 5-10% and 0-5% central collisions

Most published two-particle v_2 data are based on the second coefficient of a simple Fourier decomposition of a two-particle correlation, including the standard event-plane (EP) method within STAR's TPC acceptance. The EP method—though conventionally described with different language—can be shown to be approximately equivalent (within 5%) to the more-direct two-particle correlation method. In some published data there may also be a significant contribution from non-Fourier terms distinguishable by their dependence on the η_Δ axis, specifically the 2D Gaussian peak in our fit model.

Based on measured amplitudes and widths of the 2D Gaussian (jet) component we can calculate directly the jet contribution to the second Fourier component (v_2). This was done in the right two panels of Fig. 6.6-1 for 5-10% and 0-5% central Au-Au collisions: the curve labelled "jets". For 5-10% central collisions the jet contribution is added to the measured quadrupole amplitude to give the "sum" curve that described published $v_2\{EP\}$ data very well. For 0-5% central collisions we cannot reliably measure a nonzero quadrupole term. An estimate of an upper limit is plotted as the lower solid curve. The $v_2\{EP\}$ data are well-described by the jet curve alone. This demonstrates that what is often considered to be "elliptic flow" in the most central collisions is in fact dominated by the Gaussian jet peak.

6.7 Quadrupole spectrum and universality

D. T. Kettler and T. A. Trainor

Consider the single-particle density of particles on azimuth angle ϕ with transverse-rapidity y_t and centrality b dependence, $\rho(y_t, \phi, b)$. It is possible to write it as the sum of two terms $\rho(y_t, \phi, b) = \rho_0(y_t, b) + \rho_2(y_t, \phi, b)$, where ρ_0 is the usual single-particle spectrum and ρ_2 is the azimuth modulation of the spectrum that integrates to zero in ϕ. If $\rho_2(y_t, \phi, b)$ has simple $cos(2(\phi - \psi_R))$ dependence on ϕ we define $\rho_2(y_t, b)$ to be its amplitude. We will then identify $\rho_2(y_t, b)$ as the quadrupole spectrum.

The quadrupole spectrum is difficult to isolate experimentally, however if we invoke a blast-wave model

$$V_2(y_t, b) \approx \frac{p_t \Delta y_{t2}(b)}{2T_2} \rho_2(y_t, b),$$

where $V_2(y_t, b) \equiv \rho_0(y_t, b) v_2(y_t, b)$, $\Delta y_{t2}(b)$ is the quadrupole-dependent boost, and T_2 is a parameter of the model. Then we notice that if we divide by p_t and construct a unit-normal quantity

$$Q(y_t, b) \equiv \frac{V_2(y_t, b)/p_t}{V_2(b)\langle 1/p_t \rangle} \approx \frac{\rho_2(y_t, b)}{\rho_2},$$

which is the ratio of $V_2(y_t, b)/p_t$ to its p_t-integral. Up until now the quadrupole spectrum has been a largely theoretical construction but the quantities that define Q are all experimentally measurable and the model-dependent terms drop out in the ratio, except for the quadrupole spectrum itself. Q for 200 GeV collisions is plotted on the left in Fig. 6.7-1 below for several centralities.

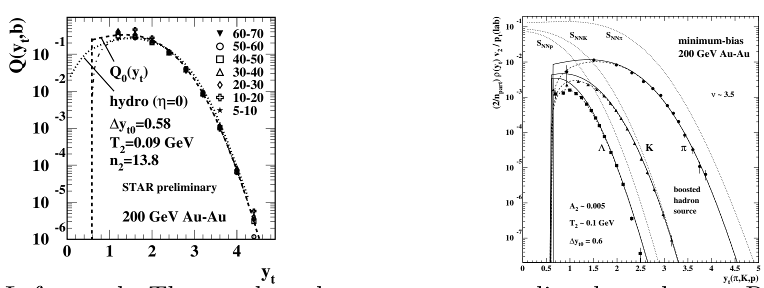

Figure 6.7-1. Left panel: The quadrupole spectrum centrality dependence. Right panel: The quadrupole spectrum for different particle species.

The universal scaling behavior when plotted in this form is remarkable. All centralities seem to exhibit the same form, though there are some deviations for the most central cases at low-p_t. There is a common boost $\Delta y_{t0} = 0.58$ and the data are described by a Lévy distribution with parameters $T_2 = 0.09$ GeV and $n_2 = 13.8$.

Similar behavior has been observed based on published data for minimum-bias identified particle v_2, as seen on the right in Fig. 6.7-1 plotted against proper y_t for each particle species. The different particle species have different y_t-dependence, but there is still a common functional form and the same common Δy_{t0} boost. The boost is a single, sharp value which contradicts flow models that depend on Hubble expansion, which would result in a range of boosts.

6.8 Gaussian jet peak marginal p_t dependence

D. T. Kettler and T. A. Trainor

2D angular correlations in the form of *pair ratios* include a same-side (SS) jet peak modeled by a 2D Gaussian of the form

$$\frac{\Delta\rho_{SS}}{\rho_{ref}} = j^2(\eta_\Delta, \phi_\Delta, b) = A_{2D} \exp\left(-\eta_\Delta^2/2\sigma_\eta^2\right) \exp\left(-\phi_\Delta^2/2\sigma_\phi^2\right). \quad (1)$$

The 2D Gaussian peak centered at $(0,0)$ is a major contributing term to correlations at all observed centralities and p_t. In studies of quadrupole (v_2) systematics it is often disregarded as 'nonflow', however it has very interesting properties of its own. Previous studies of the centrality dependence of this peak in p_t-*integral* form have shown jet-like systematics that are identical to p-p collisions for the more peripheral Au-Au collisions and scale with the number of binary collisions up to a transition point. Above the transition the amplitude increases beyond binary collision scaling and the width on pseudorapidity η also grows quite large.

p_t-*differential* correlations are measured by introducing cuts onto the pair space (y_t, y_t) or a single p_t or y_t variable. Correlation projections onto a single momentum variable result in *marginal* distributions on p_t or y_t. In the present study y_t is divided into nine equal bins (spanning $p_t \in [0.15, 7]$ GeV/c). With marginal p_t distributions we can study the p_t dependence of the SS jet peak as well. Measured $\Delta\rho/\rho_{\rm ref}$ amplitudes and widths in η are plotted in Fig. 6.8-1. Widths in ϕ have also been measured but follow the basic expected trend of narrowing at larger p_t and lack significant centrality dependence, so they have been omitted.

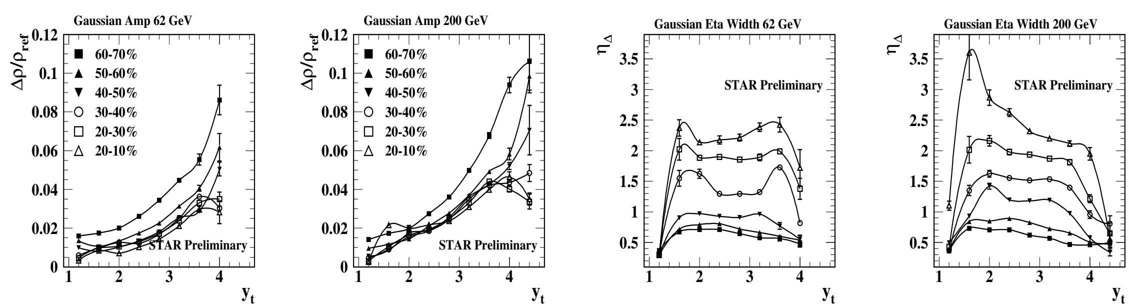

Figure 6.8-1. 62 and 200 GeV amplitudes and widths in η of the Gaussian jet peak.

It is immediately remarkable how the large η width above the transition point (third panel) persists even at large p_t/y_t. In fact, its y_t-dependence is roughly flat over a large y_t interval for all centralities above the transition point. The naive (pQCD) expectation is that the peak should narrow in both η and ϕ as hadron p_t increases if the SS peak is describing correlations between fragments from higher-energy partons. While the mechanism behind this η broadening is not well understood, it is possible to develop a correspondence between the p_t-dependent Gaussian peak and so-called hard components of single-particle spectra, which is the subject of a different article.

6.9 Parametrization of quadrupole centrality and p_t/y_t dependence

D. T. Kettler and T. A. Trainor

Marginal (on y_t, y_t) 2D pair-ratio histograms $\Delta\rho/\rho_{ref}(y_t, b)$ were obtained for 11 centrality bins from 62 and 200 GeV Au-Au collisions. Model fits were used to extract quadrupole amplitudes in the form $v_2^2\{2D\}(y_t, b)$. Factorization was assumed to obtain $v_2\{2D\}(y_t, b)$ via $v_2^2\{2D\}(y_t, b) \to v_2\{2D\}(y_t, b)\, v_2\{2D\}(b)$, where y_t-integral $v_2\{2D\}(b)$ has been previously measured. Two models of the away-side (AS) peak on azimuth (back-to-back jets) were used. Solid points refer to an AS Gaussian (preferred for peripheral collisions), open circles to an AS dipole, (preferred for central collisions). Differences estimate the systematic uncertainty.

We seek to parameterize $v_2\{2D\}(y_t, b)$ on centrality b and p_t/y_t, with transverse momentum $p_t = m_\pi \sinh(y_t)$. From previous analysis we expect a factor p_t and an approximately exponential factor representing the ratio of quadrupole spectrum to single-particle spectrum. After experimentation we divide $v_2\{2D\}(y_t, b)$ by $p_t \exp(-p_t/4)$ to obtain plots in Fig. 6.9-1 (first panel). We find that above $p_t \sim 0.75$ GeV ($y_t \sim 2.3$) the ratio is nearly constant.

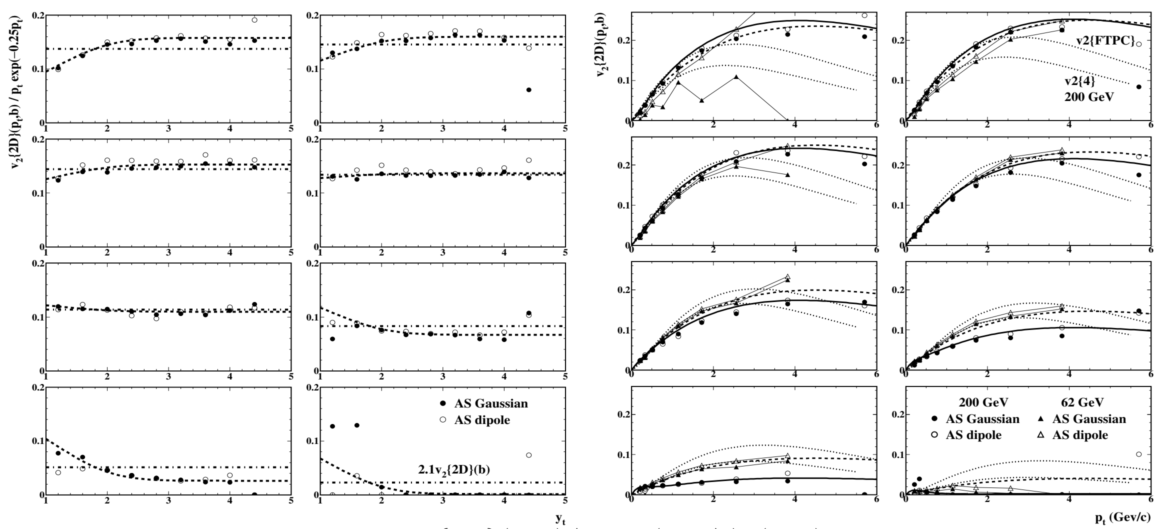

Figure 6.9-1. First: Ratio $v_2\{2D\}(p_t, b)/p_t \exp(-p_t/4) f(p_t, b) \sim$ constant, Second: $v_2\{2D\}(p_t, b)$ for 62 and 200 GeV Au-Au collisions with parametrizations.

A full parametrization of the 200 GeV data is given by

$$\begin{aligned} v_2\{2D\}(p_t, b) &= 2.1\, v_2\{2D\}(b)\, p_t \exp(-p_t/4) f(p_t, b) \\ f(p_t, b) &= 1 + C(b)\, [\mathrm{erf}(y_t - 1.2) - \mathrm{erf}(1.8 - 1.2)] \\ C(b) &= 0.12 - (\nu - 3.4)/5 - [(\nu - 3.4)/2]^2. \end{aligned} \tag{1}$$

Factor $f(y_t, b) \sim 1$ accommodates deviations from a constant value below $p_t \sim 0.75$ GeV/c. The 62 GeV data exhibit similar trends with quantitative differences. Fig. 6.9-1 (second panel) shows the 62 and 200 GeV $v_2\{2D\}(p_t, b)$ data with parametrizations (solid and dashed curves). The dotted curves show published $v_2(p_t)$ data derived from nongraphical numerical methods, with large discrepancies. This analysis shows that full factorization of centrality and p_t/y_t dependence is possible, with implications for hydro interpretations of v_2 data.

6.10 Mean jet correlations in a finite angular acceptance

T. A. Trainor

2D angular autocorrelations include a 2D *same-side* (SS) peak modeled as a 2D Gaussian. Angular correlations are reported in the *per-particle* form, with SS peak component

$$\frac{\Delta\rho_{SS}}{\sqrt{\rho_{ref}}} = \rho_0(b)\, j^2(\eta_\Delta, \phi_\Delta, b) = A_{2D}\, \exp\left(-\eta_\Delta^2/2\sigma_\eta^2\right)\, \exp\left(-\phi_\Delta^2/2\sigma_\phi^2\right).$$

The SS 2D peak is interpreted by hypothesis as representing a minimum-bias ensemble of jets and should then include all hadron pairs from all jets that survive partonic and hadronic rescattering, averaged over selected nuclear collisions. We want to infer the corresponding parton fragment (jet hadron) number from fragment pair correlations. To do so we need the *angle-averaged* integral of the SS peak within the angular acceptance.

Fig. 6.10-1 (first panel) shows an example histogram for one of eleven collision-centrality bins from 200 GeV Au-Au collisions. The main features are an elongated SS 2D peak ($\phi_\Delta = \phi_1 - \phi_2 = 0$), and away-side (AS) ridge ($\phi_\Delta = \pi$) uniform on η_Δ (η is pseudorapidity).

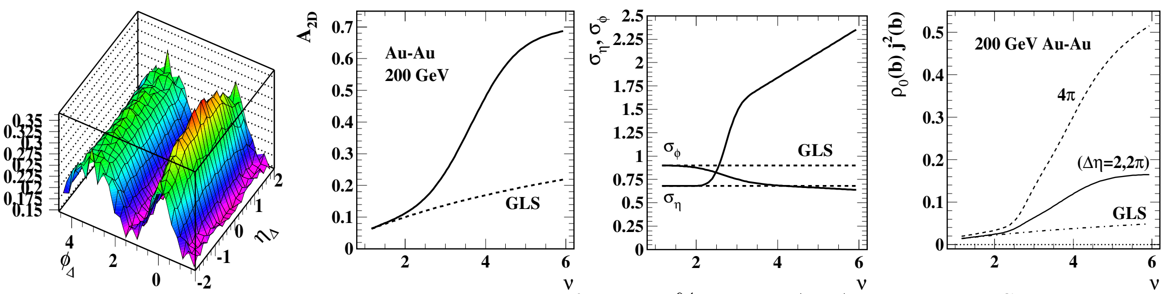

Figure 6.10-1. First: 2D angular correlations for 10-20% central Au-Au collisions. Second: Amplitude of the 2D SS jet peak. Third: rms widths of the 2D SS jet peak. Fourth: Angle-averaged SS pair yield. $\rho_0(b)$ is the single-particle density on (η, ϕ) for centrality b.

Fig. 6.10-1 (second and third panels) shows smooth parametrizations of p_t-integral data[1] for 2D peak amplitude A_{2D}, and η and ϕ widths from $\sqrt{s_{NN}} = 200$ GeV Au-Au collisions. The data are described to a few percent except for the interval $\nu > 5$ where amplitude and η-width data typically fall below the parametrization. In more-peripheral collisions the parameters follow a *Glauber linear superposition* (GLS) trend (dashed curves). At a particular centrality ($\nu \sim 2.5$) jet characteristics change dramatically, with large increases in amplitude (fragment pair yield) and η width (jet η elongation) relative to the GLS reference.

Figure 1 (fourth panel) shows the angle-averaged parton-fragment pair yield (SS jet peak) in the form $\rho_0(b)\, j^2(b)$ for fragment pairs within the angular acceptance (solid curve) and also extrapolated to 4π (dashed curve). The dash-dotted curve shows the GLS reference. The difference between the 4π and $(\Delta\eta = 2, 2\pi)$ curves is large for this pair measure because the pair acceptance depends on the square of the relative η acceptance $\Delta\eta/\Delta\eta_{4\pi}$. The curve labeled 4π can be obtained from the SS 2D peak "volume" V in the cited reference as $V/4\pi$.

[1] M. J. Daugherity, (STAR Collaboration), J. Phys. G **35**, 104090 (2008).

6.11 Jet properties inferred from jet angular correlations

D. T. Kettler and T. A. Trainor

In order to infer parton fragment numbers from jet angular correlations we need to calculate the mean jet number $n_j(b)$ in the angular acceptance. The frequency of jets per unit η per N-N binary collision in A-A collisions is defined by

$$f(b) \equiv \frac{1}{n_{bin}(b)} \frac{dn_j(b)}{d\eta} = \frac{\epsilon_j(b)\, \sigma_{dijet}(b)}{\sigma_{NSD} \Delta\eta_{4\pi}(b)}, \tag{1}$$

where $\epsilon_j(\Delta\eta, \Delta\eta_{4\pi}) \in [1, 2]$ is the mean number of jets per dijet within η acceptance $\Delta\eta \leq \Delta\eta_{4\pi}(b)$, and $\Delta\eta_{4\pi}(b)$ is the *effective* 4π acceptance assuming uniform jet density $dn_j/d\eta$. $\sigma_{NSD} = 36.5$ mb is the total cross section for non-single-diffractive (NSD) N-N collisions. n_{bin} is the mean number of N-N binary collisions per A-A collision. $\sigma_{dijet}(b)$ is determined by the parton spectrum cutoff inferred from hadron spectrum hard components.

In Fig. 6.11-1 (first panel) the number of jets per dijet within acceptance $\Delta\eta$ is $\epsilon_j(\Delta\eta) = 1/(1-a/2)$, with fractional η acceptance $a = \Delta\eta/\Delta\eta_{4\pi}$. In Fig. 6.11-1 (second panel) the solid curve estimates the centrality variation of jet frequency $f(b)$ for 200 GeV Au-Au collisions. The single point is taken from an analysis of p_t spectra from 200 GeV NSD p-p collisions.

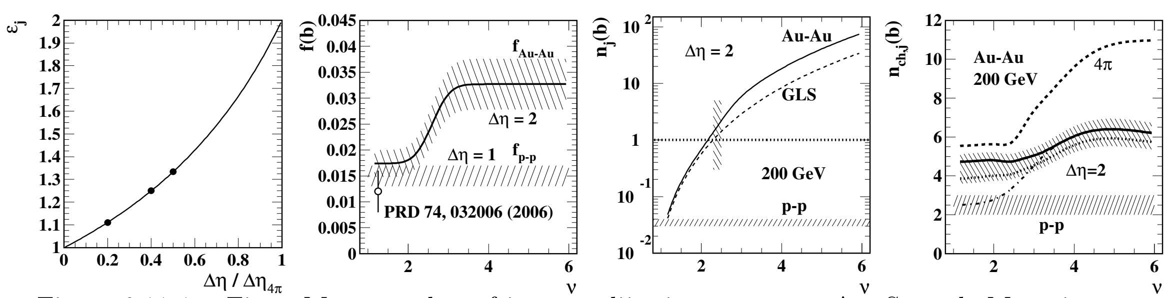

Figure 6.11-1. First: Mean number of jets per dijet in acceptance $\Delta\eta$, Second: Mean jet frequency per unit η per N-N collision, Third: Mean number of jets in angular acceptance $(\Delta\eta, 2\pi)$, Fourth: Mean jet multiplicity as a function of centrality in Au-Au collisions.

We now combine estimated jet frequencies with measured jet angular correlations to infer mean jet multiplicities. The rms minimum-bias jet multiplicity is obtained by introducing the $n_j(b)$ hypothesis to obtain

$$n_j(b)\, n^2_{ch,j}(b) = n^2_{ch}(b) j^2(b) \rightarrow n_{ch,j}(b) = n_{ch}(b) \sqrt{j^2(b)/n_j(b)}, \tag{2}$$

where $n_{ch}(b) = 2\pi\Delta\eta\, \rho_0(b)$ (multiplicity in the angular acceptance) and $j^2(b)$ are measured quantities. Fig. 6.11-1 (third panel) shows the number of jets $n_j(b) = \Delta\eta\, n_{bin}\, f(b)$ in $\Delta\eta = 2$ for 200 GeV Au-Au collisions (solid curve) and the corresponding GLS reference (dashed curve) representing binary-collision scaling of p-p collisions. The horizontal hatched band represents the estimate for p-p collisions. Fig. 6.11-1 (fourth panel) shows rms jet multiplicity $n_{ch,j}(b)$ as a function of Au-Au centrality inferred from Eq. (2). The solid curve is the result within a 2D angular acceptance $(\Delta\eta = 2, 2\pi)$ including edge losses. The dashed curve is the result for a 4π acceptance. The other curves are used to estimate systematic uncertainties.

6.12 Minijet contribution to Au-Au particle production

D. T. Kettler and T. A. Trainor

The per-participant-pair 2D total hadron density

$$\frac{2}{n_{part}}\,\rho_0(b) \quad = \quad S_{NN} + \nu\, H_{AA}(b) \approx \rho_{pp}\,\{1 + x\,(\nu - 1)\}, \tag{1}$$

with $\rho_{p\text{-}p} \approx 0.4$, describes particle production in the two-component model of A-A collisions. We consider the possibility that spectrum hard-component density $H_{AA}(b)$ can be inferred directly from jet angular correlations. $H_{AA}(b)$ is defined as the 2D angular density of parton fragments per N-N binary collision. In that case it should be related to jet angular correlations via jet frequency per N-N collision $f(b) = (1/n_{bin})\, dn_j/d\eta$ and mean jet multiplicity $n_{ch,j}(b)$

$$\nu H_{AA}(b) \quad = \quad \frac{2}{n_{part}}\, n_{ch,j}\,\frac{dn_j}{2\pi d\eta} = \frac{2}{n_{part}}\rho_0(b)\sqrt{n_j(b)\, j^2(b)}, \tag{2}$$

where the third expression is obtained by replacing $n_{ch,j}$ by its equivalent in terms of measured quantities [jet fragment pair ratio $j^2(b)$ and single-particle 2D density $\rho_0(b)$].

Fig. 6.12-1 (first panel) shows the mean 2D charged-particle density at mid-rapidity for Au-Au collisions at $\sqrt{s_{NN}} = 200$ GeV as a function of centrality defined by the last expression in Eq. (1) with $x = 0.09$. $\rho_0(b)$ is needed to convert two-particle correlations to jet yields. Fig. 6.12-1 (second panel) shows $2\pi H_{AA}(b)$ inferred from jet angular correlations via Eq. (2) for finite η acceptance and jet edge losses (solid curve) and for 4π acceptance (dashed curve). Generally, a factor 2.5-5 increase in the product of jet frequency times jet fragment multiplicity with Au-Au centrality is indicated by both spectrum and correlation data.

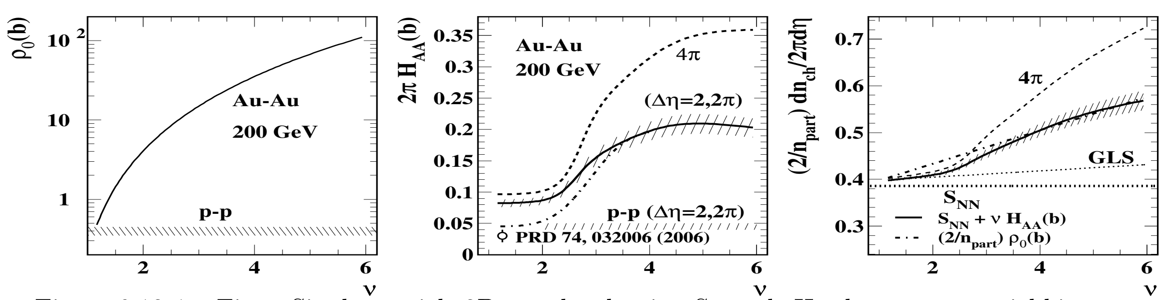

Figure 6.12-1. First: Single-particle 2D angular density, Second: Hard-component yield inferred from jet angular correlations, Third: Comparison of charged-particle densities derived from jet angular correlations and approximate observed single-particle density $\rho_0(b)$.

Substituting $H_{AA}(b)$ from Fig. 6.12-1 (second panel) into Eq. (1) gives the solid curve in the third panel. Those results can be compared with the second two-component expression in Eq. (1) with $x = 0.09$ (dash-dotted line) approximating the measured total charged-particle yield. The good agreement for more-central collisions suggests that at least a majority of the additional particle production beyond participant scaling (S_{NN},N-N soft Pomeron exchange and projectile-nucleon fragmentation) can be attributed to correlated hadrons associated with (mini)jets appearing as fragment pairs in the SS jet peak of 2D angular correlations.

6.13 Extracting single-particle fragment spectra from jet correlations

T. A. Trainor

Large-angle-scattered partons (mainly gluons) produce copious correlated hadron pairs in the final state of A-A collisions at RHIC. We want to infer single-particle fragment spectra on transverse rapidity $y_t = \ln[(m_t + p_t)/m_\pi]$ from the marginal distribution of 2D jet angular correlations. Fragment spectra are obtained by a factorization procedure. They can be compared with pQCD predictions of minimum-bias fragment distributions and with *hard components* extracted from single-particle hadron spectra. The starting point of the analysis is a set of measured *pair-ratio* histograms $\Delta\rho/\rho_{ref}(\eta_\Delta, \phi_\Delta)$ for some conditions (cuts) on (y_t, y_t) (total integral, joint or marginal distribution) and centrality b. Marginal distributions (projections) are obtained by integrating over one y_t variable of (y_t, y_t). Model fits are used to extract same-side (SS) jet peak distribution $j^2(y_t, \eta_\Delta, \phi_\Delta, b)$ from 2D angular correlations:

$$j^2(y_t, \eta_\Delta, \phi_\Delta, b) = A_{2D}\, \exp\{-\eta_\Delta^2/2\sigma_{\eta_\Delta}^2\}\, \exp\{-\phi_\Delta^2/2\sigma_{\phi_\Delta}^2\}, \tag{1}$$

where SS peak parameters A_{2D}, σ_{η_Δ} and σ_{ϕ_Δ} depend on transverse rapidity y_t and A-A centrality b. The model function may extend beyond the actual pair η acceptance. In what follows fragment-pair and fragment numbers are those observed within the angular acceptance.

6.13.1 pQCD jet fragment distributions

We first introduce the pQCD context for parton fragmentation. A single-particle parton *fragment distribution* (FD) for scattered partons on transverse rapidity y_t can be defined for individual non-single-diffractive (NSD) N-N collisions by a pQCD folding integral, including fragmentation function ensemble $D(y_t, y_{max}, b)$ and dijet (parton) spectrum $d\sigma_{dijet}/dy_{max}$:

$$\begin{aligned} FD(y_t, b) = \frac{d^2 n_f}{dy_t\, d\eta} &= \frac{\epsilon_j(\Delta\eta)/2}{\sigma_{NSD}\, \Delta\eta_{4\pi}} \int_0^\infty dy_{max}\, D(y_t, y_{max}, b)\, \frac{d\sigma_{dijet}}{dy_{max}} \\ &= f(b)\, D(y_t, b)/2, \end{aligned} \tag{2}$$

where $y_{max} = \ln(2E_{jet}/m_\pi)$ is the parton rapidity, $f(b) = (1/n_{bin}) dn_j(b)/d\eta$ is the jet frequency per unit η per N-N binary collision, and $D(y_t, b) = 2dn_{ch,j}(y_t, b)/dy_t$ is the mean dijet fragmentation function averaged over the minimum-bias parton spectrum.

6.13.2 Factorization of pair distribution

To obtain a single-particle fragment spectrum from jet correlations we must factorize the pair distribution in the SS peak. Factorization is valid only for y_t-integrated and angle-averaged pair distributions. The 5D fragment-pair density is expressed in terms of pair ratio $j^2(y_t, b)$

$$J^2(y_t, b) = \rho_0(b)\, \rho_0(y_t, b)\, j^2(y_t, b), \tag{3}$$

where $j^2(y_t, b)$ is the average number of fragment pairs per particle pair in the angular acceptance for conditions (y_t, b), 3D $\rho_0(y_t, b)$ is the single-particle y_t spectrum, and 2D $\rho_0(b)$ is its integral on y_t. To factorize we must estimate the number of pairs per jet using pQCD estimate $n_j(b)$, the mean number of jets in the acceptance for given A-A centrality. $j(y_t, b)$ is the number of jet fragments per charged hadron which we want to infer from jet correlations.

Only the y_t-integrated angle-averaged pair ratio $j^2(b)$ can be factorized. By demanding self-consistency among all integrals on y_t we obtain relations between single-particle ratios j and pair ratios j^2

$$\begin{aligned} n_j(b) j^2(b) &= [j(b)]^2 \\ j(y_t, b) &= n_j(b)\, j^2(y_t, b)/j(b) \\ &= \sqrt{\frac{n_j(b)}{j^2(b)}}\, j^2(y_t, b). \end{aligned} \tag{4}$$

$j(y_t, b)$ is then the differential (on y_t) fragment ratio in the acceptance, $j^2(b)$ and $j^2(y_t, b)$ are measured quantities, and $n_j(b)$ is estimated via pQCD calculation. The 3D angle-averaged fragment density is

$$\begin{aligned} J(y_t, b) &= \rho_0(y_t, b)\, j(y_t, b) \\ &\equiv \frac{n_j(b)}{2\pi\Delta\eta} \frac{1}{y_t} \frac{dn_{ch,j}}{dy_t} \\ &= \frac{n_{bin}}{2\pi} f(b) \frac{1}{y_t} \frac{dn_{ch,j}}{dy_t} \end{aligned} \tag{5}$$

6.13.3 Connecting jet correlations to spectrum hard components and pQCD

Fragment density $J(y_t, b)$ can be related directly to spectrum hard component $H_{AA}(y_t, b)$. The latter has in turn been compared directly to pQCD *fragment distributions* (FDs). It should be possible therefore to establish a quantitative connection between intra-jet correlations (SS jet peak) and pQCD via single-particle spectrum hard components.

$J(y_t, b)$ is the single-particle fragment distribution on y_t derived from SS jet correlations within $\Delta\eta$, the 3D y_t spectrum of jet fragments within acceptance $\Delta\eta$. We can make the transition $J \to H$ to connect jet correlations J^2 with spectrum hard components H. The 2D jet fragment density per binary N-N collision is

$$\begin{aligned} \frac{2\pi}{n_{bin}} J(y_t, b) &= f(b) \frac{1}{y_t} \frac{dn_{ch,j}(y_t, b)}{dy_t} \leftrightarrow \frac{1}{y_t} FD(y_t, b) \\ 2\pi H_{AA}(y_t, b) &= \frac{1}{y_t} \frac{d^2 n_h(y_t, b)}{dy_t\, d\eta} \end{aligned} \tag{6}$$

which can be compared to (FDs). The comparison tests the hypothesis that the integral of the SS jet peak compares directly to the y_t spectrum hard component, and therefore to pQCD predictions for parton fragmentation in nuclear collisions.

6.14 Marginal distributions of jet angular correlations on y_t

D. T. Kettler and T. A. Trainor

2D angular autocorrelations on pseudorapidity and azimuth difference variables $(\eta_\Delta, \phi_\Delta)$ provide information on jet production in nuclear collisions. Jet angular correlations depend on cuts in the complementary pair space (y_t, y_t) where transverse rapidity $y_t = \ln\{(m_t+p_t)/m_\pi\}$, p_t is transverse momentum and m_t is transverse mass. p_t- or y_t-integral jet angular correlations have been extensively studied. We have recently extended jet studies to dependence of jet correlations on restricted parts of (y_t, y_t) space. Fig. 6.14-1 (first panel) shows that space with two types of cuts. The corresponding p_t range is [0.15,7] GeV/c. The bold square boxes are bins in a joint distribution on (y_t, y_t). The crossed rectangles (for the present analysis) are bins in a *marginal* distribution, a projection of the joint distribution onto y_t.

The same-side (SS) jet peak, by hypothesis including all *intra*jet correlated fragment pairs, is represented by pair ratio $j^2(y_t, \eta_\Delta, \phi_\Delta, b)$ (fragment pairs divided by mixed or reference pairs) and modeled by a 2D Gaussian with amplitude A_{2D} and rms widths σ_η and σ_ϕ, all depending on transverse rapidity and Au-Au centrality (y_t, b). Model-fit results for six (of eleven) centrality classes of 200 GeV Au-Au collisions and nine y_t bins are shown in Fig. 6.14-1. Of those centralities the solid dots are most peripheral, the open squares are most central.

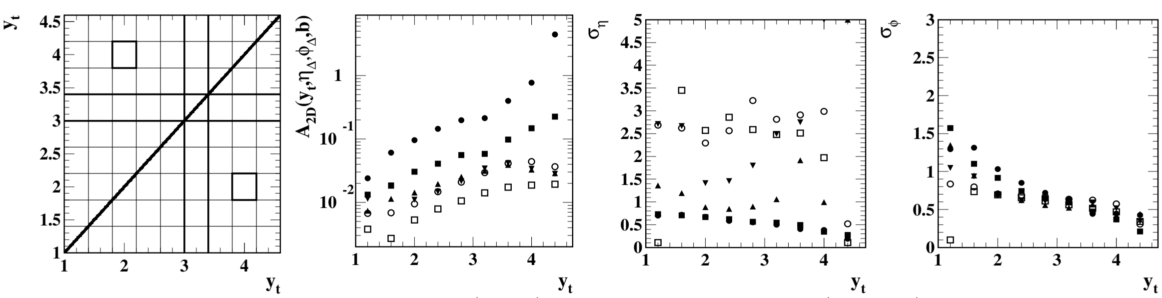

Figure 6.14-1. First: Cut space on (y_t, y_t) showing bins for joint (squares) and marginal (rectangles) distributions, Second: 2D same-side jet peak amplitude, Third: Pseudorapidity peak width σ_η, Fourth: Azimuth peak width σ_ϕ.

Fig. 6.14-1 (second panel) shows the 2D Gaussian amplitudes, which are largest for the most peripheral Au-Au collisions and the largest y_t. Because $j^2(y_t, \eta_\Delta, \phi_\Delta, b)$ is a *pair ratio* the data include a trivial factor $1/n_{ch}(y_t, b)$ (the y_t spectrum) which dominates the observed trends. In an accompanying article the data are transformed to reveal jet evolution vs (y_t, b).

Fig. 6.14-1 (third and fourth panels) show the rms widths of the 2D jet peak. What is expected in a pQCD scenario is a symmetric 2D jet peak (equal rms widths) narrowing with increasing p_t/y_t. In Au-Au collisions those expectations are dramatically contradicted. The η width increases by 3-4$\times$ with Au-Au centrality above a *sharp transition.* The greatly-increased η width is found in this study to be nearly constant on y_t until $y_t \sim 4.5$ ($p_t \sim$ 6 GeV/c) where it falls back to the pQCD expectation. Azimuth width σ_ϕ by contrast is twice as large as σ_η in peripheral (and p-p) collisions at smaller y_t but narrows to the pQCD expectation with increasing centrality and y_t. Those results provide new detailed information on in-medium modification of jets in more-central Au-Au collisions.

6.15 Marginal jet correlations versus spectrum hard components and pQCD

D. T. Kettler and <u>T. A. Trainor</u>

From marginal jet angular correlations (same-side 2D jet peak) in the form of pair ratios $j^2(y_t, \eta_\Delta, \phi_\Delta, b)$ we wish to obtain corresponding single-particle fragment spectra $J(y_t, b)$ (3D densities). We combine pQCD jet frequency $f(b) = (1/n_{bin})\, dn_j(b) d\eta$ or jet number $n_j(b) = n_{bin}\Delta\eta f(b)$ within $(\Delta\eta, 2\pi)$ and angle averaging of the 2D jet peak to obtain $\rho_0(b)\, j^2(y_t, b)$ in Fig. 6.15-1 (first panel). The solid points represent the most peripheral data, the open circles represent the most central of the six plotted (of eleven total) centrality bins. The monotonic but uneven increase in amplitude with increasing centrality is consistent with an observed “sharp transition” in jet characteristics (same-side peak amplitude, η width) on centrality.

Incorporating y_t-integrated fragment pair ratio $j^2(b)$ the 3D parton fragment spectrum is

$$\begin{aligned} J(y_t, b) &= \sqrt{\frac{n_j(b)}{j^2(b)}}\, \rho_0(y_t, b)\, j^2(y_t, b) \equiv \frac{n_j(b)}{2\pi\Delta\eta} \frac{1}{y_t} \frac{dn_{ch,j}}{dy_t} \qquad (1) \\ \frac{2\pi}{n_{bin}} J(y_t, b) &= f(b) \frac{1}{y_t} \frac{dn_{ch,j}}{dy_t}, \end{aligned}$$

the 2D fragment density on (y_t, η) per N-N binary collision. $(1/y_t) dn_{ch,j}/dy_t$ is the per-jet mean fragment spectrum. Its integral on y_t is mean jet multiplicity $n_{ch,j}$. Fig. 6.15-1 (second panel) shows $(2\pi/n_{bin})J(y_t, b)$ for six centralities of 200 GeV Au-Au collisions compared to a Gaussian model of the spectrum hard component from 200 GeV p-p collisions (dashed curve).

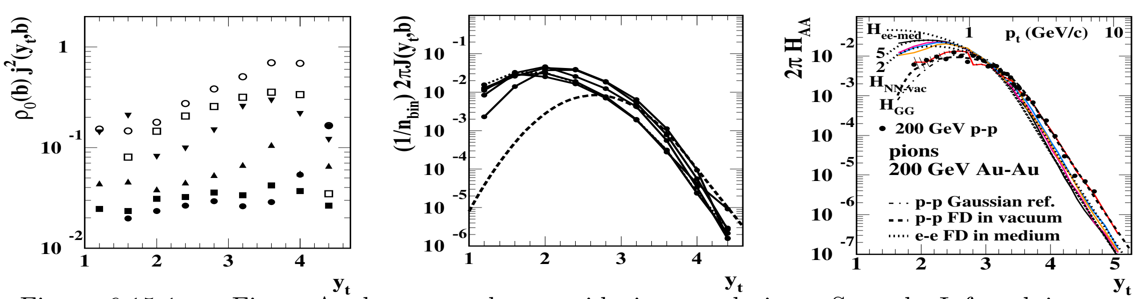

Figure 6.15-1. First: Angle averaged same-side jet correlations, Second: Inferred jet fragment spectra, Third: Spectrum hard components and pQCD fragment distributions.

The parton fragment spectra inferred from jet angular correlations can be compared with single-particle spectrum hard components extracted via a *two-component* spectrum model. Fig. 6.15-1 (third panel) shows spectrum hard components obtained from p-p and Au-Au collisions and pQCD calculations of corresponding fragment distributions (FDs). Although the results in the second panel are very preliminary we see already semiquantitative agreement between the jet correlation results and other manifestations of parton fragmentation.

We have brought together single-particle spectrum hard components, pQCD calculations of fragment distributions and fragment spectra inferred from jet angular correlations. We find that different manifestations of (by hypothesis) parton fragmentation in the final state are compatible with pQCD theory, even in central Au-Au collisions, thus buttressing interpretation of specific correlation and spectrum structure in terms of (mini)jets.

6.16 Status of the DWEF model for the analysis of pion interferometry

J. G. Cramer and G. A. Miller*

The work on this project is essentially completed. Our last publication[1] summarized our work on the DWEF model and discussed the discovery of a new term in the formalism involving pion emission from eliminated states, an additional contribution that must be included in the predictions if the optical potential is complex. In the past year we have investigated this problem further, but we have found no way of precisely evaluating this extra term. The presence of this unevaluated term limits the applicability and reliability of the DWEF model.

We note, however, that our previous work indicated the presence of an initial temperature in the collisions that was high enough to produce chiral symmetry restoration. Recent observations at RHIC of gamma rays from the initial collision stages[2] confirm that temperatures of the scale that would produce chiral symmetry restoration are indeed present in Au+Au collisons at $\sqrt{s_{NN}} = 200$ Gev.

*Supported by the UW Nuclear Theory DOE Contract

[1] "Understanding the Optical Potential in HBT Interferometry", Matthew Luzum, John G. Cramer, and Gerald A. Miller, (2008) Phys. Rev. C78:054905.

[2] "Detailed measurement of the e^+e^- pair continuum in p + p and Au + Au collisions at $\sqrt{s_{NN}} = 200$ Gev and implications for direct photon production", A. Adare, et al., arXiv: 0912.0244

7 Computing, and Electronics

7.1 Laboratory computer systems

R. C. Coffey*, G. T. Holman, M. A. Howe†, R. J. Seymour, H. E. Swanson,
N. R. Tolich, J. F. Wilkerson†, and D. I. Will

We are a mixed shop of Windows 7, XP, Vista, Mac OS X and various flavors of Linux. Windows 7 is installed on new systems, but we are still running Windows XP, Pro, and Vista. The predominant Linux distribution for servers is Fedora with a couple of exceptions. This year we added a DocDB document server on a dedicated Ubuntu server platform and moved the EWI server duties to an Apple Mac mini. We have three shared-usage Fedora-based systems, one of which hosts our 6.5 TB RAID farm. Linux and Windows backups are saved to the RAID farm, from whence they are written to LTO tape by the Physics Computer Center on a three month backup retention plan. One of the other Fedora hosts is holding a terabyte drive for archival backups.

Our computing and analysis facility consists of:
• The 140-node, 1120-core Athena (see Sec. 7.2) cluster as a shared resource with Physics, the Institute for Nuclear Theory (INT), and the Astronomy department.
• A mix of Linux systems: RedHat v7.3 through v9.0 and Fedora Cores 6 through 12
• One VMS/VAXstation and two VMS Alphas for "legacy" computing.
• The SNO, NCD, KATRIN, Majorana and emiT groups rely upon Macintosh systems.
• One SunBlade 100 workstation serves CADENCE circuit design, analysis and layout duties.
• A VAXstation is the linac and vacuum systems control and display system.
• Various WindowsXP desktop JAM systems (Java based software for acquisition and analysis), plus two laptops for taking to other installations.
• The bulk of CENPA's Windows-based PCs are behind a Gibraltar Linux-based logical firewall using an automated setup procedure developed by Corey Satten, previously of the University's Networks and Distributed Computing group[1].
• Although not directly used by lab personnel, we provide additional legacy co-location services for the INT and the Physics Nuclear Theory group in the form of one VMS Alphastation 500.

Planning is underway to improve the following resources next year:
• Improve current backup strategy by increasing disc space and implementing a backup solution for our heterogenous OS environment.
• Provide a dedicated and structured file server.
• Implement CENPA wiki.
• Consolidate redundant services (group Wiki applications, web and mail servers, etc.).
• Migrate serial/VAX based controllers to TCP/Labview.

---

*UW Physics Department
†Presently at the University of North Carolina
[1]http://staff.washington.edu/corey/fw/

7.2 Athena: a high end computing deployment for scientific computing

R. Coffey, J. Garder, G. T. Holman, D. B. Kaplan, M. L. Miller, T. Quinn, R. J. Seymour, and D. I. Will

Initiated by Co-Investigators D. Kaplan and T. Quinn, Athena[1] is a high end computing (HEC) cluster, hosted at CENPA, for use within Physics, Astronomy, and Computer Science. The cluster supports high performance scientific computing applications that cannot be efficiently executed on typical commodity server infrastructures (e.g., the Amazon EC2 Cloud). The current Athena configuration consists of 140 machines linked together by a high speed InfiniBand network fabric, 1.23 TB of RAM, and 23.7 TB of high rate shared storage. The peak performance of the system is greater than 10 TeraFlops. Access to the computing nodes is controlled via the PBS job submission application. Aside from the raw horsepower mentioned above, the Athena cluster's key differentiating characteristic is the InfiniBand interconnect ($\sim$80 Gbs communication between any two nodes) which radically outpaces the traditional 1 Gbs ethernet connections used in a typical data center, allowing for seamless integration of parallel methods such as MPI into application design and execution.

The cluster has already proven to be an invaluable resource for local researchers. A full list of publications is available online[2]. Notable uses of the cluster include:

- Simulations of the KATRIN detector and backgrounds.
- Simulations of the MAJORANA detector.
- Data analysis and dark matter limit extraction[3].
- Simulations and data analysis of the SNO+ detector.
- Providing the 5x speedup that the SNO collaboration needed to perform an emergency reprocessing of the phase-3 data to meet conference and publication deadlines[4].
- Integrating MPI into an existing C++ application to perform massively parallel analytic calculations of the EM fields in the KATRIN spectrometer.
- Simulations of new detector configurations for the rapidly evolving MAJORANA project.
- Computing the interactions of 2- and 3-baryons using lattice QCD.
- Simulating structure formation in the early universe.
- Searching for systematic patterns in the masses of medium and heavy nuclei.
- Rapid prototyping and benchmarking of existing parallel data management solutions (Hadoop, PIG, etc.) leading to a deadline driven, inter-disciplenary eScience proposal to build a custom Database Management System for HEC applications.

[1]http://librarian.phys.washington.edu/athena/index.php/
[2]http://physoffice.phys.washington.edu/athenapreprint/display/view.aspx
[3]http://www.nature.com/news/2010/100226/full/news.2010.97.html
[4]B. Aharmim *et al.*, Phys. Rev. Letters **101**, 111301 (2008).

7.3 Preamplifier with forward biased reset for MAJORANA

M. L. Miller, D. A. Peterson, R. G. H. Robertson, T. D. Van Wechel, and B. A. Wolfe

A charge sensitive pre-amplifier with continuous reset by the forward biased gate-to-source junction of the input JFET is currently under development for MAJORANA and other projects. Our previous work focused on the development of a pulsed reset pre-amplifier. The pulsed reset pre-amplifier has several disadvantages including complex circuitry for generating the reset, and dead time due to the periodic resets and the associated recovery time after the reset transient.

The key to the forward biased reset pre-amplifier is that the JFET is operated in a different region than is typical. Typically JFETs are biased with the gate reversed biased with respect to the source. The saturation current of a JFET, I_{DSS}, is defined as the drain current with a gate-to-source voltage of 0 volts. When the gate-to-source junction is reverse biased, there is a small reverse leakage current, typically lower than 1 pA for a good JFET. It is not generally well known, but it is actually possible to operate a JFET with the gate source junction slightly forward biased. If the transfer function of gate current versus gate voltage is plotted, there is a point where the gate current is zero, typically about 50 mV forward bias. The JFET will operate at this same point if the gate lead is open, the gate current is zero and the drain current is slightly higher than I_{DSS}, and can be defined as I_{DSO}. As the gate-to-source junction forward bias is increased further, the gate current flows in a forward direction, generally following the same curve as a forward biased diode. The drain current also increases as the forward bias on the gate to source junction increases, basically following the same transfer function as when it was reverse biased.

There are two feedback loops in our forward biased pre-amplifier. The first provides ac feedback and consists of a feedback capacitor between the output of the pre-amplifier and the input, which is the gate of the JFET. In a classical charge sensitive amplifier, the dc feedback is provided by a high value feedback resistor in parallel with the feedback capacitor. In the forward biased pre-amplifier the DC feedback is provided by a second feedback loop that controls the drain current, setting it to the proper value that matches the JFET's transfer function of drain current versus gate current.

The forward biased pre-amplifier has series and parallel noise comparable to a pulse reset pre-amplifier. The shot noise due to the forward biased gate junction carrying the detector leakage current may be larger, depending on the degree of correlation with the intrinsic shot noise of detector leakage current. For reference, if the detector leakage current is 1 pA, then the shot noise would be equivalent to a 50 GΩ feedback resistor of a conventional preamp.

Another issue is that for a JFET with a low I_{DSS}, not more than 5 to 10 mA must be used or the power dissipation will be excessive. We plan to use a special type of JFET, a tetrode JFET manufactured by Moxtek, that has two gates. This JFET has high I_{DSS} and transconductance. The substrate gate is reverse biased and sets the quiescent operating point at approximately 5 mA. The signal gate is physically small and therefore has a relatively small input capacitance while still maintaining a higher than typical transconductance. In this configuration we are operating the signal gate in the forward biased region as described above, but the dc feedback is provided to the substrate gate to maintain the JFET at its proper dc operating point.

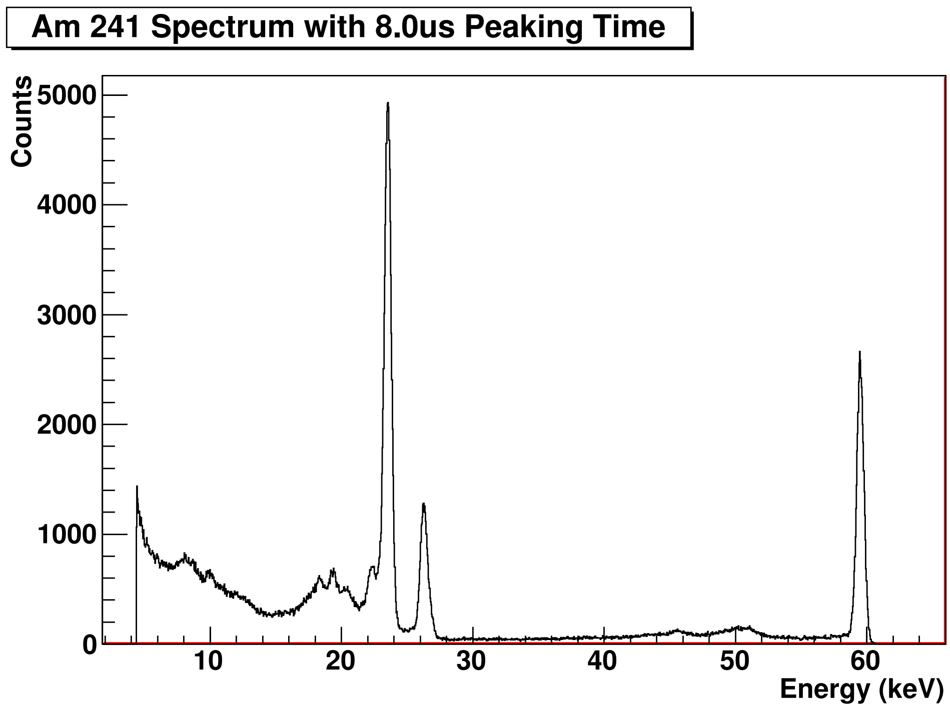

Figure 7.3-1. Spectrum of ^{241}Am with a small Si PIN diode and a prototype forward-biased FET preamp.

Fig. 7.3-1 was taken with the first prototype of the forward biased pre-amplifier cooled to -50° C with dry ice, at a peaking time of 8 μs. The measurement was made with a low cost Hamamatsu S3096-02 photodiode biased at 60 volts and a ^{241}Am source. The photodiode has approximately 3 pF capacitance and a leakage current of around 50 pA. The first prototype has a Moxtek MX-120 FET in a TO-72 package. Dielectric loss in the header of the TO-72 package and also the dielectric loss of the printed circuit board limit the resolution in this version. The measured resolution was 670 eV FWHM for the Si detector, or 550 eV FWHM converted to Ge. The final design will use bare dice bonded to a fused silica substrate.

7.4 Electronic equipment

A. W. Myers*, D. A. Peterson, and T. D. Van Wechel

The electronics shop is responsible for the design and construction of new laboratory electronic equipment, as well as the maintenance and repair of existing CENPA electronics. Projects undertaken by the electronics shop included the following:

1. The development of a forward biased reset pre-amplifier (see Sec. 7.3) for the MAJORANA experiment has been the most significant design project this year. The design has been completed and the initial prototype is now being tested.
2. A spare PULCINELLA femtoammeter board was constructed for the KATRIN experiment (see Sec. 1.9).
3. The electronics shop and stock room is currently being reorganized and cleaned up.
4. We are acquiring training at the Washington Technology Center to learn the processes and the use of the tools needed for the construction of hybrid electronics on a fused silica based substrate.
5. A power supply controller module with TCP/IP based communication is under development.
6. A PSpice simulation model of capacitor dissipation noise was developed.

*Pacific Northwest National Laboratory, Richland, WA

8 Accelerator and ion sources

8.1 Van de Graaff accelerator and ion source operations and development

N. A. Boyd*, T. M. Cope, N. A. Gillgren†, G. C. Harper, A. W. Myers‡, D. A. Peterson, T. D. Van Wechel, and D. I. Will

The tandem was entered nine times this year. Gas bottles of either $^1H_2$ or $^2H_2$ were installed, swapped or refilled during three of the tank openings. The gradient was changed for single-ended running during two openings. Three openings were devoted to switching between tandem and single-ended operation. Repairs took place during four of the openings as follows. The low energy current monitor was repaired. One of the spinning brackets was replaced. The terminal ion source (TIS) steering wiring was replaced. A leak from the tank into the accelerator tube was repaired.

During the 12 months from 1 April, 2009 to 31 March, 2010 the tandem pellet chains operated 691 hours, the SpIS operated 1354 hours, and the DEIS operated 243 hours. Additional statistics of accelerator operations are given in Table 8.1-1.

ACTIVITY SCHEDULED	DAYS SCHEDULED	PERCENT of AVAILABLE TIME
Ion implantation, deck ion sources	74	20
Nuclear physics research, terminal ion source	113	31
Subtotal, ion implant or nuclear physics research	187	51
Machine development, maintenance, or crew training	80	22
Grand total	267	73

Table 8.1-1. Tandem Accelerator Operations April 1, 2009 to March 31, 2010

Development continued on the DEIS for the production of the positive ion beams of the noble gases. There is a push for higher currents of the rare isotopes, in particular ^{21}Ne which occurs with a natural abundance of about 2 parts per thousand. The aperture will be increased from 0.5 mm to 1.3 mm in diameter which will increase throughput but also increase emittance. Beam quality for implantation is unimportant so this is not a significant sacrifice.

*Left for grad school, Waterloo, ON, CA, August,2009
†Left CENPA September,2009
‡Pacific Northwest National Laboratory, Richland, WA

9 Other Research

9.1 Progress on a test of quantum nonlocal communication

J. G. Cramer

The question we have been investigating is whether the nonlocality of standard quantum mechanics is the private domain of Nature, as is generally assumed by the physics community, or whether in special circumstances the nonlocal connection between subsystems can be used to send signals from one observer to another. With the aid of generous private contributions and some use of CENPA resources, we have continued the work on this test of nonlocal quantum communication, which has been reported in the past three years[1,2,3]. The initial configuration of the experiment, as described in the first two references, employed a high power argon-ion laser operating at about 1 W in the ultraviolet at 351 nm that pumped nonlinear crystals (BBO or $LiIO_3$) to produce pairs of momentum-entangled 702 nm photons, on which measurements were subsequently performed. It was concluded that signal-to-noise limitations from fluoresence photons competing with the down-converted photons prevented the planned measurements using the initial configuration.

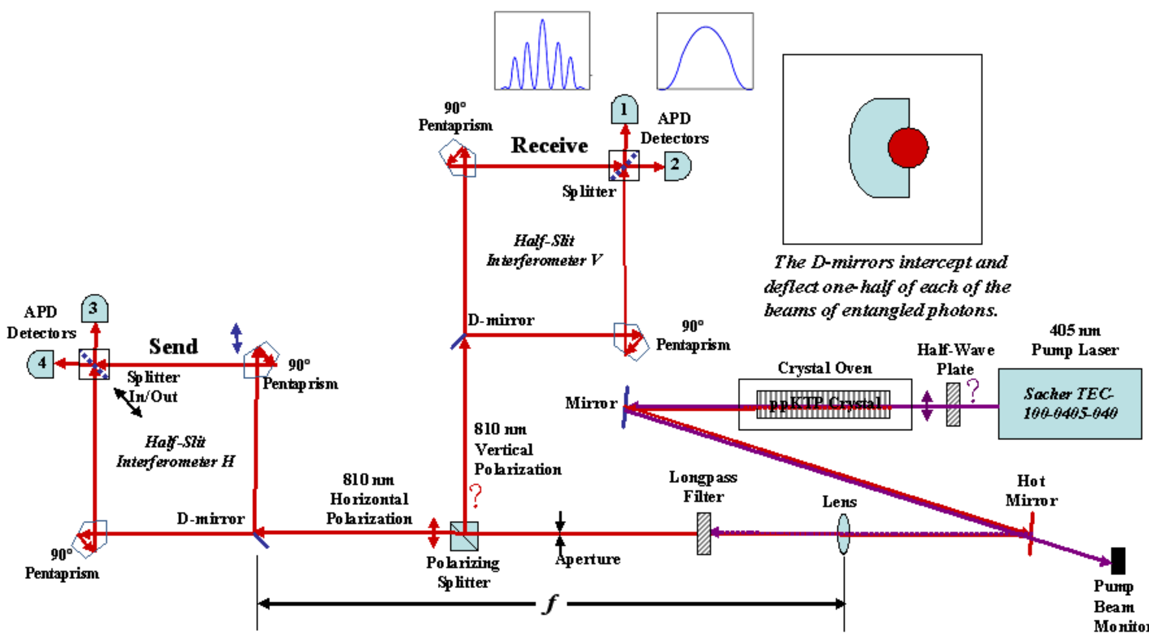

Figure 9.1-1. Schematic diagram of the Mark III quantum nonlocal communication test setup

In the past year the measurement has been moved to the Optics Laboratory on the 2nd floor of the Physics-Astronomy Building, where the experimental area can be darkened without interference with other experiments. We have purchased a 1 mm x 2 mm x 30 mm

[1]CENPA Annual Report, University of Washington (2007)pp. 52-54.
[2]CENPA Annual Report, University of Washington (2008), p. 42.
[3]CENPA Annual Report, University of Washington (2009), p. 41.

periodically-poled potassium titanyl phosphate (ppKTP) crystal from Raicol, Inc. with a 10 μm poling length that is maintained at 50° C in a crystal oven and is pumped with 405 nm horizontally polarized light to produce pairs of 810 nm momentum-entangled photons. The ppKTP crystal absorbs light at 351 nm, so a new pump laser was needed. A Littow-type grating-stabilized diode laser capable of delivering up to 100 mW at 405 nm was purchased from Sacher, Inc. to pump the ppKTP crystal, with the laser polarization rotated from vertical to horizontal with a half-wave plate.

To implement the interference measurements required by the experiment, we have replaced the two-slit interference setup with a "half-slit" momentum-sensitive version of the conventional Mach-Zehnder interferometer of our own design. This new type of interferometer is described in a separate article (see Sec. 9.2). This increases the sensitivity of the experiment, since a two-slit interferometer uses only 1-5% of the incident light while the half-slit interferometer uses essentially all of it. The new Mark III experimental configuration is shown in Fig. 9.1-1.

We moved the experiment in January-2010, and since then we have been aligning and testing the new Mark III configuration. Despite the large number of down-converted photons expected with the new crystal and laser (on the order of 10^5 pairs per second) we are still having trouble in detecting coincident photon pairs. We suspect that there are unanticipated inefficiencies in our avalanche photodiode (APD) detector system, and we are planning tests with alternative APDs.

9.2 A "half-slit" interferometer based on the Mach-Zehnder design

J. G. Cramer

The Mach-Zehnder interferometer[1,2] is a widely used optical instrument that separates a light beam into two paths and then recombines them into output beams corresponding to same-phase and reverse-phase mixtures of the path beams. Fig. 9.2-1 shows a classic Mach-Zehnder interferometer.

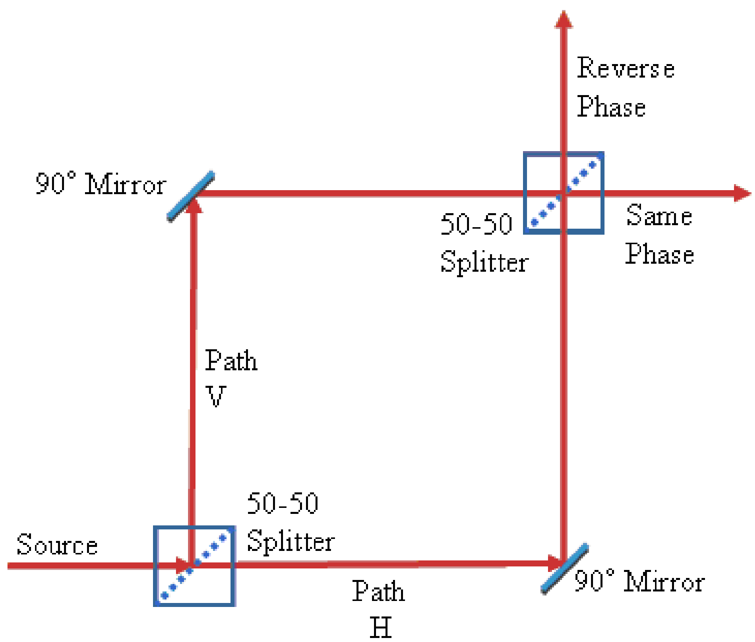

Figure 9.2-1. Schematic diagram of a classic Mach-Zehnder interferometer

The classic Mach-Zehnder interferometer is notoriously difficult to align, because each of its four reflecting elements (splitters and mirrors) must be located and rotated to wavelength-scale precision. Fortunately, Hariharan[3] has devised a modification in which 90° pentaprisms replace the two 90° mirrors, thereby guaranteeing two 90° deflections independent of slight misalignments and greatly simplifying the final adjustment of the interferometer. In the present work, we have adopted the Hariharan pentaprism scheme.

In the standard Mach-Zehnder interferometer, the choice of path through the interferometer taken by a hypothetical photon is randomly determined by the initial 50-50 beam-splitter. In particular, the choice of path is independent of the transverse momenta of incident photons. This makes the system unsuitable for investigations that involve interference effects that are related to momentum entanglement.

In two experiments demonstrating the operation of quantum nonlocality in systems of

[1] Ludwig Zehnder, Z. Instrumentenkunde 11, 275 (1891).
[2] Ludwig Mach, Z. Instrumentenkunde 12, 89 (1892).
[3] P. Hariharan, Applied Optics 8, 1925-1926 (1969).

momentum-entangled photons[4,5,6], Young-type two-slit systems were employed to demonstrate the presence or absence of interference depending on the absence or presence of "which-way" information provided by a momentum-entangled twin photon. The use of Young slits to demonstrate interference in such experiments leads to two undesirable features. First, each slit spreads the interference pattern over a single-slit diffraction envelope that can be very wide, complicating the detection of interference. Second, the large majority of the available entangled photons do not pass through either of the slits, but instead are absorbed at the barrier that the slits penetrate. It is therefore desirable to devise an alternative system that, like the Young two-slit system, produces momentum-dependent interference but that uses more of the available light. To accomplish this, we have designed a modified version of the Mach-Zehnder-Hariharan interferometer in which the path choice is momentum dependent. This device we will refer to as the "half-slit interferometer."

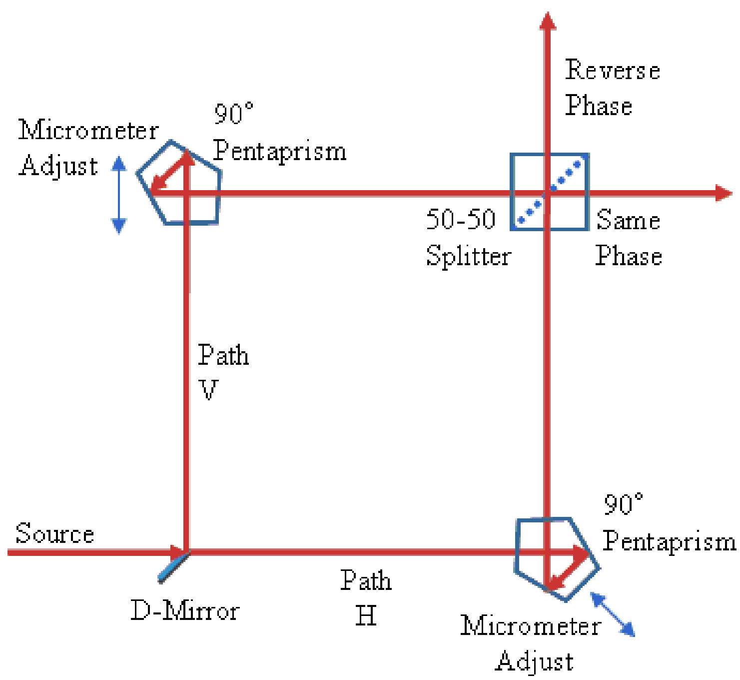

Figure 9.2-2. Schematic diagram of the Half-Slit Interferometer

Fig. 9.2-2 shows our design for the half-slit interferometer in which the path choice depends on the transverse momenta of incident photons. The initial 50-50 beam splitter has been replaced by a 45° D-shaped mirror that intercepts about half of the incident light beam. The intercepted part of the beam is deflected vertically on Path V in the diagram, while the non-intercepted part of the beam continues horizontally on Path H. If a given photon with momentum down the center line has a slight upward momentum component it will travel on Path H, while if it has a slight downward momentum component it will travel on Path V. As

[4]D. V. Strekalov, A. V. Sergienko, D. N. Klyshko, and Y. H. Shih, Phys. Rev. Letters 74, 3600-3603 (1995).
[5]Birgit Dopfer, PhD Thesis, University of Innsbruck (1998, unpublished).
[6]Anton Zeilinger, Rev. Mod. Physics 71, S288-S297 (1999).

in the classic Mach-Zehnder interferometer, the beams are re-combined at the upper splitter to produce same-phase and reverse-phase beam mixtures,

Fig. 9.2-2 indicates the directions of micrometer-driven adjustment motions used in the final alignment of the interferometer. The upper micrometer adjustment controls the location of the point at which the two beams intersect. This intersection point must lie on the reflection plane of the splitter. The lower micrometer adjustment, without changing the two beam directions, positions, or intersection point, controls the path length difference of the two beams. This should be adjusted (preferably using white light) to find the equal-path interference maximum at which the interferometer normally operates.

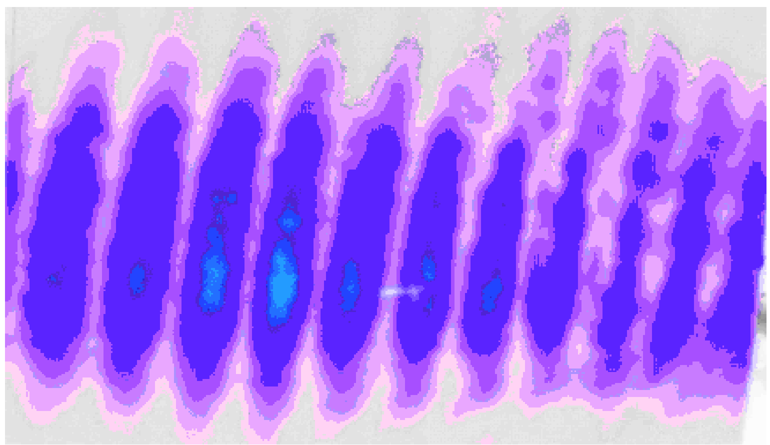

Figure 9.2-3. Interference fringes (405 nm) observed with the half-slit interferometer described here

Fig. 9.2-3 shows interference fringes observed with a preliminary version of the half-slit interferometer shown in Fig. 9.2-2. Here, a 405 nm violet diode laser was used as the light source. The light beams from the two paths each have edge-diffraction patterns at one edge that are not superimposed, but these are cut off by the apertures. Each beam has a non-Gaussian shape due to mirror truncation. Therefore, they have different non-circular outlines, and even with the best optimization of alignment they cannot have complete overlap. Nevertheless, it is estimated that 45% of the light entering the interferometer contributes to each of the interference patterns observed in the same-phase and opposite-phase outputs. This is a qualitative improvement in efficiency over observations of interference using a two-slit system.

Therefore, it appears that this half-slit interferometer satisfies the desired criteria of efficient production of momentum dependent interference patterns. We are using two of these devices in our onging tests with 810 nm momentum entangled photon pairs produced by down-conversion in a periodically poled KTP crystal described in a separate article (see Sec. 9.1).

9.3 Stochastics of dosimetry of C-ions

H. Bichsel and J.L. Schwartz* .

In a cancer treatment with $T = 3600$ MeV C-ions the energy spectrum of the ions at the Bragg peak is broad (see Fig. 9.3-1). For an irradiation the dose might be 4 Gy (Joule/kg), and the number of ions crossing a cell will be small. If we assume cells of $V_c = 10 \times 10 \times 10$ μm only about $N_D = 20$ ions *on the average* will traverse a cell. The actual number will be random, given by a Poisson distribution $P(n; N_D)$, and each ion will have a random energy selected from $f(T)$ in Fig. 9.3-1.

Monte Carlo calculations have been made to obtain the distribution $f(z)$ in cell dose z (actually "specific energy deposited" per cell) for 10,000 cells irradiated by an *average number* $N_D = 20$ per cell. The result is shown in Fig. 9.3-2. The doses z in the cells vary greatly, and we must expect a corresponding distribution $\phi(S_v)$ in *survival* S_v of the cells. The survival value S_v of *each cell* is calculated with the approximation

$$S_v = \sum_1^n \exp(-\alpha(T_n) \cdot nz(T_n))/n \qquad (1)$$

where n is chosen at random from $P(n; 20)$, and $\alpha(T_n)$ is determined in biological experiments with cells. The correlation between z and S_v is shown in Fig. 9.3-3.

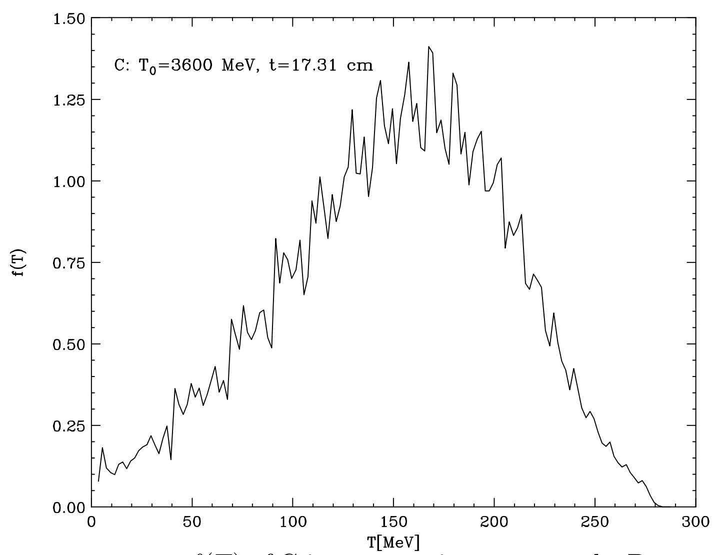

Figure 9.3-1. Energy spectrum $f(T)$ of C-ions traversing water at the Bragg peak, at depth $t = 17.31$ cm. The wiggles are an artifact of the convolution method used.

If in laboratory experiments irradiations of layers of cells with monoenergetic ions are made, the functions in Fig. 9.3-1, Fig. 9.3-2 are delta functions, and z as well as S_v are the same for each cell. The use of the results of laboratory experiments in deriving biological effects in tumor treatments thus appears to be a complex enterprise.

*UW Radiation Oncology.

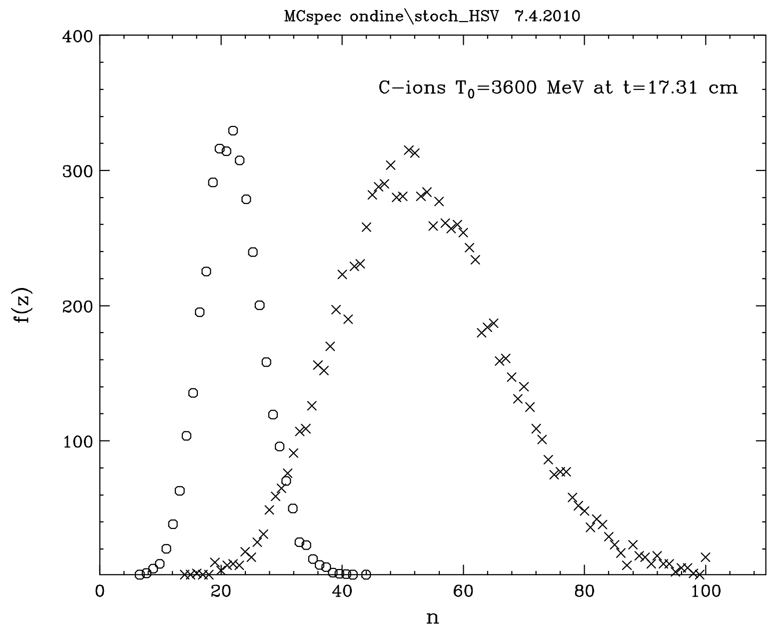

Figure 9.3-2. MC calculation of the spectrum of the number n of ions traversing cells is given by o. It is a Poisson distribution $P(n; N_D)$ with mean value $N_D = 20$. The spectrum of z ("specific energy") is given by $\times$, values are $z = n/10$ Gy.

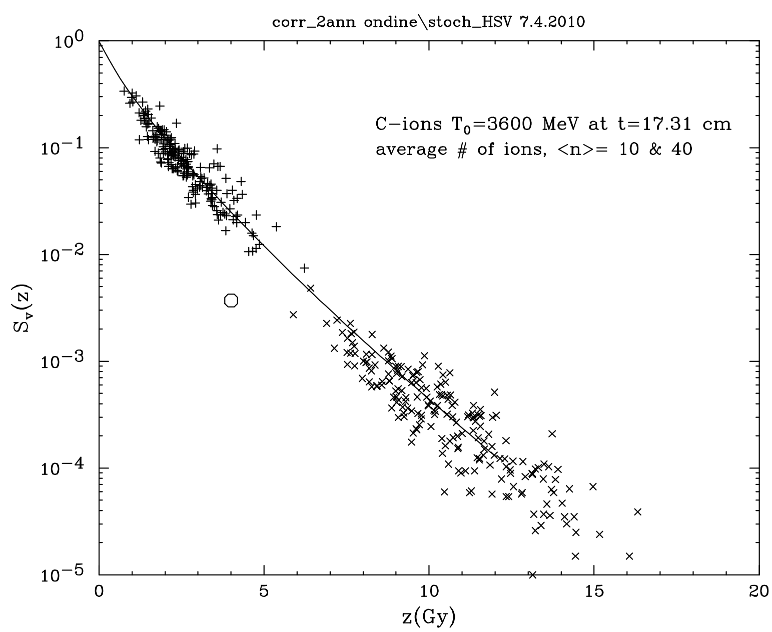

Figure 9.3-3. C-ion survival fractions for two experiments for 200 cells with irradiation dose of $< z >= 2.2$ Gy: $+$ and $< z >= 8.8$ Gy: $\times$. The function for $T = 140$ MeV and fixed $n = 20$ is given by $\bigcirc$. An "analytic" approximation to MC is given by the solid line.

10 CENPA Personnel

10.1 Faculty

Eric G. Adelberger[1]	Professor Emeritus
Massimo Bassan[1]	Visiting Professor[2]
Hans Bichsel[1]	Affiliate Professor
John G. Cramer	Professor Emeritus[3]
Peter J. Doe	Research Professor
Sanshiro Enomoto	Research Assistant Professor; CENPA Fellow
Alejandro García	Professor
Jens H. Gundlach[1]	Professor
Blayne R. Heckel[1]	Professor
Michael L. Miller	Research Assistant Professor; CENPA Fellow
R. G. Hamish Robertson	Professor; Director
Leslie J. Rosenberg[1]	Professor
Stephan Schlamminger[1]	Research Assistant Professor
Kurt A. Snover[1]	Research Professor Emeritus
Derek W. Storm[1]	Research Professor Emeritus
Nikolai R. Tolich	Assistant Professor
Thomas A. Trainor	Research Professor
Robert Vandenbosch[1]	Professor Emeritus
William G. Weitkamp[1]	Research Professor Emeritus
John F. Wilkerson[1,4]	Professor

10.2 CENPA External Advisory Committee

Baha Balantekin	University of Wisconsin
Stuart Freedman	UC Berkeley
William Zajc	Columbia University

[1]Not supported by DOE CENPA grant.
[2]On sabbatical from Università di Roma Tor Vergata, Rome, Italy, departed December 2009.
[3]With effect January, 2010.
[4]Affiliated faculty, University of North Carolina

10.3 Postdoctoral Research Associates

Frank Fleischer[1,2]	Seth Hoedl[1]
Jarek Kaspar	Andreas Knecht[3]
Gray Rybka[1]	Kazumi Tolich[4]
Brent VanDevender	Hok Wan Chan Tseung[1]
Chris Wrede	

10.4 Predoctoral Research Associates

Laura Bodine	Ted Cook[1]
Ian Derrington[1]	Jonathan Diaz Leon
Charles Hagedorn[1]	Michael Hotz[1]
Robert Johnson	David Kettler
Michelle Leber[5]	Michael Marino
Eric Martin	Jared Nance
Noah Oblath[6]	Anne Sallaska
Alexis Schubert	Daniel Scislowski
William Terrano[1]	Matthew Turner[1]
Todd Wagner[1]	Brandon Wall
Brett Wolfe	David Zumwalt

10.5 NSF Research Experience for Undergraduates participants

Dan Dandurand	Swarthmore College
Josh Eby	University of Indiana, South Bend
Jenna Walrath	Purdue University

[1]Not supported by DOE CENPA grant.
[2]Feodor Lynen Fellow
[3]Joined January, 2010
[4]Shoreline Community College, Seattle, WA
[5]Ph.D., March, 2010. Postdoctoral Fellow, U.C.S.B.
[6]Ph.D., August, 2009. Postdoctoral Fellow, M.I.T.

10.6 University of Washington undergraduates taking research credit

Jennie Chen	Blayne Heckel, Advisor
Brent Delbridge	Chris Wrede, Advisor
Blake Freeman	Chris Wrede, Advisor
Matthew Haefele	Ted Cook, Advisor
William Norton Haycox	Michael Miller, Advisor
Holly Hess	Eric Adelberger, Seth Hoedl, Advisors
Chantelle Jacques	Nikolai Tolich, Advisor
Eric Lee-Wong	Blayne Heckel, Advisor
John Mower	Nikolai Tolich, Advisor
Evan Nelson	Michael Miller, Brent VanDevender, Advisors
Andrew Palmer	A. García, Advisor
Natalie Ann Ramien	Nikolai Tolich, Advisor
Carin Schlimmer[1]	Stephan Schlamminger, Advisor
Devin Short	Chris Wrede, Advisor
Seth Tyson Coleman	Nikolai Tolich, Advisor
Rachel Vander Giessen	Chris Wrede, Advisor
Elizabeth Waldren	Nikolai Tolich, Advisor
David Williams	A. García, Advisor
Thomas Wolowiec	Leslie Rosenberg, Advisor

10.7 Professional staff

The professional staff are listed with a description of their recent major efforts.

John F. Amsbaugh	Research Engineer	KATRIN vacuum systems
Tom H. Burritt	Research Engineer	Design of KATRIN detector system
Gregory C. Harper	Associate Director	Electronic and mechanical design
Gary T. Holman	Computer Systems Manager	
Allan Myers[2]	Research Engineer	Electronic fabrication
Duncan J. Prindle, Ph.D.	Research Scientist	Heavy ion software
Richard J. Seymour[3]	Computer Systems Manager	
Hendrik Simons	Instrument Maker, Shop Supervisor	
H. Erik Swanson, Ph.D.	Research Physicist	Precision experimental equipment
Timothy D. Van Wechel	Electronics Engineer	Analog and digital electronics design
Douglas I. Will	Research Engineer	Cryogenics, ion sources

[1]Graduated and departed December 2009.
[2]Departed October 2009, P.N.N.L.
[3]Retired March 2010.

10.8 Technical staff

James Elms	Instrument Maker
David Hyde	Instrument Maker
David A. Peterson	Electronics Technician

10.9 Administrative staff

Victoria A. Clarkson	Administrator
Kate J. Higgins	Fiscal Specialist

10.10 Part time staff and student helpers

Nora Boyd[1]
Tyler Cope
Nathaniel Gillgren[2]
Jesse Heilman
Draza Miloshevich
Eugene Ngai[3]
Ahn Ngo[4]
Andrew Palmer
Jonathan Rollins
Carin Schlimmer[4,5]
Devin Short
Kevin Wald[6]
Kevin Wierman

[1]Departed August 2009, Graduate School, Waterloo, ON, CA.
[2]Departed September 2009
[3]Departed May 2009
[4]Departed December 2009
[5]Supported by NSF-Gravity funds
[6]Departed May 2010

11 Publications

Publications and presentations with a date of 2009 or 2010 are included below. Some entries from early 2009 may therefore also appear in the 2009 Annual Report.

11.1 Published papers

"Characterization of thin-foil ultracold neuron detectors," A. L. Sallaska, S. A. Hoedl, A. García, D. Melconian, A. R. Young, P. Geltenbort, S. K. L. Sjue, and A. T. Holley, Nucl. Instrum. Methods A **603**, 421 (2009).

"Study of astrophysically important resonant states in ^{30}S using the ^{32}S$(p,t)^{30}$S reaction," K. Setoodehnia, A. A. Chen, J. Chen, J. A. Clark, C.M. Deibel, D. Kahl, W. N. Lennard P. D. Parker, and C. Wrede, J. Phys.: Conf. Ser. **202**, 012042 (2010).

"Study of astrophysically important resonant states in ^{30}S using the ^{32}S$(p,t)^{30}$S reaction," K. Setoodehnia, A. A. Chen, J. Chen, J. A. Clark, C.M. Deibel, D. Kahl, W. N. Lennard, P. D. Parker, and C. Wrede, Nucl. Phys. **A834**, 205c (2010).

"Measurement of ^{23}Mg+p resonance energies," C. Wrede, D. W. Visser, J. A. Caggiano, J. A. Clark, C. Deibel, R. Lewis, A. Parikh, and P. D. Parker, Proceedings of Science (NIC X) **164**.

"First measurement of the ^{31}P(^{3}He,t)^{31}S reaction: a study of the thermonuclear ^{30}P$(p,\gamma)^{31}$S reaction rate," C. Wrede, J. A. Caggiano, J. A. Clark, C. Deibel, A. Parikh, and P. D. Parker, Proceedings of Science (NIC X) **062**.

"The ^{26m}Al$(p,\gamma)^{27}$Si reaction rate in ONe novae," C. M. Deibel, J. A. Clark, R. Lewis, A. Parikh, P. D. Parker, and C. Wrede, Proceedings of Science (NIC X) **053**.

"Study of astrophysically important resonant states in ^{30}S using the ^{32}S$(p,t)^{30}$S reaction," K. Setoodehnia, A. A. Chen, J. A. Clark, C. M. Deibel, D. Kahl, P. D. Parker, and C. Wrede, Proceedings of Science (NIC X) **161**.

"Towards an experimentally determined ^{26m}Al$(p,\gamma)^{27}$Si reaction rate in ONe novae," C. M. Deibel, J. A. Clark, R. Lewis, A. Parikh, P. D. Parker, and C. Wrede, Phys. Rev. C **80**, 035806 (2009).

"Properties of ^{23}Na implanted targets," T. A. D. Brown, K. Deryckx, A. García, A. L. Sallaska, K. A. Snover, D. W. Storm, and C. Wrede, Nucl. Instrum. Methods B **267**, 3302 (2009).

"Thermonuclear ^{30}S$(p,\gamma)^{31}$Cl reaction in type I x-ray bursts," C. Wrede, J. A. Caggiano, J. A. Clark, C. M. Deibel, A. Parikh, and P. D. Parker, Phys. Rev. C **79**, 045808 (2009); Phys. Rev. C **80**, 019904(E) (2009).

"Measurements of ^{31}S energy levels and reevaluation of the thermonuclear resonant ^{30}P$(p,\gamma)^{31}$S reaction rate," C. Wrede, J. A. Caggiano, J. A. Clark, C. M. Deibel, A. Parikh, and P. D. Parker, Phys. Rev. C **79**, 045803 (2009).

"Thermonuclear ^{25}Al$(p,\gamma)^{26}$Si reaction rate in classical novae and Galactic ^{26}Al," C. Wrede, Phys. Rev. C **79**, 035803 (2009).

"Nuclear structure relevant to neutrinoless double β decay: the valence protons in ^{76}Ge and ^{76}Se," B. P. Kay, J. P. Schiffer, S. J. Freeman, T. Adachi, J. A. Clark, C. M. Deibel, H. Fujita, P. Grabmayr, H. Hatanaka, D. Ishikawa, H. Matsubara, Y. Meada, H. Okamura, K. E. Rehm, Y. Sakemi, Y. Shimizu, H. Shimoda, K. Suda, Y. Tameshige, A. Tamii, and C. Wrede, Phys. Rev. C **79**, 021301(R) (2009).

"A SQUID-based microwave cavity search for dark-matter axions," S. J. Asztalos, G. Carosi, C. Hagmann, D. Kinion, K. van Bibber, M. Hotz, L. Rosenberg, G. Rybka, J. Hoskins, J. Hwang, P. Sikivie, D. B. Tanner, R. Bradley, and J. Clarke, Phys. Rev. Lett. **104**, 041301 (2010).

"Identified particle production, azimuthal anisotropy, and interferometry measurements in Au+Au collisions at $\sqrt{s_{NN}} = 9.2$ GeV," B. I. Abelev and the STAR Collaborators,* Phys. Rev. C **81**, 24911 (2010), arXiv:0909.4131 [nucl-ex].

"System size dependence of associated yields in hadron-triggered jets," B. I. Abelev and the STAR Collaborators,* *et al*, Phys. Lett. B **683**, 123 (2010), arXiv:0904.1722 [nucl-ex].

"Longitudinal double-spin asymmetry and cross section for inclusive neutral pion production at midrapidity in polarized proton collisions at $\sqrt{s_{NN}} = 200$ GeV," B. I. Abelev and the STAR Collaborators,* *et al*, Phys. Rev. D **80**, 111108 (2009), arXiv:0911.2773 [nucl-ex].

"Longitudinal spin transfer to Λ and $\bar{\Lambda}$ hyperons in polarized proton-proton collisions at $\sqrt{s} = 200GeV$," B. I. Abelev and the STAR Collaborators,* Phys. Rev. D **80**, 111102 (2009).

"Azimuthal charged-particle correlations and possible local strong parity violation," B. I. Abelev and the STAR Collaborators,* Phys. Rev. Lett. **103**, 251601 (2009), arXiv:0909.1739 [nucl-ex].

"Long range rapidity correlations and jet production in high energy nuclear collisions," B. I. Abelev and the STAR Collaborators,* Phys. Rev. C **80**, 64192 (2009), arXiv:0909.0191 [nucl-ex].

"Neutral pion production in Au+Au collisions at $\sqrt{s_{NN}} = 200$ GeV," B. I. Abelev and the STAR Collaborators,* Phys. Rev. C **80**, 44905 (2009), arXiv:0907.2721 [nucl-ex].

"Center of mass energy and system-size dependence of photon production at forward rapidity at RHIC," B. I. Abelev and the STAR Collaborators,* Nucl. Phys. **A832**, 134 (2009), arXiv:0906.2260v1 [nucl-ex].

"Growth of long range forward-backward multiplicity correlations with centrality in Au+Au collisions at $\sqrt{s_{NN}} = 200$ GeV," B. I. Abelev and the STAR Collaborators,* Phys. Rev. Lett. **103**, 172301 (2009), arXiv:0905.0237 [nucl-ex].

"J/psi production at high transverse momentum in p+p and Cu+Cu collisions at $\sqrt{s_{NN}} =$ 200 GeV," B. I. Abelev and the STAR Collaborators,* Phys. Rev. C **80**, 41902 (2009), arXiv:0904.0439 [nucl-ex].

"Pion iterferometry in Au+Au and Cu+Cu collisions at RHIC," B. I. Abelev and the STAR Collaborators,* Phys. Rev. C **80**, 24905 (2009), arXiv:0903.1296 [nucl-ex].

"K/pi fluctuations at relativistic energies," B. I. Abelev and the STAR Collaborators,* Phys. Rev. Lett. **103**, 92301 (2009), arXiv:0901.1795v1 [nucl-ex].

"Measurement of D* mesons in jets from p+p collisions at $\sqrt{s_{NN}} = 200$ GeV," B. I. Abelev and the STAR Collaborators,* Phys. Rev. D **79**, 112006 (2009), arXiv:0901.0740 [nucl-ex].

"Observation of two-source interference in the photoproduction reaction $AuAu \to AuAu\rho^0$," B. I. Abelev and the STAR Collaborators,* Phys. Rev. Lett. **102**, 112301 (2009), arXiv:0812.1063 [nucl-ex].

"Energy and system size dependence of ϕ meson production in Cu+Cu and Au+Au collisions," B. I. Abelev and the STAR Collaborators,* Phys. Lett. B **673**, 183 (2009), arXiv:0810.4979 [nucl-ex].

"Measurements of ϕ meson production in relativistic heavy-ion collisions at RHIC," B. I. Abelev and the STAR Collaborators,* Phys. Rev. C **79**, 64903 (2009), arXiv:0809.4737 [nucl-ex].

"Systematic measurements of identified particle spectra in *pp*, d+Au and Au+Au collisions from STAR," B. I. Abelev and the STAR Collaborators,* Phys. Rev. C **79**, 34909 (2009), arXiv:0808.2041 [nucl-ex].

"Beam-energy and system-size dependence of dynamical net charge," B. I. Abelev and the STAR Collaborators,* Phys. Rev. C **79**, 24906 (2009), arXiv:0807.3269 [nucl-ex].

"System-size dependence of Λ and Ξ production in nucleus–nucleus collisions at 40A and 158A GeV measured at the CERN Super Proton Synchrotron," C. Alt and the NA49 Collaborators,* Phys. Rev. C **80**, 034906 (2009), arXiv:0906.0469 [nucl-ex].

"Energy dependence of transverse momentum fluctuations in Pb+Pb collisions at the CERN Super Proton Synchrotron (SPS) at 20A to 158A GeV," C. Alt and the NA49 Collaborators,* Phys. Rev. C **79**, 044904 (2009), arXiv:0810.5580 [nucl-ex].

"Energy dependence of particle ratio fluctuations in central Pb+Pb collisions from $\sqrt{s_{NN}} =$ 6.3 to 17.3 GeV," C. Alt and the NA49 Collaborators,* Phys. Rev. C **79**, 044910 (2009).

"A liquid helium target system for a measurement of parity violation in neutron spin rotation," C. D. Bass, T. D. Bass, B. R. Heckel, C. R. Huffer, D. Luo, D. M. Markoff, A. M. Micherdzinska, W. M. Snow, H. E. Swanson, S. C. Walbridge, Nucl. Instrum. Methods A **612**, 69 (2009).

"Laboratory tests of the equivalence principle at the University of Washington," J. H. Gundlach, S. Schlamminger, T. A. Wagner, Space Science Review **148**, 201 (2009).

"Charge management for gravitational-wave observatories using UV LEDs," S. E. Pollack, M.D. Turner, S. Schlamminger, C. A. Hagedorn and J. H. Gundlach, Phys. Rev. D **81**, 021101(R) (2010).

"Measurement of the cosmic ray and neutrino-induced muon flux at the Sudbury Neutrino Observatory," B. Aharmim and the SNO Collaborators,* Phys. Rev. D **80**, 012001, (2009), arXiv:0902.2776.

"The Sudbury Neutrino Observatory," N. Jelley, A. B. McDonald, and R. G. H. Robertson, Ann. Rev. Nucl. Part. Sci. **59**, 431 (2009).

"Explain it in 60 seconds: Shielding," R. G. H. Robertson, symmetry 07, vol. 01 (2010).

"Searches for High Frequency Variations in the ^{8}B Neutrino Flux at the Sudbury Neutrino Observatory," B. Aharmim and the SNO Collaborators,* Astrophys. J. **710**, 540 (2010).

"Weak-interaction strength from charge-exchange reactions versus β-decay in the A = 40 isoquintet," M. Bhattacharya, C. D. Goodman and A. García, Phys. Rev. C **80**, 055501 (2009).

"Improved limit on the permanent electric dipole moment of ^{199}Hg," W. C. Griffiths, M. D. Swallows, T. H. Loftus, M. V. Romalis, B. R. Heckel, and E. N. Fortson, Phys. Rev. Lett. **102**, 101601 (2009).

"Evolution of minimum-bias parton fragmentation in nuclear collisions," T. A. Trainor, Phys. Rev. C **80**, 044901 (2009).

"ZYAM and $\mathbf{v_2}$: Underestimating jet yields from dihadron azimuth correlations," T. A. Trainor, Phys. Rev. C **81**, 014905 (2010).

"Low energy threshold analysis of the Phase I and Phase II data sets of the Sudbury Neutrino Observatory," B. Aharmim and the SNO Collaborators,* SNO LA-UR-09-06694, (2009) arXiv:0910.2984 [nucl-ex].

"Updated S factors for the $^{7}\mathrm{Be}(p,\gamma)^{8}\mathrm{B}$ reaction," A. R. Junghans, K. A. Snover, E. C. Mohrmann, E. G. Adelberger and L. Buchmann, Phys. Rev. C **81**, 012801(R) (2010).

11.2 Papers submitted or to be published 2010

“Results from a search for light-mass dark matter with a P-type point contact germanium detector, C. E. Aalseth and the CoGeNT Collaborators,* (2010) arXiv:1002.4703 [astro-ph.CO].

“First direct measurement of the ^{23}Mg$(p,\gamma)^{24}$Al reaction,” L Erikson, C. Ruiz, F. Ames, P. Bricault, L. Buchmann, A. A. Chen, J. Chen, H. Dare, B. Davids, C. Davis, C. Deibel, M. Dombsky, S. Foubister, N. Galinski, U. Greife, U. Hager, A. Hussein, D. A. Hutcheon, J. Lassen, L. Martin, D. F. Ottewell, C. V. Ouellet, G. Ruprecht, K. Setoodehnia, A. C. Shotter, A. Teigelhöfer, C. Vockenhuber, C. Wrede, and A. Wallner, accepted for publication in Phys. Rev. C.

“Towards precise Q_{EC} values for the superallowed $0^+ \to 0^+$ β decays of $T = 2$ nuclides: The masses of ^{20}Na, ^{24}Al, ^{28}P, and ^{32}Cl,” C. Wrede, J. A. Clark, C. M. Deibel, T. Faestermann, R. Hertenberger, A. Parikh, H.-F. Wirth, S. Bishop, A. A. Chen, K. Eppinger, A. García, R. Krücken, O. Lepyoshkina, G. Rugel, and K. Setoodehnia, accepted for publication in Phys. Rev. C.

“Positive ion beams of the noble gases for implantation from a direct extraction duoplasmatron ion source,” G. C. Harper, October, 2009, SNEAP 2009, University of Arizona, Tuscon, AZ.

“University of Washington Lab Report to SNEAP 2009,” J. F. Amsbaugh, N. M. Boyd, N. A. Gilgren, G. C. Harper, A. W. Myers, D. A. Short, T. D. VanWechel, and D. I. Will, October, 2009, SNEAP 2009, University of Arizona, Tuscon, AZ.

“Why Everettians should appreciate the transactional interpretation,” R. E. Kastner and J. G. Cramer, March, 2010, submitted for publication to Foundations of Physics, arXiv:1001.2867 [quant-ph].

“Longitudinal scaling property of the charge balance function in Au + Au collisions at 200 GeV,” B. I. Abelev and the STAR Collaborators,* February, 2010, submitted for publication to Phys. Rev. Lett., arXiv:1002:1641 [nucl-ex].

“Charged and strange hadron elliptic flow in Cu+Cu collisions at $\sqrt{s_{NN}} = 62.4$ and 200 GeV,” B. I. Abelev and the STAR Collaborators,* January, 2010, submitted for publication to Phys. Rev. C, arXiv:1001.5052 [nucl-ex].

“Upsilon cross section in p+p collisions at sqrt(s) = 200 GeV,” B. I. Abelev and the STAR Collaborators,* January, 2010, submitted for publication to Phys. Rev. D, arXiv:1001.2745 [nucl-ex].

“Three-particle coincidence of the long range pseudorapidity correlation in high energy nucleus-nucleus collisions,” B. I. Abelev and the STAR Collaborators,* January, 2010, submitted for publication to Phys. Rev. Lett., arXiv:0912.3977 [nucl-ex].

"Inclusive π^0, η, and direct photon production in p+p and d+Au collisions at $\sqrt{s_{NN}} = 200$ GeV," B. I. Abelev and the STAR Collaborators,* December, 2009, submitted for publication to Phys. Rev. D, arXiv:0912.3838 [nucl-ex].

"Studying parton energy loss in heavy-ion collisions via direct-photon and charged-particle azimuthal correlations," B. I. Abelev and the STAR Collaborators,* December, 2009, submitted for publication to Phys. Rev. Lett., arXiv:0912.1871 [nucl-ex].

"Observation of $\pi^+\pi^-\pi^+\pi^-$ photoproduction in ultra-peripheral heavy ion collisions at STAR," B. I. Abelev and the STAR Collaborators,* December, 2009, submitted for publication to Phys. Rev. Lett., arXiv:0912.0604 [nucl-ex].

"Identified high-p_T spectra in Cu+Cu collisions at $\sqrt{s_{NN}}$=200 GeV," B. I. Abelev and the STAR Collaborators,* November, 2009, submitted for publication to Phys. Rev. Lett., arXiv:0911.3130 [nucl-ex].

"Observation of an antimatter hypernucleus," B. I. Abelev and the STAR Collaborators,* October, 2009, submitted for publication to Phys. Rev. D, arXiv:1003.2030 [nucl-ex].

"Observation of charge-dependent azimuthal correlations and possible local strong parity violation in heavy ion collisions," B. I. Abelev and the STAR Collaborators,* September, 2009, submitted for publication to Phys. Rev. D, arXiv:0909.1717 [nucl-ex].

"Yields and elliptic flow of $d(\overline{d})$ and $^3He(\overline{^3He})$ in Au+Au collisions at $\sqrt{s_{_{NN}}} = 200$ GeV," B. I. Abelev and the STAR Collaborators,* September, 2009, submitted for publication to Phys. Rev. D, arXiv:0909.0566 [nucl-ex].

"The interaction of radiation with matter," H. Bichsel, 2010, submitted for publication to Handbook of Particle Physics, Springer Verlag (Landoldt-Boernstein).

"Solubility, light output and energy resolution studies of molybdenum-loaded liquid scintillators," V. M. Gehman, P. J. Doe, R. G. H. Robertson, D. I. Will, H. Ejiri, and R. Hazama, 2010, submitted for publication to Nucl. Instrum. Methods A.

"Improved limit on the permanent electric dipole moment of ^{199}Hg," W. C. Griffiths, M. D. Swallows, T. H. Loftus, M. V. Romalis, B. R. Heckel, and E. N. Fortson, to be submitted to Phys. Rev. A.

"Measurement of the stark-induced interference in ^{199}Hg," T. H. Loftus, B. R. Heckel, and E. N. Fortson, to be submitted to Phys. Rev. Lett.

"Is hydrodynamics relevant to RHIC collisions?," T. A. Trainor, accepted for publication in J. Phys. G, arXiv:0906.1229 [hep-ph].

“The calibration of the Sudbury Neutrino Observatory using uniformly distributed radioactive sources,” K. Boudjemline, B. Cai, B. T. Cleveland, H. C. Evans, J. Farine, R. J. Ford, E. Guillian, A. L. Hallin, E D. Hallman, C. Howard, P. Jagam, N. A. Jelley, K. J. Keeter, J. R. Klein, C. Kraus, C. B. Krauss, R. Lange, I. T. Lawson, J. V. L. Rusu, S R. Seibert, P. Skensved, and M. J. Thomson; Nucl. Instrum. Methods A51444 (in press).

11.3 Invited talks, abstracts and other conference presentations

“Probing nucleosynthesis in novae: ^{22}Na$(p,\gamma)^{23}$Mg,” A. L. Sallaska, 3rd Joint Meeting of the APS Division of Nuclear Physics and the Physical Society of Japan, October, 2009.

“Precise nuclear masses via magnetic spectroscopy,” C. Wrede, Technische Universität München, seminar, Garching, Germany, November, 2009.

“Mass of the lowest $T = 2$ level in ^{32}Cl,” C. Wrede for the CPT collaboration, 3rd Joint Meeting of the APS Division of Nuclear Physics and the Physical Society of Japan, October, 2009.

“Status of the ultra cold neutron beta asymmetry (UCNA) experiment,” C. Wrede for the UCNA Collaboration, Los Alamos Neutron Science Center (LANSCE) users group meeting, invited presentation, Santa Fe, NM, USA, September, 2009.

“Beta decay of ^{32}Ar for fundamental tests,” C. Wrede, Argonne-ATLAS users meeting, presentation, Argonne, IL, USA, August, 2009.

“Rotating torsion balance tests of the equivalence principle,”, T. Wagner, Session S10.003 APS, April, 2010.

“Exotic physics with ADMX,” G. Rybka, Axions 2010, University of Florida, Gainesville, FL, January, 2010.

“ADMX: searching for axions and other light hidden particles,” G. Rybka, SLAC Dark Forces Workshop, Menlo Park, CA, September, 2009.

“ADMX: continuing search for dark matter axions,” G. Rybka, 5th Patras Workshop on Axions, WIMPs and WISPS, Durham, UK 13 July, 2009.

“Direct neutrino mass measurements,” B. A. VanDevender, Conference on the Intersections of Particle and Nuclear Physics, (CIPANP), May, 2009.

“Weighing the Neutrino,” B. A. VanDevender, James Madison University Physics and Astronomy Department Colloquium, January, 2010.

“Direct neutrino mass measurements: past, present and future,” B. A. VanDevender, Technical Seminar at Los Alamos National Lab, February, 2010.

"Positive ion beams of the noble gases for implantation from a direct extraction duoplasmatron ion source," G. C. Harper, SNEAP 2009, University of Arizona, Tuscon, AZ, October, 2009.

"Gravity scale particle physics with torsion pendulums: a new axion search," S. A. Hoedl, Duke University Colloquium, Durham, NC, April, 2010.

"A torsion pendulum based axion search," S. A. Hoedl, Texas A&M Seminar, College Station, TX, April, 2010.

"Gravity scale particle physics with torsion pendulums: a new axion search," S. A. Hoedl, North Carolina State University Colloquium, Raleigh, NC, March, 2010.

"Torsion pendulum based searches for axions and other exotic forces," S. A. Hoedl, GRANIT Workshop, Les Ecoles de Physique, Les Houches, France, February, 2010.

"Torsion pendulum based axion search," S. A. Hoedl, Indiana University Seminar, Bloomington, Indiana, January, 2010.

"Torsion pendulum based axion search," S. A. Hoedl, Triangle University Nuclear Laboratory Seminar, Durham, NC, September, 2009.

"Gravity scale particle physics with torsion pendulums," S. A. Hoedl, Leptons/Photons 2009, Hamburg, Germany, February, 2010.

"Measurement of the parity-odd neutron spin rotation in liquid helium," H. E. Swanson on behalf of the Neutron Spin Rotation Collaboration, APS April Meeting, Washington D.C., February, 2010.

"Precise mechanical experiments for metrology and fundamental physics," S. Schlamminger, NIST Seminar, Gaithersburg, MD, January, 2010.

"Laboratory tests of the inverse square law of gravity," S. Schlamminger, April Meeting of the APS, Washington, DC, February, 2010.

"Study of SNO+ liquid scintillator energy response," H. S. Wan Chan Tseung, APS April Meeting, Washington, D.C., February, 2010.

"Neutrino physics for the masses," R. G. H. Robertson, Colloquium, Michigan State University February, 2009.

"Neutrino physics for the masses," R. G. H. Robertson, Colloquium, University of Chicago, February, 2009.

"Neutrino physics for the masses," R. G. H. Robertson, Colloquium, University of Victoria, April, 2009.

"Neutrino physics for the masses," R. G. H. Robertson, Argonne National Laboratory, February, 2010.

“Detecting neutrinos,” R. G. H. Robertson, INT Summer School, Seattle, WA, July, 2009.

“Kinematic measurements,” R. G. H. Robertson, INT Workshop: The Future of Neutrino Mass Measurements, Seattle, WA, February, 2010.

“Searches for new physics using the neutron,” A. García, Plenary talk at the Meeting of the NW-section of the APS at Vancouver, BC, May, 2009.

“Searches for new physics using the neutron,” A. García, Physics Colloquium, Texas A&M, September, 2009.

“Results from the UCNA collaboration,” A. García, Workshop: *Research Opportunities with Ultracold Neutrons in the US*, Santa Fe, NM, November, 2009.

“New results on the electric dipole moment of ^{199}Hg,” B. R. Heckel, April Meeting of the APS, Washington D.C., February, 2010.

“Systematics of parton fragmentation in e^+-e^- and nuclear collisions,” T. A. Trainor, 39th International Symposium on Multiparticle Dynamics: ISMD 2009, Gomel, Belarus, September, 2009.

“v2(pt) From 2D Angular Correlations and Centrality Evolution of the Azimuth Quadrupole pt Spectrum,” T. A. Trainor and David Kettler, 39th International Symposium on Multiparticle Dynamics: ISMD 2009, Gomel, Belarus, September, 2009.

“Data management with CouchDB,” M. L. Miller, no::sql(east) Conference, Atlanta, GA, October, 2009.

“Scientific data management with CouchDB,” M. L. Miller, OpenSQL Conference, Portland, OR, November, 2009.

“Probing low-mass dark matter with the Majorana Demonstrator,” M. L. Miller, APS Spring Meeting, Washington, D.C., February, 2010.

“Probing the Neutrino Mass Hierarchy,” L. I. Bodine, Meeting of the NW-section of the APS at Vancouver, BC, May, 2009

“Simulating 1GeV Electrons and Muons in a Very Large Liquid Scintillator Detector,” N.R. Tolich, Advances in Neutrino Technology, Manoa, HI, August, 2009.

“Status of the SNO+ Experiment,” N.R. Tolich, Workshop on Next Generation Nucleon Decay and Neutrino Detectors, Estes Park, Co, October, 2009.

“Probing Nucleosynthesis in Novae: ^{22}Na$(p, \gamma)^{23}$Mg,” A. L. Sallaska, Meeting of the NW-section of the APS at Vancouver, BC, May, 2009 (poster).

*UW collaborators for the various CENPA research groups are listed below (April 1, 2009 - March 31, 2010):

CoGeNT Collaborators: M. G. Marino, M. L. Miller, R. G. H. Robertson, T. D. Van Wechel

NA49 Collaborators: J. G. Cramer

SNO Collaborators: P. J. Doe, N. S. Oblath, R. G. H. Robertson, N. Tolich, B. L. Wall, H. S. Wan Chan Tseung, J. F. Wilkerson

STAR Collaborators: H. Bichsel, J. G. Cramer, D. T. Kettler, D. J. Prindle and T. A. Trainor. In cases where some CENPA personnel played a major role in a STAR publication, their names are listed explicitly.

11.4 Ph.D. degrees granted

A Measurement of Neutral-Current Neutrino Interactions at the Sudbury Neutrino Observatory with an Array of ^{3}He *Proportional Counters*, Noah Oblath (August, 2009).

Monte Carlo Calculations of the Intrinsic Detector Backgrounds for the Karlsruhe Tritium Neutrino Experiment, Michelle Leber (March, 2010).